

First Principles Design and Investigation of Lithium-Ion Battery Cathodes and Electrolytes

by

Shyue Ping Ong

Submitted to the Department of Materials Science and Engineering
in partial fulfillment of the requirements for the degree of

Doctor of Philosophy

at the

MASSACHUSETTS INSTITUTE OF TECHNOLOGY

February 2011

© Massachusetts Institute of Technology 2011. All rights reserved.

Author
Department of Materials Science and Engineering
Jan 4, 2011

Certified by
Gerbrand Ceder
R.P. Simmons Professor of Materials Science and Engineering
Thesis Supervisor

Accepted by
Christopher Schuh
Chairman, Departmental Committee on Graduate Students

First Principles Design and Investigation of Lithium-Ion Battery Cathodes and Electrolytes

by

Shyue Ping Ong

Submitted to the Department of Materials Science and Engineering
on Jan 4, 2011, in partial fulfillment of the
requirements for the degree of
Doctor of Philosophy

Abstract

In this thesis, we leveraged on first principles techniques to advance our understanding of Li-ion battery technology. Two major components in a Li-ion battery were studied, namely the cathode and the electrolyte. Simultaneous materials advances in these areas are needed to increase the energy density and improve the safety of Li-ion batteries.

On the cathode front, we have advanced the understanding of phase equilibria in the technologically important Li-Fe-P-O system by constructing the phase diagram as a function of oxidation conditions.[1] The predictions of the calculated diagram agree well with previous experimental findings. The combined application of the phase diagrams and an Ellingham diagram provides a means to more efficiently focus experimental efforts to optimize synthesis approaches for LiFePO_4 .

We then developed a means to predict the thermal stability of a material by determining the oxygen evolution as a function of oxygen chemical potential / temperature.[2] In agreement with previous experimental findings, we predicted delithiated FePO_4 to be the most thermally stable, and delithiated MnPO_4 to be less stable. The delithiated high-voltage NiPO_4 and CoPO_4 olivines were found to be the least stable, suggesting a correlation between voltage and thermal stability.

We revisited the calculation of lithium intercalation potentials and oxide redox energies in the context of the Heyd-Scuseria-Ernzerhof (HSE06)[3, 4] hybrid functional.[5] We found the HSE06 functional to perform similarly to DFT+ U in the prediction of lithium intercalation potentials and oxide redox energies, albeit at a significantly higher computational cost.

Using HSE06, we investigated the polaron migration barriers and phase separation energies of LiMnPO_4 and LiFePO_4 . The polaron migration barriers were found to be significantly higher in the Mn olivine as compared to the Fe olivine, and indicates approximately two orders of magnitude difference in conductivity between the two materials, in agreement with previous experimental findings. However, HSE06 predicts qualitatively incorrect phase separation energies in LiFePO_4 , suggesting that its treatment of electron correlation in more strongly localized transition metal states

is still deficient.

On the electrolyte front, we investigated the trends in the gas-phase electron affinities (EAs) of room-temperature ionic liquid (IL) cations and ionization energies (IEs) of IL anions by systematically transversing the IL ion chemical space using computational chemistry methods.[6] Our results show that trends in the calculated vertical EAs and IEs are in qualitative agreement with the relative experimental redox stabilities of ILs formed from various cations and anions. A monotonic decreasing trend of cation EA with increasing alkylation is observed, while no apparent trend is observed for anions. We found that electron-donating (ED) functional groups decreases the EA of the cation and IE of the anion, and hence, increases the stability of the cation against reduction but decreases the stability of the anion against oxidation. The reverse is true for electron-withdrawing (EW) functional groups. We also demonstrated that the position of substitution is important in determining the strength of the ED or EW effects. These qualitative trends agree well with previous experimental and theoretical results.

Thesis Supervisor: Gerbrand Ceder

Title: R.P. Simmons Professor of Materials Science and Engineering

Acknowledgments

First and foremost, I would like to thank my thesis advisor, Professor Gerbrand Ceder, for his guidance throughout my graduate studies. Beyond your always illuminating insights, I have been inspired by your vision and commitment to the scientific pursuit.

I am grateful to the current and previous members of my thesis committee, Professors Nicola Marzari, Troy Van Voorhis and Jeffrey Grossman, for their ideas and advice at critical stages of my research.

I thank my collaborators, Lei Wang, Vincent Chevrier, Oliviero Andreussi, Anubhav Jain, Geoffroy Hautier, Byoungwoo Kang and Rickard Armiento. Much of the work in this thesis would not have been possible without your contributions. I hope this thesis is the start of many fruitful collaborations to come. I also thank you and the current members and alumni of the Ceder research group for making graduate life stimulating, fun and interesting.

I thank my father for challenging me to reach greater heights, my mum for always quietly standing by me, and my brother for his support.

To Seow Hong Ong and Eleanor Tan, thank you for being there to share with me my brightest days and carry me through my darkest hours.

To my ex-wife, Jynn Goh, I thank you for starting this journey with me, even if you did not have the faith to finish it.

I also would like to thank the Public Service Division of Singapore for their understanding all these years.

Finally, to my girlfriend, Denise Ang, I could not have completed this journey without your constant support and encouragement. Your love gives me the courage to continue to pursue my dreams.

Contents

1	Introduction	17
1.1	Anatomy of a lithium-ion battery	18
1.1.1	Intercalation cathodes	18
1.1.2	Electrolytes	20
1.2	Motivation and overview	22
2	Phase diagrams from first principles	27
2.1	Compositional phase diagrams	28
2.2	Oxygen grand potential phase diagrams	29
2.3	First principles energies from density functional theory	31
2.4	Limitations	33
3	The Li-Fe-P-O oxygen grand potential phase diagram	35
3.1	The LiFePO ₄ cathode material	35
3.2	Calculated energies of Li-Fe-P-O phases	37
3.3	Verification of calculated ternary sub-system phase diagrams	37
3.4	Constant μ_{O_2} phase diagrams	41
3.5	Modified Ellingham diagram	46
3.6	Phase equilibria pertinent to LiFePO ₄ synthesis	48
3.7	Applications	54
3.8	Conclusion	55
4	Estimating the thermal stability of intercalation electrodes	57

4.1	Thermal stability in olivine cathodes	57
4.2	Computational details	58
4.3	Phase diagrams at critical μ_{O_2} for reduction	59
4.4	O_2 evolved versus temperature	62
4.5	Implications for cathode design	63
4.6	Thermal stability as a design criteria in a high-throughput materials search	65
4.7	Conclusion	65
5	Beyond DFT: Hybrid functional calculations of redox energies	67
5.1	Redox energies in DFT	67
5.2	Hybrid functionals	68
5.3	Methods	69
5.3.1	Intercalation potentials of electrode materials	69
5.3.2	Oxide Formation Energies	71
5.3.3	Computational Methods	72
5.4	Comparison of calculated intercalation potentials	73
5.5	Comparison of oxide formation energies	75
5.6	Relationship between charge transfer and voltage in electrode materials	77
5.7	Oxides	83
5.8	Benefits and drawbacks of hybrids compared to GGA+ U	84
5.9	Conclusion	85
6	Polaron migration and phase separation in $LiMnPO_4$ and $LiFePO_4$ using hybrid functionals	87
6.1	Polaronic conductivity in the $LiMnPO_4$ and $LiFePO_4$	87
6.2	Methods	88
6.2.1	Small polaron migration	88
6.2.2	Phase separation behavior	90
6.2.3	Computational methodology	90
6.3	Polaron bond lengths and electronic structure	91

6.4	Polaron migration barriers	92
6.5	Li_xMPO_4 formation energies	97
6.6	Intrinsic kinetic differences between the Mn and Fe olivines	99
6.7	Successes and limitations of HSE06	100
6.8	Conclusion	101
7	Approximating the electrochemical windows of room-temperature ionic liquids	103
7.1	Room-temperature ionic liquids as potential electrolytes	103
7.2	Systematic transversal of IL ion chemical space	105
7.3	Proxy measure for electrochemical stability	107
7.4	Geometry relaxation of cations and anions upon reduction and oxidation	111
7.5	Effect of alkylation on EAs of cations	112
7.6	Effect of alkylation on IEs of anions	116
7.7	Effect of functional group substitutions	117
7.8	IL design strategies	120
7.9	Conclusion	121
8	Conclusion	123
A	Calculated magnetic moments of Li_xMPO_4	127

List of Figures

1-1	Schematic of the operation of a typical Li-ion battery.	18
1-2	Structure of olivine LiMPO_4	19
1-3	Common IL cations. From left to right: 1-alkyl-3-methylimidazolium, 1-alkylpyridinium and N-methyl-N-alkylpyrrolidinium.	21
3-1	Phase diagrams for ternary subsystems of Li-Fe-P-O.	40
3-2	Li-Fe-P-O phase diagrams at less reducing environments.	42
3-3	Li-Fe-P-O phase diagrams at more reducing environments.	43
3-4	Li-Fe-P-O phase diagrams at highly reducing environments.	44
3-5	Li-Fe-P-O phase diagrams at extremely reducing environments.	45
3-6	Modified Ellingham diagram for reduction reactions in Li-Fe-P-O system.	49
4-1	Li-M-P-O (M = Fe, Mn, Co, Ni) phase diagrams for μ_{O_2} just below critical values where delithiated MPO_4 olivine decomposes. The composition of MPO_4 is marked with an X.	60
4-2	O_2 evolved vs temperature for delithiated MPO_4 (M=Fe, Mn, Co, Ni).	62
5-1	Difference between calculated and experimental Li intercalation potentials for GGA, GGA+ U , and HSE06.	74
5-2	Formation energies of oxides per O_2 calculated with GGA and HSE06 plotted against experimental formation enthalpies.[71, 60]	76

5-3	Isosurface of the difference between charge densities obtained with HSE06 and GGA+ U ($\rho^{\text{HSE06}} - \rho^{\text{GGA+U}}$). The yellow and blue represent the positive and negative 0.02 electron/ \AA^3 isosurfaces respectively. View along $[01\bar{1}]$, rendered using VESTA.[115]	78
5-4	Isosurface of the difference between charge densities obtained with HSE06 and GGA+ U ($\rho^{\text{HSE06}} - \rho^{\text{GGA+U}}$). The yellow and blue represent the positive and negative 0.02 electron/ \AA^3 isosurfaces respectively. . .	79
5-5	Isosurfaces of the change in charge density upon lithiation of NiPO_4 to LiNiPO_4 ($\rho_{\text{LiNiPO}_4} - \rho_{\text{NiPO}_4}$) with (a) GGA+ U and (b) HSE06. The yellow and blue represent the positive and negative 0.054 electron/ \AA^3 isosurfaces respectively. Only the NiO_6 octahedra is shown as no difference was visible on the P atom at the chosen isosurface value. . . .	81
5-6	Summed projected DOS of atoms having parallel magnetic moments in AFM LiNiPO_4 calculated using (a) GGA+ U and (b) HSE06. . . .	82
6-1	Single layer viewed in projection along the $[100]$ direction showing polaron hops considered. The lithium atom marked with the X is the atom removed when calculating polaron barriers in the presence of vacancies.	88
6-2	DOS stacked area plots for LiMPO_4 and MPO_4 olivines containing a single hole and electron polaron respectively. The height of each colored area shows the contribution of each orbital type at each energy level.	93
6-3	Isosurface of LiMPO_4 hole polaron differential charge density ($\rho_{\text{polaron cell}} - \rho_{\text{neutral cell}}$) at a 0.005 electron \AA^{-3} level calculated in HSE06. . .	94
6-4	Calculated free polaron migration barriers in HSE06 and GGA+ U . . .	95
6-5	Calculated bound polaron migration barriers in HSE06.	96
6-6	Formation energies of Li_xMPO_4 using different functionals.	98

7-1	Plot of the calculated vertical EAs against calculated adiabatic EAs for alkylated IL cations, and calculated vertical IEs against calculated adiabatic IEs for alkylated IL anions.	111
7-2	Effect of Increasing Alkylation on Vertical EA of IL Cations. XMIM refers to the 1-alkyl-3-methylimidazolium cation, where X ranges from ethyl (2 carbon atoms) to octyl (8 carbon atoms).	113
7-3	Effect of alkylation on the EA of 1-ethyl-3-methylimidazolium (EMIM) cation. The naming convention is based on the length of the alkyl chain attached to each ring atom, starting from the leftmost N atom and going around in a clockwise direction. Hence, Imi20100 \equiv EMI cation, Imi21100 \equiv 1-ethyl-2,3-dimethylimidazolium, etc. Imi30100 refers to the cation having an n-propyl group attached to the leftmost N atom, while Imi30100br refers to having an isopropyl group attached at the leftmost N atom.	115
7-4	Effect of increasing alkylation on vertical IP of IL anions.	116
7-5	Effect of functional group substitutions on EA of 1,2,3-trimethylimidazolium (TMIM). The change in EA from the TMI cation is plotted, i.e., difference in EA between the functionalized cation and the non-functionalized cation.	117
7-6	Effect of functional group substitutions on IE of PF ₅ CF ₃ . The change in IE from the PF ₅ CF ₃ anion is plotted, i.e., difference in IE between the functionalized anion and the non-functionalized anion.	118

List of Tables

3.1	Crystal structures and GGA+ U formation energies per formula unit (as listed) of phases in Li-Fe-P-O system.	38
3.2	Predicted phase equilibria under various oxidation and Li off-stoichiometry conditions.	52
5.1	Values of the U parameters in eV.	72
5.2	Average Li intercalation potentials vs. Li/Li ⁺ in volts, obtained using GGA, GGA+ U , and HSE06 for complete delithiation compared to experiment. Parentheses indicate the use of the GGA value ($U = 0$). Experimental potentials have an estimated error of ± 0.1 V.	73
6.1	Average M-O bond lengths of polaron and non-polaron sites in the Mn and Fe olivines in angstroms. Ranges are shown in brackets for the polaron sites.	91
7.1	Cations investigated.	107
7.2	Anions investigated.	107
7.3	Functional groups investigated and their known electron-donating (ED) and electron-withdrawing (EW) effects.[153]	108
A.1	Calculated magnetic moments on each Fe ion in the unit cell of Li _{x} FePO ₄ for the various functionals.	127
A.2	Calculated magnetic moments on each Mn ion in the unit cell of Li _{x} MnPO ₄ for the various functionals.	128

Chapter 1

Introduction

One of the key hurdles to clean energy is energy storage. For the foreseeable future, rechargeable lithium-ion batteries are the technology to beat in terms of delivering high energy densities at a reasonable cost and safety. Beyond current consumer electronics applications, Li-ion batteries are at the forefront of efforts to commercialize plug-in hybrid electric vehicles (PHEV) and hybrid electric vehicles (HEV) for the mass market.

The importance of Li-ion battery technology behooves its rapid development. Computational material design can help achieve this in two ways. Firstly, the advent of widely available computational power and efficient computational codes has provided a means to rapidly screen a large set of materials by computing key relevant properties, such as the voltage of a cathode or electrochemical window of an electrolyte, thereby accelerating the search for new and better materials. Secondly, first principles techniques allow us to study materials of interest in a virtual environment with absolute control over conditions, something not possible in an experimental setup. These highly controlled investigations provide insights into a material's intrinsic properties and how they can be optimized or improved. In this thesis, we leveraged on both these advantages of computational techniques to study cathode and electrolyte materials in Li-ion batteries.

The remainder of this chapter provides an introduction to Li-ion battery technology and the components studied in this thesis. The chapter concludes with an

overview and motivation of the research.

1.1 Anatomy of a lithium-ion battery

Figure 1-1 shows the operation of a typical Li-ion battery. Li-ion batteries operate by shuttling Li^+ ions between the cathode and anode through an electronically insulating, ion-conducting electrolyte. During discharge, lithium ions migrate from the anode, where they are at a higher chemical potential, through the electrolyte, and into the cathode, where they are at a lower chemical potential. At the same time, an electron travels through the external circuit to perform external work. The free energy change of the lithium migration process is the maximum reversible work that can be obtained. During charge, the application of an external potential forces lithium ions to migrate out of the cathode, through the electrolyte, and back into the anode.

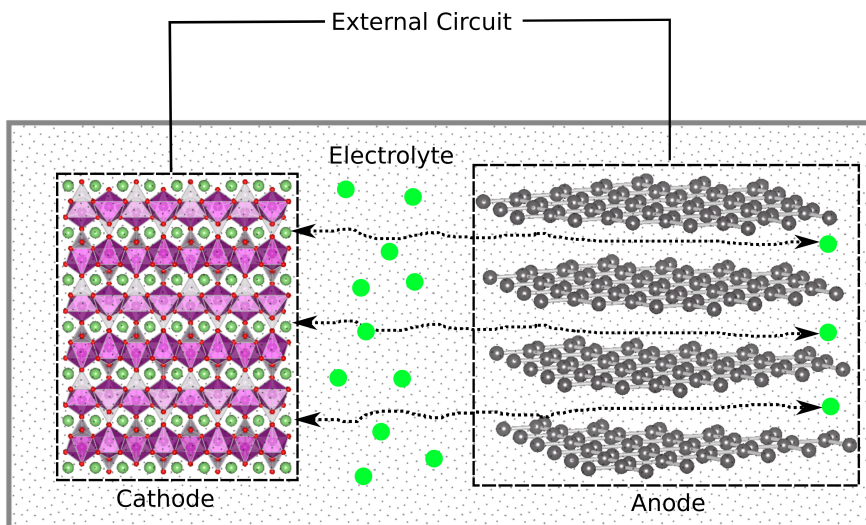


Figure 1-1: Schematic of the operation of a typical Li-ion battery.

1.1.1 Intercalation cathodes

Typically, both electrodes in a Li-ion battery are intercalation compounds, which as their name implies, store Li^+ by inserting them into their crystal structure in a topotactic manner. Currently, the anode used in most Li-ion batteries is based on

graphitic carbon, which stores up to one Li^+ for every six carbon atoms in between its graphene layers. Current cathodes are typically lithium transition-metal dischalcogenides, which contain interstitial sites that can be occupied by Li^+ . The insertion of each Li^+ is accompanied by the concomitant reduction of a transition metal ion to accommodate the compensating electron.

The earliest commercial intercalation cathode can be traced back to the work of Whittingham,[7] who first demonstrated electrochemical activity in layered LiTiS_2 in the 1970s. Layered LiCoO_2 , the cathode material that dominates the market in lithium batteries today, was discovered by Mizushima *et al.*[8] in 1980.

In recent years, olivine LiMPO_4 materials have emerged as promising cathodes for rechargeable lithium batteries.[9, 10, 11, 12, 13, 14, 15, 16, 17, 18] The olivine LiMPO_4 compounds have an orthorhombic $Pnma$ spacegroup (Fig. 1-2) where the transition metal (M) ions are sixfold coordinated by oxygen ions, forming layers of edge-sharing octahedra.

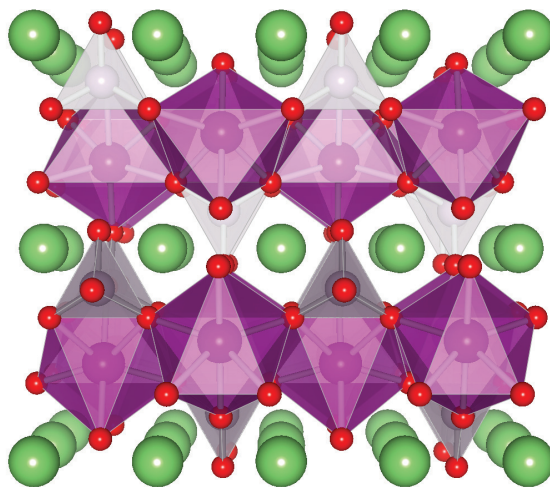


Figure 1-2: Structure of olivine LiMPO_4 .

LiFePO_4 [9], in particular, has already found widespread applications in industry due to its reasonable voltage of 3.5 V and theoretical capacity of 170 mAhg^{-1} , low cost and low toxicity, and high thermal stability. Because of its substantial potential, much research effort has been directed towards optimizing synthesis routes for LiFePO_4 cathodes. A variety of techniques have been developed to optimize the

electrode by controlling particle size and morphology and improving the electrical conductivity.[10, 14, 11, 19] Most of these techniques are based on the control of the oxidation environment and initial stoichiometry of precursors; the synthesis of LiFePO_4 requires reducing conditions, typically achieved via high temperatures, the use of carbon-containing precursors and/or reducing atmospheres such as an Ar atmosphere. The impurities formed are highly dependent on the stoichiometry and synthesis conditions.[20, 21, 22]

LiMnPO_4 , LiCoPO_4 and LiNiPO_4 can potentially deliver higher theoretical energy densities than LiFePO_4 due to their higher measured/predicted voltages of 4.1 V, 4.8 V and 5.1 V vs Li/Li^+ respectively.[23, 24, 18] Of these promising alternatives, LiMnPO_4 has garnered the most interest because its voltage of 4.1 V is higher than LiFePO_4 (3.5 V) but well within the limitations of current organic electrolytes. However, experimental investigations thus far have in general found poor rate performance in LiMnPO_4 due to low ionic and electronic conductivities,[25] a high surface energy barrier for Li diffusion,[26] or significant volume change at the phase boundary.[13, 16, 27] Two recent investigations by Kim *et al.*[28] and Chen *et al.*[29] have also demonstrated that while fully lithiated LiMnPO_4 remains stable up to fairly high temperatures, delithiated MnPO_4 decomposes at temperatures of around 150-200°C, evolving O_2 and heat in the process. This is in stark contrast to delithiated FePO_4 which has been shown to be stable for temperatures up to 500-600°C.[30] There is also evidence that the other higher voltage olivines, LiCoPO_4 and LiNiPO_4 , are even more thermally unstable upon delithiation.[31, 32].

1.1.2 Electrolytes

The electrolyte functions as a Li^+ conductor and comprises a solvent, typically a mixture of a cyclic carbonate such as ethylene carbonate (EC) and linear carbonate such as dimethyl carbonate (DMC), and a lithium salt, typically LiPF_6 . An ideal electrolyte should have a wide enough electrochemical window to accommodate the operating voltage of the battery, chemical stability against the electrodes and other components, a high ionic conductivity with extremely low electronic conductivity, low

flammability, and low cost. Current EC/DMC + LiPF₆ electrolytes are an imperfect compromise of these objectives. The electrochemical windows of EC/DMC + LiPF₆ electrolytes of up to approximately 5 V versus Li/Li⁺[33] are sufficient for current electrode systems, but would be severely tested by higher voltage cathodes (e.g., LiNiPO₄, which has a predicted voltage of 5.1 V[23]). Current electrolytes are also unstable against the graphitic anode and function by forming a passivating solid-electrolyte interphase (SEI) whose composition, structure and transport mechanisms are still not well understood.[33]

Recently, there has been a steadily growing interest in using room-temperature ionic liquids (ILs) as electrolytes in rechargeable lithium batteries.[34, 35, 36, 37] ILs are liquids that comprise entirely of ions at room temperature. IL cations are typically bulky, asymmetric organic cations such as 1-alkyl-3-methylimidazolium, 1-alkylpyridinium and N-methyl-N-alkylpyrrolidinium (see Figure 1-3). For lithium battery applications, the IL anions chosen are based on those in lithium salts commonly added to current electrolytes to aid lithium conductivity, such as BF₄, PF₆ and bis(trifluoromethylsulfonyl)-imide.

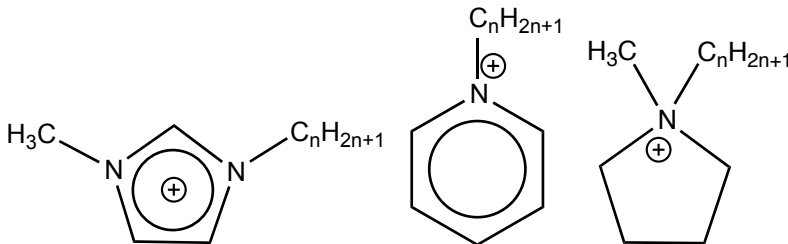


Figure 1-3: Common IL cations. From left to right: 1-alkyl-3-methylimidazolium, 1-alkylpyridinium and N-methyl-N-alkylpyrrolidinium.

The properties of ILs are highly dependent on the cations and anions used and the functional groups attached to those ions. As a class of materials, ILs generally exhibit low volatility, low flammability and high thermal stability, which provides significant safety advantages over flammable organic compounds. Many ILs also have wide electrochemical windows of approximately 5-6 V,[38] which are considerably larger than the 4.3-4.4 V electrochemical windows of current organic electrolytes. A more electrochemically stable electrolyte could unlock the potential of high-voltage

cathodes with higher power density. For example, LiNiPO_4 , which is predicted to have a potential near 5 V,[23] would have 50% higher energy density than the Fe-based LiFePO_4 system currently under development for HEVs. The main disadvantage of ILs as Li-ion battery electrolytes is their generally higher viscosity and lower ionic conductivities compared to current organic electrolytes, especially after the addition of a lithium salt.

1.2 Motivation and overview

While Li-ion battery technology has come a long way since its early beginnings, significant advances are necessary for Li-ion batteries to move beyond small-scale consumer electronics applications into large scale applications such as PHEVs and HEVs. In its 2007 Draft Plug-In Hybrid Electric Vehicle R&D Plan, the US Department of Energy has identified new materials development, especially the development of new transition-metal oxide cathodes and electrolyte materials, as an important research thrust.[39] To meet the PHEV 40-mile electric range target, the specific energy of current Li-ion batteries must approximately double. The specific energy of a battery is given by its voltage multiplied by its specific capacity. Hence, a cathode with higher voltage and/or higher achievable capacity, combined with an stable electrolyte that supports operation at that voltage, will increase the overall specific energy of a battery.

Computationally, the voltage of a cathode material can be predicted by calculating the change in the lithium chemical potential as lithium shuttles between the cathode and anode. The theoretical rate capability of a cathode is determined by the rate limiting step, which could be set by either the ionic or electronic conductivities.

Phase diagrams representing the thermodynamic phase equilibria of multi-component systems reveal fundamental material aspects regarding the processing and reactions of materials. With the advent of relatively cheap computational power, it is now possible to calculate the energies of all compounds in a multi-component system to computationally determine its phase diagram. In this thesis, we computed the technologically

important Li-Fe-P-O quaternary phase diagram as a function of oxidation conditions using first principles calculations. The computed Li-Fe-P-O phase diagram have provided insights into the phase equilibria for different LiFePO_4 off-stoichiometries and guided experimental efforts to optimize synthesis approaches that remove ionic kinetic limitations.

Thermal stability remains an important issue in large scale applications. At elevated temperatures, cathode materials may potentially release oxygen, which can combust the electrolyte and lead to runaway reactions and fire. While the discharged cathode is usually relatively stable with respect to oxygen release, cathodes based on layered LiCoO_2 , LiNiO_2 , and spinel LiMn_2O_4 decompose with oxygen evolution[40] when heated in the highly oxidized charged state. Olivine LiFePO_4 on the other hand, offers much better thermal stability, and it has been tacitly assumed that all materials based on the phosphate polyanion would share this advantage.[13, 41] In this thesis, we developed a technique to study the thermal stability of cathode materials using first principles phase diagrams and applied the technique to compare the relative thermal stabilities of the charged olivine phosphates.

Previous theoretical work has shown that standard local density (LDA) and generalized gradient approximations (GGA) to density functional theory (DFT) are generally insufficient to treat electron correlation in the localized d states in transition metal oxides and tends to lead to an over-delocalization of the d electrons.[42, 43, 44] A more sophisticated treatment with the application of a Hubbard U term to penalize partial occupancies in the site-projected d orbitals is needed. Exact Hartree-Fock (HF) exchange cancels the unphysical self-interaction by construction.[45] As such, hybrid functionals, which incorporate a fraction of exact exchange, can be considered an alternative approach to dealing with the over-delocalization of d -orbitals in transition metal ions by conventional semi-local functionals, albeit at a significantly higher computational cost. The advantage of hybrid functionals over GGA+ U is the lack of a species-specific U parameter and perhaps more importantly, a more universal treatment of the self-interaction error over all species and occupied states rather than specific atomic orbital projections on specific ions. In this thesis, we investigated the

merits of the Heyd-Scuseria-Ernzerhof (HSE06)[3, 4] hybrid functional for predicting voltages and redox energies, and applied the same functional to study relative polaron conductivities and phase separation energies in the LiMnPO_4 and LiFePO_4 materials.

Last but not least, better cathode materials require better electrolytes. Room-temperature ionic liquids (ILs) are not only safer, but also have the potential to unlock higher voltage cathode materials. In this thesis, we systematically probed the large chemical space of IL ion structures to obtain broad trends in the gas-phase electron affinities of IL cations and ionization energies of IL anions using computational chemistry methods. These trends are consistent with experimental observations and provides a tool to screen IL ions for applications in Li-ion batteries.

This thesis is divided into the following chapters:

- Chapter 2 provides an overview of the thermodynamic and computational techniques to develop phase diagrams from first principles calculations.
- Chapter 3 discusses the Li-Fe-P-O phase diagram computed using the above techniques and its relevance and application.
- Chapter 4 discusses the extension of computational phase diagrams to the prediction of the thermal stabilities of the olivine LiMPO_4 ($M = \text{Fe, Mn, Co, Ni}$) materials, and the use of the technique as a high-throughput cathode design criteria.
- Chapter 5 compares the performance of the HSE06 functional in predicting voltages and redox energies with the predictions of standard DFT functionals based on $\text{GGA}+U$ and GGA.
- Chapter 6 is devoted to the study of polaron migration barriers and phase separation energies in LiMnPO_4 and LiFePO_4 using the HSE06 functional.
- Chapter 7 presents our systematic investigation of the gas phase electron affinities of IL cations and ionization energies of IL anions using computational chemistry methods.

- Chapter 8 concludes this thesis.

Chapter 2

Phase diagrams from first principles

In this chapter, we outline the general thermodynamic methodology to construct phase diagrams using first principles calculations. The methodology is based on the technique used by Wang *et al.*[46] to determine the ternary phase diagrams of Li-M-O (M = Ni, Co, Mn) systems to investigate the thermal stability of the layered LiCoO₂, LiNiO₂ and LiMnO₂ materials. In this thesis, we have made a few notable extensions to that technique, including an oxygen grand potential construction for studying systems that are open with respect to oxygen gas, which has the added benefit of simplifying phase diagram analysis for the four-component systems of interest. The oxygen chemical potential is treated as an external parameter and can be related to experimental conditions such as temperature and oxygen partial pressures using simple thermodynamic relations.

Because our interest are primarily in the Li-M-P-O quaternary systems, we have adopted a notation based on this system in the following derivations without loss of generality.

2.1 Compositional phase diagrams

To construct a phase diagram, one would need to compare the relative thermodynamic stability of phases belonging to the system using an appropriate free energy model. For an isothermal, isobaric, and closed Li-M-P-O system, the relevant thermodynamic potential is the Gibbs free energy, G , which can be expressed as a Legendre transform of the enthalpy, H , and internal energy, E , as follows:

$$\begin{aligned} G(T, P, N_{Li}, N_M, N_P, N_O) = & E(T, P, N_{Li}, N_M, N_P, N_O) \\ & - TS(T, P, N_{Li}, N_M, N_P, N_O) \\ & + PV(T, P, N_{Li}, N_M, N_P, N_O) \end{aligned}$$

where T is the temperature of the system, S is the entropy of the system, P is the pressure of the system, V is the volume of the system, and N_i is the number of atoms of species i in the system.

In the olivine Li-M-P-O systems of interest, we are primarily comparing the relative stability of condensed phases, for which $P\Delta V$ is generally small and the PV term may therefore be neglected. At 0K, the expression for G simplifies to just E . Normalizing E with respect to the total number of particles in the system, we obtain $\bar{E}(0, P, x_{Li}, x_M, x_P, x_O)$ where $x_i = \frac{N_i}{N_{Li}+N_M+N_P+N_O}$ is the fraction of species i in the system. By taking the convex hull [47] of \bar{E} for all phases belonging to the N -component system and projecting the stable nodes into the $(N - 1)$ -dimension composition space, one can obtain the 0K phase diagram for the closed system at constant pressure. The convex hull of a set of points is the smallest convex set containing the points. For instance, to construct a 0K, closed Li-M-P-O system phase diagram, the convex hull is taken on the set of points in $(\bar{E}, x_{Li}, x_M, x_P)$ space with x_O being related to the other three composition variables by $x_O = 1 - x_{Li} - x_M - x_P$.

2.2 Oxygen grand potential phase diagrams

The description of a closed four-component system at constant temperature and pressure requires three-dimensional space and can be represented in the form of a composition tetrahedron. However, given the large number of phases present in the Li-M-P-O system, this representation is not one that is amenable to easy analysis. Furthermore, such a phase diagram, which describes phase equilibria in an environment with controlled Li, M, P and O compositions, is not reflective of the environments of interest.

Typically, synthesis and thermal stability investigations of LiMPO_4 olivines are conducted under controlled oxygen chemical potential conditions. LiFePO_4 synthesis requires reducing environments, which are usually achieved using relatively high temperature processing (typically 600-850°C) and a low oxygen environment such as an Ar or N_2 atmosphere. In some cases, even more extreme reducing environments are achieved with the presence of carbon or H_2 as reducing agents. Thermal stability experiments, such as thermogravimetric analysis, are also typically conducted under controlled atmospheres.

Under these conditions, the system of interest is an isothermal, isobaric system that is open with respect to oxygen and closed with respect to the other components, rather than a completely closed system. The key control variable is then the oxygen chemical potential, μ_{O_2} . The relevant thermodynamic potential to study phase equilibria with respect to an oxidizing or reducing environment is the oxygen grand potential, defined by the following expression:

$$\begin{aligned} \phi(T, P, N_{\text{Li}}, N_{\text{M}}, N_{\text{P}}, \mu_{\text{O}_2}) &= G(T, P, N_{\text{Li}}, N_{\text{M}}, N_{\text{P}}, \mu_{\text{O}_2}) \\ &\quad - \mu_{\text{O}_2} N_{\text{O}_2}(T, P, N_{\text{Li}}, N_{\text{M}}, N_{\text{P}}, \mu_{\text{O}_2}) \end{aligned} \quad (2.1)$$

$$\begin{aligned} &\approx E(T, P, N_{\text{Li}}, N_{\text{M}}, N_{\text{P}}, \mu_{\text{O}_2}) \\ &\quad - TS(T, P, N_{\text{Li}}, N_{\text{M}}, N_{\text{P}}, \mu_{\text{O}_2}) \\ &\quad - \mu_{\text{O}_2} N_{\text{O}_2}(T, P, N_{\text{Li}}, N_{\text{M}}, N_{\text{P}}, \mu_{\text{O}_2}) \end{aligned} \quad (2.2)$$

where the PV term is again ignored.

Normalizing ϕ with respect to Li-M-P composition and dropping the explicit expression of the functional dependence of E , S and N_{O_2} on the right-hand side henceforth for brevity, we obtain:

$$\bar{\phi}(T, P, x_{Li}, x_M, x_P, \mu_{O_2}) \approx \frac{E - TS - \mu_{O_2} N_{O_2}}{N_{Li} + N_M + N_P} \quad (2.3)$$

where $x_i = \frac{N_i}{N_{Li} + N_M + N_P}$ is the fraction of component i in Li-M-P composition space.

To formally introduce temperature into *ab initio* phase stability calculations, one would usually need to take into account all the relevant excitations (e.g., vibrational, configurational, and electronic) that contribute to entropy.[48, 49, 50, 51] However, for our chosen system, a few simplifying assumptions can be made that allow us to obtain a useful approximate phase diagram with less effort. For an open system with respect to oxygen, phase equilibria changes take place primarily through reactions involving the absorption or loss of oxygen gas. In such reactions, the reaction entropy is dominated by the entropy of oxygen gas, and the effect of temperature is mostly captured by changes in the oxygen chemical potential. The oxygen chemical potential is related to the temperature and oxygen partial pressure by the following equations:

$$\mu_{O_2}(T, p_{O_2}) = \mu_{O_2}(T, p_0) + kT \ln \frac{p_{O_2}}{p_0} \quad (2.4)$$

$$= E_{O_2} + kT - TS_{O_2}^{T, p_0} + kT \ln \frac{p_{O_2}}{p_0} \quad (2.5)$$

where p_{O_2} is the oxygen partial pressure, p_0 is a reference oxygen partial pressure, $S_{O_2}^{T, p_0}$ is the oxygen entropy at the reference oxygen partial pressure, E_{O_2} is the oxygen energy, and k is Boltzmann's constant. Equation 2.5 is obtained by writing the chemical potential as a Legendre transform of the internal energy, with an ideal gas assumption made for the PV term.

Because the TS term in equation 2.3 is the entropy contribution of the solid state system to $\bar{\phi}$, it can be neglected compared to the entropy effect of μ_{O_2} on $\bar{\phi}$ (due to the much larger contribution of $N_{O_2} s_{O_2}$ compared to S). The expression for $\bar{\phi}$ then

simplifies to the following:

$$\bar{\phi}(\mu_{O_2}, x_{Li}, x_{Fe}, x_P) \approx \frac{E - \mu_{O_2} N_{O_2}}{N_{Li} + N_{Fe} + N_P} \quad (2.6)$$

Using the above assumptions, the effect of temperature and oxygen partial pressure can be fully captured in a single variable, μ_{O_2} , with a more negative value corresponding to higher T or lower p_{O_2} (as can be seen from equation 2.5).

Varying μ_{O_2} , the Li-M-P-O phase diagram can be constructed as constant μ_{O_2} sections in $(\mu_{O_2}, x_{Li}, x_M, x_P)$ space by taking the convex hull of $\bar{\phi}$ for all phases at a particular μ_{O_2} and projecting the stable nodes onto a two-dimensional Li-M-P Gibbs triangle. Each constant μ_{O_2} phase diagram then represents phase equilibria at a particular oxidation environment, and each point in the phase diagram provides the phase or combination of phases with the lowest $\bar{\phi}$.

2.3 First principles energies from density functional theory

In this thesis, we have extracted all known ordered compounds in the Inorganic Crystal Structure Database (ICSD)[52] belonging to the quaternary Li-M-P-O (M = Fe, Mn, Ni, Co) systems, and calculated the energies for these using the generalized gradient approximation (GGA) to density functional theory (DFT) and the GGA+ U extension to it.[53] Projected augmented wave (PAW)[54] pseudopotentials were used, as implemented in the Vienna *ab initio* simulation package (VASP).[55] An energy cutoff of 500 eV and appropriate k -point meshes were chosen so that total energies converged within 3 meV per formula unit with the atomic positions and lattice vectors fully relaxed. All calculations were spin-polarized, but no attempt was made to find anti-ferromagnetic solutions except for the iron oxides for which the magnetic ground states are well-known.

The DFT+ U [53] methodology was chosen for its appropriateness for the redox reactions studied in this work. It is well-known that first principles calculations

within the local density approximation (LDA) or generalized gradient approximation (GGA) lead to considerable error in calculated redox energies of transition metal oxides. This error arises from the self-interaction in LDA and GGA, which is not canceled out in redox reactions where an electron is transferred between significantly different environments, such as between a metal and a transition metal or between a transition metal and oxygen. Zhou *et al.*[23] have demonstrated that a GGA+ U treatment of the localized d orbitals with an explicit Hubbard term to cancel the self-interactions lead to significantly improved accuracy in the calculated redox energies and Li-insertion voltages for lithium transition metal cathodes. Similarly, Wang *et al.*[56, 46] showed the benefit of the U correction in improving the calculated oxidation energies for transition metal oxides.

Throughout this thesis, the rotationally invariant approach to the LSDA+ U introduced by Dudarev *et al.*[57] was used in which there is only one effective U parameter. In the literature, there are two common methods to determine the appropriate U value:

1. The self-consistent linear response theory approach of Cococcioni *et al.*[58] The energies for the Li-Fe-P-O phase diagram in Chapter 3 and the GGA+ U voltages in Chapter 5 were calculated using U values determined from this approach as our primary interest in these works were reproducing and comparing redox energies using “parameter-free” functionals.
2. Fitting to reproduce experimental oxidation energies for transition metal oxides, as implemented by Wang *et al.*[59] For the thermal stability investigations in Chapter 4, the calculations were performed using our high-throughput computation infrastructure. In that setup, we adopted Wang *et al.*’s method [59] of fitting the calculated binary oxide formation enthalpies to experimental values from the Kubaschewski tables.[60] The rationale for adopting this approach was that to ensure that we obtain accurate formation energies. In any case, the U values determined using this approach are usually very close to the self-consistent value determined in method (1), and we do not expect significantly

different results.

2.4 Limitations

Several limitations are inherent in our first principles approach to developing phase diagrams.

Firstly, our phase diagrams are developed from phases in the ICSD database. Our analysis, therefore, by definition does not include phases which have not yet been discovered. However, we do not foresee this to be a major issue as the Li-M-P-O systems are fairly well-studied, and most of the relevant phases should have already been identified. A more elaborate search for unknown compounds would require a method to predict likely crystal structures for a large number of possible stoichiometries. Hautier *et al.*[61] has recently developed such a method based on a combination of machine learning techniques and high-throughput *ab initio* phase diagrams.

Secondly, we have made several key assumptions in our free energy model, most notably considering only the entropic contributions of gaseous phases. This assumption seems reasonable for the phase equilibria we are interested in, where phase transitions consist primarily of solid state changes with the absorption or release of gases. It should be noted, however, that the predicted transition temperatures are likely to be overestimated as the entropy terms we neglected in the solid state would lower their free energy somewhat.

Finally, while the GGA+ U methodology chosen for our DFT computations has been shown to be useful in obtaining accurate redox energies, the appropriate values of U are dependent on the crystal environment and valence state of the transition metal ion. However, we expect major inaccuracies only for reactions involving metallic states for which the electrons are no longer atomic-like.

Chapter 3

The Li-Fe-P-O oxygen grand potential phase diagram

3.1 The LiFePO_4 cathode material

Since the pioneering work of Padhi *et al.*, [9] olivine LiFePO_4 has become one of the most promising cathode materials and is already under active commercialization today. LiFePO_4 has a reasonable theoretical capacity of 170 mAhg^{-1} and voltage of 3.5 V, low materials cost and low toxicity. Because of its substantial potential, much research effort has been directed towards optimizing synthesis routes for LiFePO_4 cathodes. A variety of techniques have been developed to control particle size and morphology, as well as improve the electrical conductivity of the electrode through coating with conducting phases (e.g., carbon or metallic iron phosphides) or aliovalent doping. [19] Investigations by Herle *et al.* [20] and Delacourt *et al.* [62] attributed the increase in conductivity of off-stoichiometric, aliovalently-doped LiFePO_4 to a percolating network of iron phosphides and phosphocarbides believed to be formed from carbothermal reduction of LiFePO_4 or $\text{Fe}_2\text{P}_2\text{O}_7$. More recently, Rho *et al.* [21] used a combination of Mössbauer and X-ray photoelectron spectroscopy to show that under most synthesis conditions in inert or reducing atmospheres, FeP and Fe_2P , along with Li_3PO_4 , are formed on the surface via surface reduction at temperatures as low as 600°C . Ellis *et al.* [22] also recently investigated the impact of synthesis conditions on

the conductivity and electrochemical performance of various lithium transition metal phosphates. They found that using H_2 or NH_3 gas as a reducing agent, they were able to achieve the reduction of Li-deficient LiFePO_4 to iron phosphides at lower temperatures and shorter sintering periods than when using carbon alone. They claimed that this reduced particle growth and carbon consumption, thereby significantly improving electrochemical performance.

We can see, therefore, that a key factor to optimizing synthesis approaches for LiFePO_4 is a thorough understanding of phase equilibria under stoichiometric and off-stoichiometric conditions. LiFePO_4 is typically synthesized under highly reducing conditions to avoid the formation of Fe^{3+} . Often, an excess of lithium is introduced to compensate for its high volatility. Depending on the precursors used (e.g., carbon containing or otherwise), the exact synthesis environment (temperatures, Ar or N_2/H_2 atmosphere) and the degree and nature of off-stoichiometry, different secondary phases may be formed in addition to LiFePO_4 , either during synthesis or subsequent re-oxidation under normal operating conditions. The nature of such “impurity” phases can have a significant impact on the performance of the electrode. The presence of undesirable or inactive phases may at best reduce the capacity of the electrode, and at worst, seriously degrade electrochemical performance. On the other hand, some secondary phases may improve the performance of the electrode, for instance, by acting as Li^+ or electron conduits.

A Li-Fe-P-O phase diagram would provide useful insights into experimental findings on LiFePO_4 and also serve as a guide for future experimental efforts to optimize synthesis approaches for LiFePO_4 . In this thesis, we have constructed the phase diagram for the quaternary Li-Fe-P-O system as a function of oxidation conditions using the first principles techniques outlined in Chapter 2.[1] Using the information on phase relations garnered from the phase diagram, we were then able to construct an Ellingham-type diagram for reactions of interest using a combination of total energies obtained from first principles calculations and experimental entropy data of gaseous phases.

3.2 Calculated energies of Li-Fe-P-O phases

The GGA+ U calculated energies and structures of the Li-Fe-P-O compounds studied in this work are presented in Table 3.1. All energies are presented as per formula unit (f.u.) formation energies, E_f , from the elemental standard states, Li, Fe, P and O_2 . Because the olivine $LiFePO_4$ system was the focus of our investigation, the U value used for Fe was 4.3 eV, based on the average of the self-consistently determined U values for Fe^{2+} and Fe^{3+} in the olivine system calculated by Zhou *et al.*[23] However, the value of U tends to become smaller as the valence state of Fe decreases. Hence, the U value used may be somewhat too small for oxidized states (e.g., Fe_2O_3) and too large for reduced states (e.g., FeO). In particular, we expect considerable error in the calculated energies of metallic systems such as Fe metal and the iron phosphides, Fe_xP_y , where the d orbitals are no longer atomic-like, and the GGA+ U methodology is less applicable.

3.3 Verification of calculated ternary sub-system phase diagrams

To verify that the calculated energies reasonably reflect the relative stability of the various phases, we first constructed the phase diagrams of the various ternary sub-systems at 0 K, i.e., the Li-P-O, Li-Fe-O, Fe-P-O and Li-Fe-P systems, and compared these with known experimental phase diagrams for these systems.[63, 64, 65, 66, 67] It should be noted, however, that the experimental phase diagrams are generally for non-zero temperatures while the calculated phase diagrams represent phase equilibria at 0 K. Hence, some differences between the experimental and first principles phase diagrams are to be expected.

The phase diagrams constructed from first principles calculations are given in Figure 3-1. Only the section of the Fe-P-O phase diagram bounded by the oxides is shown given the large number of phases in this system. For the ternary diagrams with oxygen as a component, the reference O_2 energy used includes the constant -1.36 eV

Table 3.1: Crystal structures and GGA+ U formation energies per formula unit (as listed) of phases in Li-Fe-P-O system.

Phase	Crystal Struct.	E_f (eV ^a)	Phase	Crystal Struct.	E_f (eV)
Li ₂ O	Fm $\bar{3}$ m	-6.200	LiFeO ₂	R $\bar{3}$ m	-9.156
Li ₂ O ₂	P6 ₃ /mmc	-7.040	Li ₅ FeO ₄	Pbca	-21.883
FeO	Fm $\bar{3}$ m	-4.095	Li ₃ PO ₄	Pnma	-22.189
Fe ₂ O ₃	R $\bar{3}$ c	-11.250	Li ₄ P ₂ O ₇	P2 ₁ /c1	-36.022
Fe ₃ O ₄	Fd $\bar{3}$ m	-15.682	LiPO ₃	P2/c	-13.685
Fe ₃ P	I $\bar{4}$	-1.114	Fe ₉ (PO ₄)O ₈	Cmmm	-47.628
Fe ₂ P	Pnm	-0.876	Fe ₃ (PO ₄)O ₃	R3m	-26.078
FeP	Pnma	-0.339	Fe ₄ (PO ₄) ₂ O	P2 ₁ /c	-38.360
FeP ₂	P $\bar{6}$ 2m	-0.601	Fe ₂ PO ₄ O	Pnma	-20.143
FeP ₄	P2 ₁ /c	-1.265	Fe ₃ (PO ₄) ₂	P2 ₁ /c	-34.187
P ₄ O ₁₈	P2 ₁ 2 ₁ 2 ₁	-32.042	Fe ₇ (PO ₄) ₆	P $\bar{1}$	-95.984
P ₂ O ₅	Pnma	-17.343	Fe ₂ P ₂ O ₇	C $\bar{1}$	-29.097
P ₄ O ₉	R $\bar{3}$ c	-31.265	FePO ₄	Pnma	-15.309
(P ₄ O ₆)O ₂	C2/c	-27.792	Fe ₇ (P ₂ O ₇) ₄	C222 ₁	-113.022
P ₄ O ₇	P2 ₁ /c	-24.028	Fe ₃ (P ₂ O ₇) ₂	Pnma	-55.034
P ₄ O ₆	P2 ₁ /m	-20.173	Fe ₄ (P ₂ O ₇) ₃	P2 ₁ /c	-80.173
LiP ₇	I4 ₁ /acd	-2.261	Fe ₂ P ₄ O ₁₂	C2/c	-47.801
LiP ₅	Pna2 ₁	-1.873	Fe(PO ₃) ₃	Cc	-33.953
LiP	P2 ₁ /c	-1.193	FeP ₄ O ₁₁	C $\bar{1}$	-41.533
Li ₃ P ₇	P2 ₁ 2 ₁ 2 ₁	-4.619	LiFePO ₄	Pnma	-18.853
Li ₃ P	P6 ₃ /mmc	-2.944	Li ₃ Fe ₂ (PO ₄) ₃	P2 ₁ /c	-53.192
LiFeP	P4/nmm	-1.238	LiFeP ₂ O ₇	P2 ₁	-29.376
LiFe ₅ O ₈	P4 ₃ 32	-30.650	LiFeP ₃ O ₉	P2 ₁ 2 ₁ 2 ₁	-37.523
Li ₃ Fe ₅ O ₈	P4 ₃ 32	-35.668	Li ₉ Fe ₃ (P ₂ O ₇) ₃ (PO ₄) ₂	P $\bar{3}$ c1	-132.471

^a1 eV/f.u. = 96.49 kJ/mol = 23.06 kcal/mol

shift to the oxygen enthalpy determined by Wang *et al.*[56] to correct for the error associated with the well-known over-binding of O₂ in GGA. This reference energy has no effect on the constant μ_{O_2} phase diagram but only modifies the scale of the oxygen chemical potential. Comparing the experimental and calculated diagrams, the following key observations can be made:

1. Li-P-O system: All compounds present in the experimental Li₂O-P₂O₅ phase diagram at 500°C[63] are present in our calculated diagrams. Of the 5 known Li-P binary phases,[68] LiP₇, LiP, Li₃P and Li₃P₇ are present in our phase diagram, while LiP₅ is only slightly above the convex hull.
2. Li-Fe-O system: Our phase diagram correctly reflects the stable compounds of LiFeO₂ and Li₅FeO₄ in the experimental diagram at 400°C.[64] However, instead of LiFe₅O₈, the lithiated form, Li₃Fe₅O₈, is present in our phase diagram.
3. Fe-P-O system: The experimental Fe-P-O phase diagram for Fe/P \geq 1 at 900°C has been established by Modaressi *et al.*[65] Of the nine ternary phases identified by Modaressi in this region, five are present in our calculated phase diagram (Fe₃(PO₄)₂, Fe₄(PO₄)₂O, Fe₂P₂O₇, Fe₇(PO₄)₆ and FePO₄). Fe₃(PO₄)O₃, Fe₂(PO₄)O and Fe₉(PO₄)O₈ are present in the experimental diagram but not present in our calculated diagram, even though these phases were considered in our calculations. The experimental diagram also identifies Fe₅(PO₄)₃O to be a stable phase, though this phase was not included in our computations as it is not in the ICSD database. For Fe/P <1, our calculated phase diagram identifies Fe₃(P₂O₇)₂, Fe₄(P₂O₇)₃, FeP₄O₁₁, Fe₂P₄O₁₂ and Fe(PO₃)₃ to be stable phases.
4. Li-Fe-P system: Compared with the experimental Li-Fe-P phase diagram at 800°C,[66] the binary Li₃P, LiP, Fe₃P and Fe₂P phases are present in our calculated diagram. However, FeP and the only known ternary phase, LiFeP,[69, 70] are not stable phases in our calculated phase diagram. Compared with the experimental binary Fe-P phase diagram,[67] all the iron phosphide phases are present in our calculated diagram except FeP and FeP₂. As mentioned in the

previous section, we expect significant errors in the calculated energies of metallic phases such as Fe metal and the iron phosphides as the GGA+ U methodology is less applicable. Indeed, using GGA energies (without the + U extension) results in a Li-Fe-P phase diagram (not shown) that is more consistent with the experimental diagram. With the exception of Fe_3P , all other phases present in the experimental diagram are present in the GGA phase diagram. However, the + U extension is necessary to obtain accurate redox energies for the iron oxide and phosphate phases, which are the phases of interest in this work. Hence, GGA+ U energies of all phases were used in constructing the phase diagram.

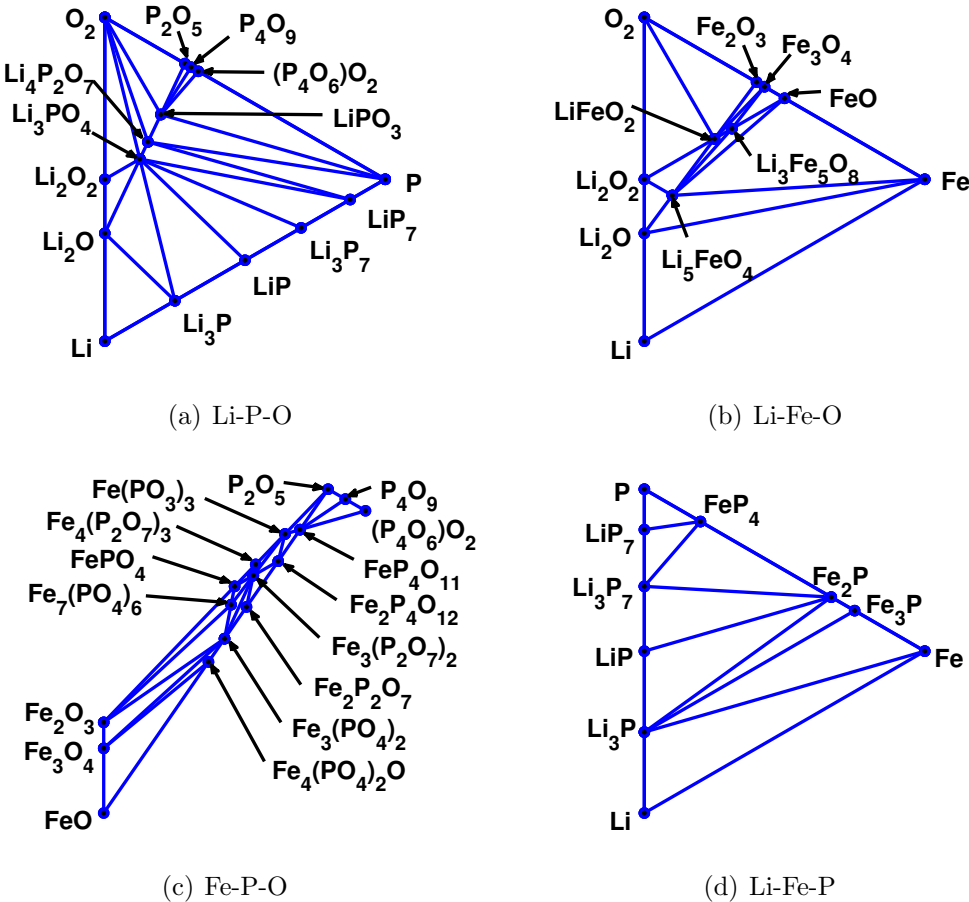
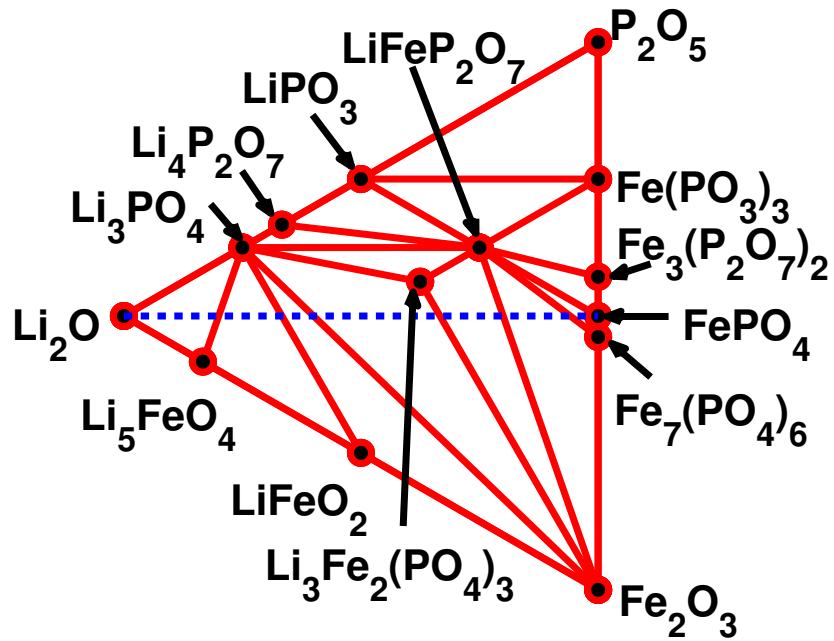


Figure 3-1: Phase diagrams for ternary subsystems of Li-Fe-P-O.

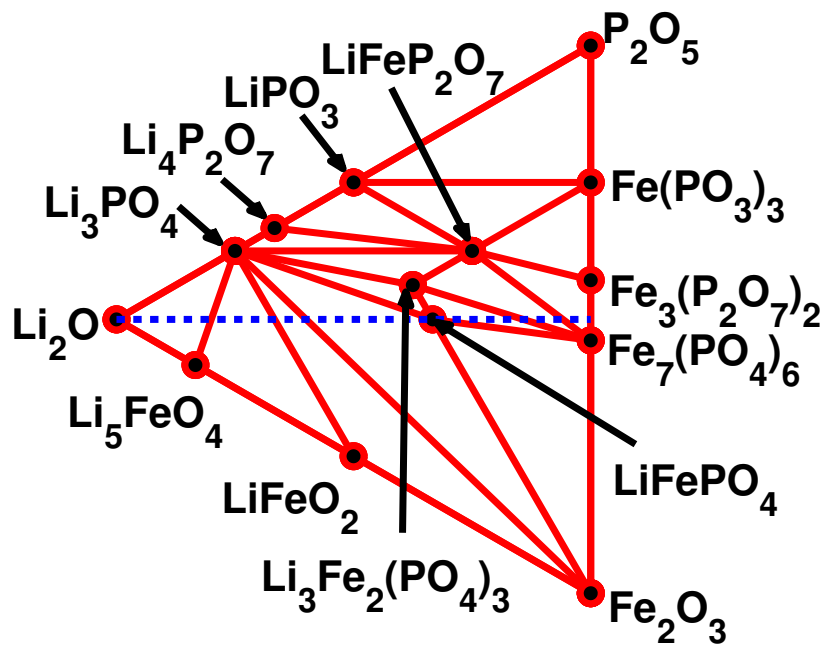
3.4 Constant μ_{O_2} phase diagrams

Using the calculated energies and the methodology outlined in Chapter 2, we constructed a series of phase diagrams at constant μ_{O_2} , given in Figures 3-2 to 3-5. Diagrams at lower μ_{O_2} represent more reducing environments, which correspond to higher temperatures and/or lower oxygen partial pressures and/or the presence of reducing agents, while higher μ_{O_2} represents less reducing (or more oxidizing) environments. The values of μ_{O_2} were chosen so as to present diagrams at key transition μ_{O_2} , i.e., values of μ_{O_2} where an important phase of interest (say LiFePO_4) is formed or removed. Figure 3-2 shows diagrams at mildly reducing environments in which the monoclinic $\text{Li}_3\text{Fe}_2(\text{PO}_4)_3$ phase is still present, and most Fe-containing phases have Fe in the 3+ oxidation state. At $\mu_{O_2} = -11.52$ eV, LiFePO_4 appears as the first stable Fe^{2+} -containing phase. As the environment becomes more reducing, phases containing Fe^{3+} are progressively being reduced to Fe^{2+} . Figure 3-3 shows phase diagrams where mixed valence phosphates, such as $\text{Fe}_7(\text{PO}_4)_6$, are being reduced to Fe^{2+} phases. At even more reducing environments (Figure 3-4), Fe^{2+} becomes the dominant valence state for Fe. Finally, at the extremely reducing environments represented by Figure 3-5, the iron phosphates are reduced to the metallic iron phosphides (Fe valence of 0) and eventually, LiFePO_4 itself is reduced. The reduction of the remaining highly stable oxygen-containing phases (Li_3PO_4 and Li_2O) takes place at conditions much more reducing than those of interest in this work. Under those conditions, the ternary Li-Fe-P phase (Figure 3-1(d)) is reproduced.

Also plotted in all the phase diagrams are dotted lines representing the path of Li off-stoichiometry with respect to LiFePO_4 . Compositions to the left of LiFePO_4 have Li-excess, while compositions to the right have Li-deficiency. For compositions that do not lie at a stable node on the phase diagram, the phases in equilibrium are given by the vertices of the triangle bounding that composition. For instance, at $\mu_{O_2} = -16.70$ eV, the phase diagram indicates that a Li-deficient composition ($\text{Li}_{1-x}\text{FePO}_4$) will consist of LiFePO_4 , FeP_4 and Fe_2P at equilibrium.

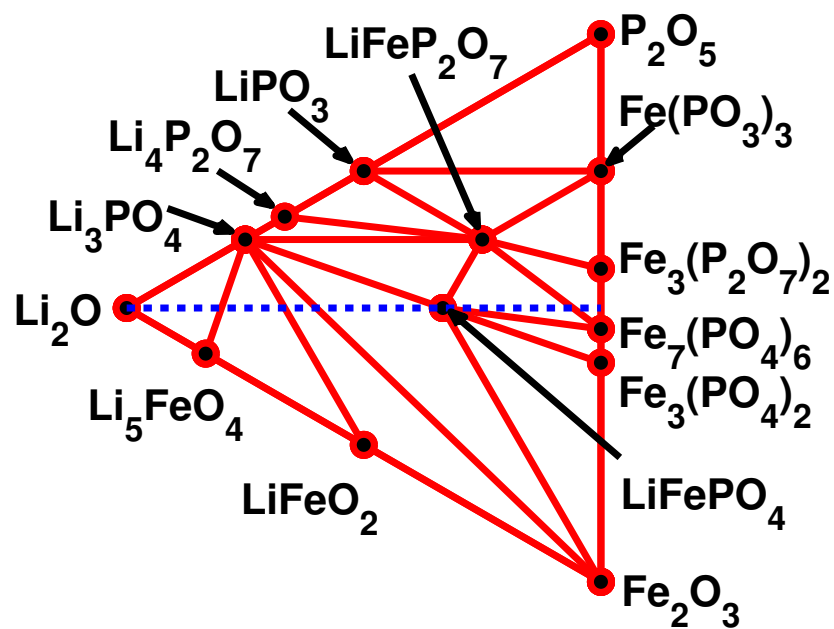


(a) $\mu_{O_2} = -10.50$ eV, $Fe_7(PO_4)_6$ appears

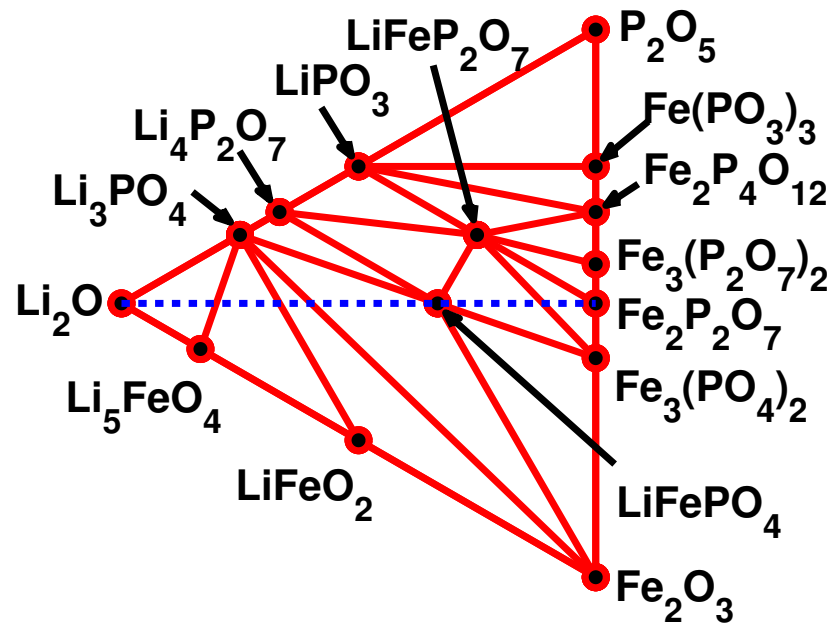


(b) $\mu_{O_2} = -11.52$ eV, $LiFePO_4$ appears

Figure 3-2: Li-Fe-P-O phase diagrams at less reducing environments.

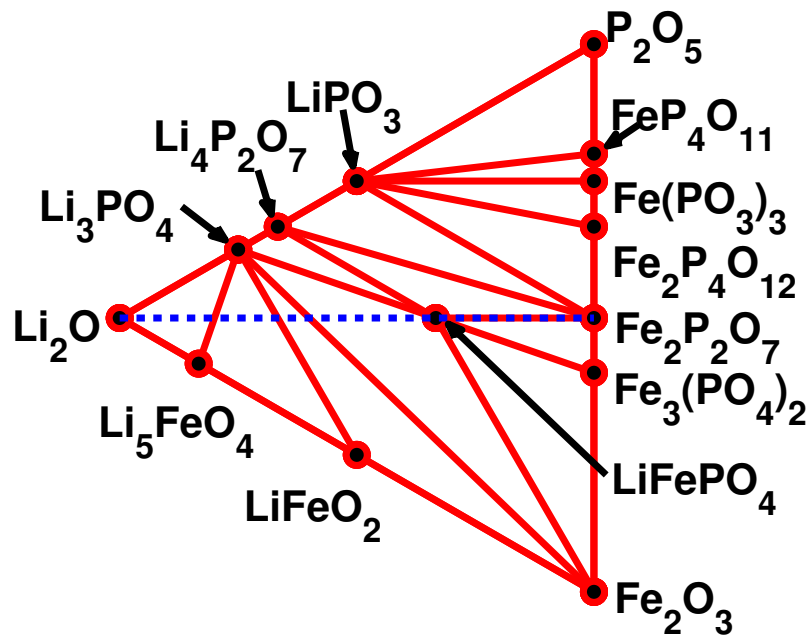


(a) $\mu_{O_2} = -11.74$ eV, $\text{Li}_3\text{Fe}_2(\text{PO}_4)_3$ disappears

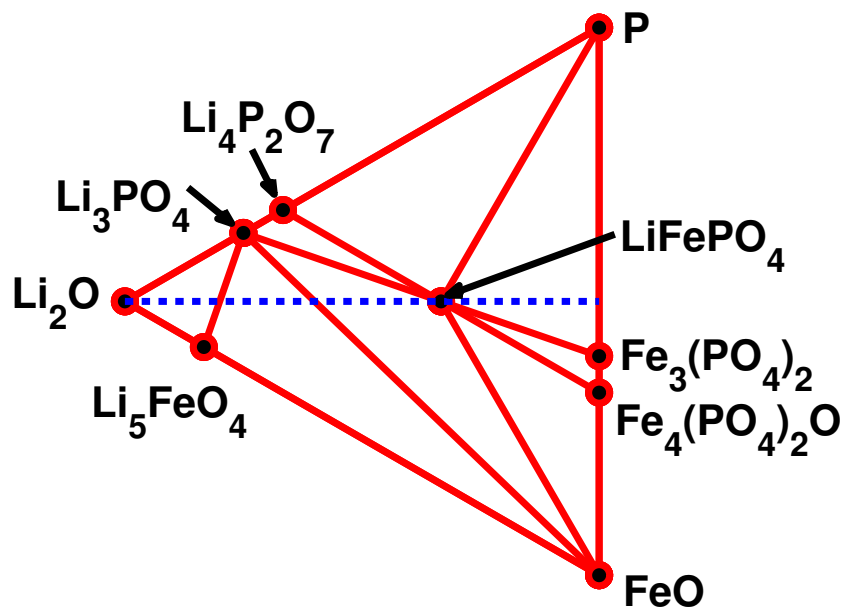


(b) $\mu_{O_2} = -12.38$ eV, $\text{Fe}_2\text{P}_2\text{O}_7$ appears

Figure 3-3: Li-Fe-P-O phase diagrams at more reducing environments.

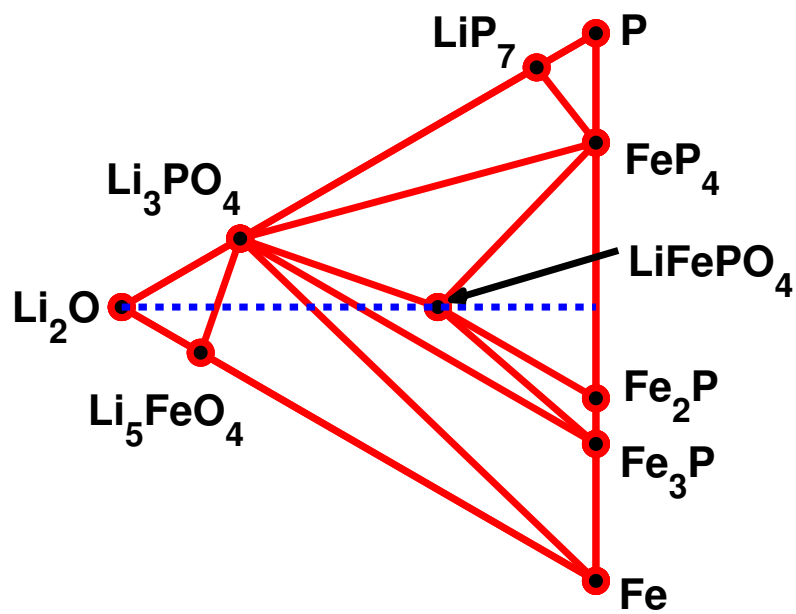


(a) $\mu_{O_2} = -13.08$ eV, LiFeP_2O_7 disappears

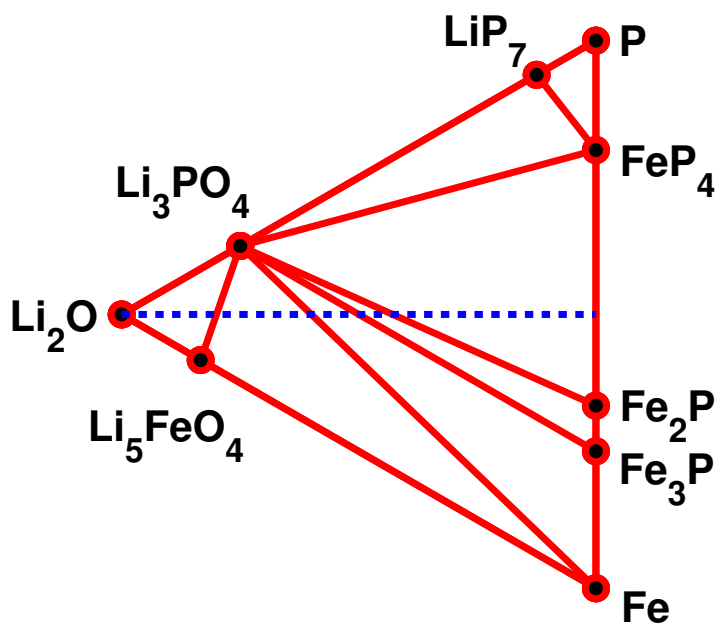


(b) $\mu_{O_2} = -16.08$ eV, $\text{Fe}_2\text{P}_2\text{O}_7$ disappears

Figure 3-4: Li-Fe-P-O phase diagrams at highly reducing environments.



(a) $\mu_{O_2} = -16.70$ eV, $Fe_3(PO_4)_2$ disappears



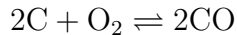
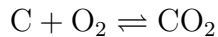
(b) $\mu_{O_2} = -16.74$ eV, $LiFePO_4$ disappears

Figure 3-5: Li-Fe-P-O phase diagrams at extremely reducing environments.

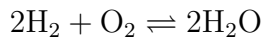
3.5 Modified Ellingham diagram

The effective oxygen partial pressure may be affected by the presence of reducing or oxidizing agents. For example, to improve electrical conductivity, carbon containing precursors are often used in the synthesis of LiFePO_4 . Carbon is a reducing agent and carbothermal reduction (CTR) is used extensively to reduce metal oxides to metals. The preparation of LiFePO_4 using CTR has been carried by various groups since it was first reported by Barker *et al.* in 2003.[11]

Carbon oxidation during CTR can take place via two different reactions:



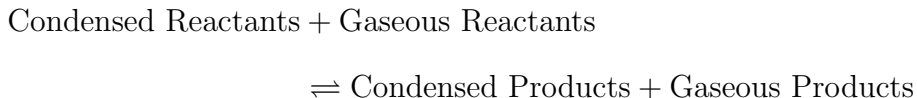
The CO_2 reaction, which is more thermodynamically favorable at lower temperatures, has minimal volume change and hence, negligible entropy change. At temperatures in excess of 1000 K however, the formation of CO becomes more thermodynamically favorable than the CO_2 reaction.[71] The CO reaction creates one extra mole of gas for every mole of oxygen consumed, and therefore involves an increase in entropy. As temperature increases, the free energy of formation of CO becomes increasingly negative, and this leads to stronger reducing conditions. In this work, we focused primarily on the CO reaction since LiFePO_4 synthesis is usually conducted at relatively high temperatures. Another reducing agent commonly used in LiFePO_4 synthesis is hydrogen gas, which is oxidized according to the following reaction:



For metal oxides, a typical method of showing the relationship between the reduction transition temperatures, oxygen partial pressures and the presence of reducing agents is an Ellingham diagram,[72] which shows the change in free energy of the oxidation reaction as a function of temperature. In this work, we have used a modified Ellingham construction where the change in Gibbs free energy for **reduction**

reactions of interest (normalized to a per O₂ molecule basis) in the Li-Fe-P-O system is plotted against temperature.

Consider the following general reaction:



where the gaseous products can be O₂, CO or H₂O depending on whether the reaction is a thermal reduction, carbothermal reduction or hydrogen reduction respectively, and the gaseous reactant comprises H₂ in the case of hydrogen reduction. As the entropy contributions of gases are much higher than that of condensed phases, the change in Gibbs free energy of the reaction can then be approximated as follows:

$$\Delta G = G_{\text{Products}} - G_{\text{Reactants}} \quad (3.1)$$

$$\approx H_{\text{Products}} - H_{\text{Reactants}} - T(S_{\text{Gaseous Products}} - S_{\text{Gaseous Reactants}}) \quad (3.2)$$

where the enthalpy, H , can be approximated with the internal energy, E , at 0K. To determine ΔG , we have used the energies for the various phases from our DFT calculations and experimental entropy values for the gases.

From the phase diagrams, we were able to extract the predicted phase relations for key reactions of interest. For instance, from the phase diagrams in Figures 3-2(b) and 3-3(a), we can see that a system with a Li:Fe:P composition of 3:2:3 will transit from a single phase, Li₃Fe₂(PO₄)₃, to a mixture of LiFePO₄, Li₃PO₄ and LiFeP₂O₇ as μ_{O_2} decreases, i.e., Li₃Fe₂(PO₄)₃ is being reduced to LiFePO₄, Li₃PO₄ and LiFeP₂O₇ with the release of O₂.

Based on the calculated phase diagrams, we have constructed the modified Ellingham diagram presented in Figure 3-6. The reactions chosen are those in which a phase of interest is being reduced or is being formed via a reduction reaction (e.g., formation and reduction of LiFePO₄). As these reduction reactions are not thermodynamically favored at 0 K, the changes in free energy of the reactions are positive

and decrease as temperature increases due to the entropy associated with the release of oxygen gas.

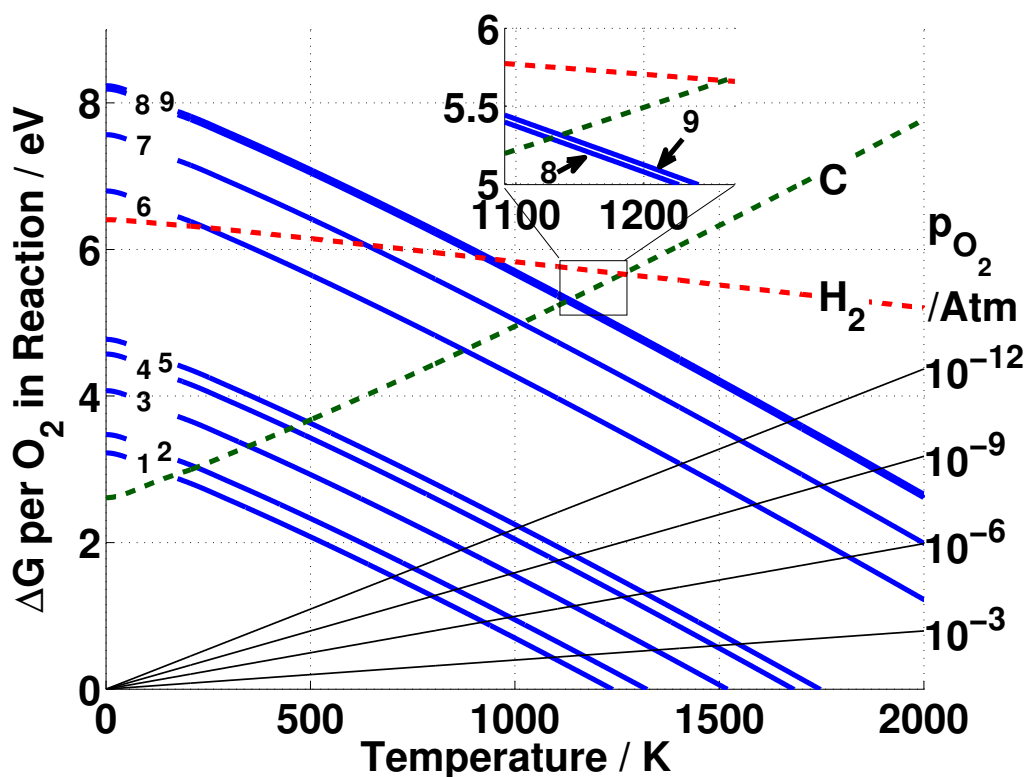
The estimated transition temperatures for thermal reduction at the reference oxygen partial pressure of 0.1 MPa are given by the intercept of the reaction lines (labeled 1-9 in Figure 3-6) with the temperature axis. At the transition temperature, the ΔG of a reaction changes from positive to negative and the reaction becomes thermodynamically favorable. The thermal reduction temperatures at lower oxygen partial pressures can be found where the $\Delta G(T)$ line intersects the relevant p_{O_2} line. Finally, the transition temperature for reduction by C/CO-CTR or hydrogen reduction at the reference partial pressure is given by the temperatures which the $\Delta G(T)$ line intersects the C or H₂ line.

The iron oxide reactions are included as a useful reference for comparison with the widely available Ellingham Diagram for the metal oxides. The predicted C/CO-CTR transition temperatures for $\text{FeO} \rightarrow \text{Fe}$, $\text{Fe}_3\text{O}_4 \rightarrow \text{FeO}$ and $\text{Fe}_2\text{O}_3 \rightarrow \text{Fe}_3\text{O}_4$ are approximately 1130 K, 880 K and 490 K respectively, which compares reasonably well to the experimental values of approximately 990 K, 930 K and 540 K.

3.6 Phase equilibria pertinent to LiFePO_4 synthesis

One of our key motivations for fully characterizing the Li-Fe-P-O phase diagram is to apply these diagrams to understand how different synthesis conditions create LiFePO_4 with very different electrochemical performance. From Figures 3-2 to 3-5, we observe that olivine LiFePO_4 is stable over a wide range of oxidation environments. LiFePO_4 is the first Fe^{2+} -containing phase to appear at $\mu_{O_2} = -11.52$ eV, and the last of the Fe-containing phosphates to be reduced at $\mu_{O_2} = -16.74$ eV. This large stability range provides a wide range of options for selecting the phases that can co-exist with LiFePO_4 .

In recent years, various research groups have experimented with synthesis ap-



Reaction	Line Label
$3 \text{Li}_3\text{Fe}_2(\text{PO}_4)_3 \rightleftharpoons 4 \text{LiFePO}_4 + 2 \text{LiFeP}_2\text{O}_7 + \text{Li}_3\text{PO}_4 + \text{O}_2$	1
$\frac{3}{2} \text{Fe}_7(\text{PO}_4)_6 \rightleftharpoons \text{Fe}_3(\text{P}_2\text{O}_7)_2 + \frac{5}{2} \text{Fe}_3(\text{PO}_4)_2 + \text{O}_2$	2
$2 \text{Fe}_3(\text{P}_2\text{O}_7)_2 \rightleftharpoons 2 \text{Fe}_2\text{P}_2\text{O}_7 + \text{Fe}_2\text{P}_4\text{O}_{12} + \text{O}_2$	3
$4 \text{LiFeP}_2\text{O}_7 \rightleftharpoons 4 \text{LiPO}_3 + 2 \text{Fe}_2\text{P}_2\text{O}_7 + \text{O}_2$	4
$6 \text{Fe}_2\text{O}_3 \rightleftharpoons 4 \text{Fe}_3\text{O}_4 + \text{O}_2$	5
$2 \text{Fe}_3\text{O}_4 \rightleftharpoons 6 \text{FeO} + \text{O}_2$	6
$\frac{6}{5} \text{Fe}_2\text{P}_2\text{O}_7 \rightleftharpoons \frac{4}{5} \text{Fe}_3(\text{PO}_4)_2 + \frac{4}{5} \text{P} + \text{O}_2$	7
$2 \text{FeO} \rightleftharpoons 2 \text{Fe} + \text{O}_2$	}
$\frac{1}{4} \text{Fe}_3(\text{PO}_4)_2 \rightleftharpoons \frac{1}{28} \text{FeP}_4 + \frac{5}{14} \text{Fe}_2\text{P} + \text{O}_2$	
$\frac{3}{4} \text{LiFePO}_4 \rightleftharpoons \frac{1}{4} \text{Li}_3\text{PO}_4 + \frac{5}{14} \text{Fe}_2\text{P} + \frac{1}{28} \text{FeP}_4 + \text{O}_2$	9
$2\text{CO} \rightleftharpoons 2\text{C} + \text{O}_2$	C
$2\text{H}_2\text{O} \rightleftharpoons 2\text{H}_2 + \text{O}_2$	H ₂

Figure 3-6: Modified Ellingham diagram for reduction reactions in Li-Fe-P-O system.

proaches for LiFePO_4 in which Li off-stoichiometry is introduced under a variety of reducing environments. The aim is to achieve phase equilibria in which conducting phases (e.g., iron phosphides) are formed together with LiFePO_4 , thereby compensating for the low electrical conductivity for LiFePO_4 . In three papers published between 2004 and 2007 (Herle *et al.*[20], Rho *et al.*[21], Ellis *et al.*[22]), Nazar and colleagues reported that the increase in conductivity in off-stoichiometric, aliovalently-doped LiFePO_4 is due to the formation of iron phosphides during LiFePO_4 synthesis. Systematic investigations were carried out on “Zr-doped” $\text{Li}_{1-x}\text{Zr}_{0.01}\text{FePO}_4$ (with the doping resulting in a Li-deficiency), stoichiometric LiFePO_4 and undoped Li-deficient LiFePO_4 processed at temperatures ranging from 600-850°C. They found that regardless of doping, Li-deficient $\text{Li}_{1-x}\text{FePO}_4$ ($0.01 < x < 0.07$) formed $\text{Fe}_2\text{P}_2\text{O}_7$ at 600°C, which disappeared at 800°C to form Fe_2P and iron phosphocarbide ($\text{Fe}_{75}\text{P}_{15}\text{C}_{10}$) at the grain boundaries. The fraction of $\text{Fe}_2\text{P}_2\text{O}_7$ was found to be correlated with degree of Li-deficiency. For stoichiometric LiFePO_4 , formation of phosphides was found at a higher temperature (850°C). Their investigations also found that formation of iron phosphides could be achieved at lower temperatures and shorter sintering periods using stronger reducing environments such as 7% H_2 - N_2 or NH_3 atmospheres.

Similar investigations were carried out by the Masquelier group (Delacourt *et al.*[30, 62]). They found that Li-rich compositions processed at temperatures $> 500^\circ\text{C}$ in a N_2 atm consist of LiFePO_4 , $\text{Li}_3\text{Fe}_2(\text{PO}_4)_3$ and iron oxides. For Li-deficient compositions, the mixed valence phosphate, $\text{Fe}_7(\text{PO}_4)_6$, was formed, and as the lithium content decreased, less $\text{Fe}_7(\text{PO}_4)_6$ formed but α - FePO_4 appeared. Significant amounts of Li_3PO_4 and iron oxides (Fe_2O_3 and Fe_3O_4) were also found as a result of partial decomposition of LiFePO_4 .

Kim *et al.*[73] also reported on the effects of synthesis conditions on the properties of LiFePO_4 . Their experiments found $\text{Fe}_2\text{P}_2\text{O}_7$ and Li_3PO_4 impurities for Li-deficient and Li-excess stoichiometries respectively, consistent with the findings of the Nazar and Masquelier groups.

Table 3.2 summarizes the predicted phase equilibria from our first principles Li-Fe-P-O₂ phase diagrams for three values of μ_{O_2} , which we believe to be representative

of the range of oxidation environments in experimental literature. *Lower μ_{O_2} phase equilibria correspond to more reducing experimental conditions of higher temperatures and/or lower oxygen partial pressures and/or the presence of reducing agents, and vice versa.* Comparing the predicted phase equilibria with the experimental findings, we find that:

1. Li-deficient stoichiometries: At less reducing conditions ($\mu_{O_2} = -10.50$ eV), the predicted phase equilibria for intermediate to severe Li-deficiency compositions is consistent with the formation of $Fe_7(PO_4)_6$ and $FePO_4$ observed by Delacourt *et al.*[62] $LiFePO_4$ itself is not present in the phase diagram at this μ_{O_2} level and begins to appear only at $\mu_{O_2} = -11.52$ eV (Figure 3-2(b)). However, inhomogeneities in the reaction environment may allow the co-existence of $LiFePO_4$ with $Fe_7(PO_4)_6$ and $FePO_4$ in actual experiments. At more reducing conditions, the predicted phase equilibria contains $Fe_2P_2O_7$ and under extremely reducing conditions, iron phosphides are formed. This prediction again compares well with the findings of the Nazar group. Their observation that the proportion of $Fe_2P_2O_7$ decreases with more Li-deficient stoichiometries can also be seen from the first principles phase diagrams by way of the lever rule. We note that for highly reducing environments, the first principles phase diagrams predict the formation of FeP_4 , which is seldom seen under experimental conditions. As mentioned previously, we attribute this to likely errors in the calculated energies of the metallic iron phosphides due to the application of the GGA+U methodology. Furthermore, phosphorus is treated as a condensed phase in our framework, though it is likely the actual experimental conditions are low P-chemical potential environments due to the vaporization of P.
2. Li-rich stoichiometries: For compositions with slight to intermediate Li-excess, the predicted phase equilibria comprises Li_3PO_4 and iron oxides in all but the most extreme reducing conditions. This observation is consistent with the findings of Kim *et al.*[73] The formation of $Li_3Fe_2(PO_4)_3$, $LiFePO_4$ and Fe_2O_3 for Li-rich compositions observed by Delacourt *et al.*[30] may be due to the partial

oxidation of LiFePO_4 (Figure 3-2(b)) or minor inhomogeneities in the reactants or reaction environment.

3. Stoichiometric LiFePO_4 : At sufficiently oxidizing environments, the predicted equilibrium phases are $\text{Li}_3\text{Fe}_2(\text{PO}_4)_3$ and Fe_2O_3 . This is consistent with the findings of Belharouak *et al.*[74]

$\mu_{\text{O}_2}/\text{eV}$	Li-deficient	Stoichiometric	Li-excess
-10.50	<u>Severe Deficiency</u> $\text{LiFeP}_2\text{O}_7 + \text{FePO}_4 + \text{Fe}_7(\text{PO}_4)_6$ <u>Intermediate Deficiency</u> $\text{LiFeP}_2\text{O}_7 + \text{Fe}_2\text{O}_3 + \text{Fe}_7(\text{PO}_4)_6$ <u>Slight Deficiency</u> $\text{Li}_3\text{Fe}_2(\text{PO}_4)_3 + \text{LiFeP}_2\text{O}_7 + \text{Fe}_2\text{O}_3$	$\text{Li}_3\text{Fe}_2(\text{PO}_4)_3 + \text{Fe}_2\text{O}_3$	<u>Slight-Intermediate Excess</u> $\text{Li}_3\text{Fe}_2(\text{PO}_4)_3 + \text{Fe}_2\text{O}_3 + \text{Li}_3\text{PO}_4$
-13.08	$\text{LiFePO}_4 + \text{Fe}_2\text{P}_2\text{O}_7$	LiFePO_4	<u>Slight-Intermediate Excess</u> $\text{LiFePO}_4 + \text{Li}_3\text{PO}_4 + \text{Fe}_2\text{O}_3$
-16.70	$\text{LiFePO}_4 + \text{FeP}_4 + \text{Fe}_2\text{P}$	LiFePO_4	<u>Slight Excess</u> $\text{LiFePO}_4 + \text{Li}_3\text{PO}_4 + \text{Fe}_3\text{P}$ <u>Intermediate Excess</u> $\text{Li}_3\text{PO}_4 + \text{Fe}_3\text{P} + \text{Fe}$

Table 3.2: Predicted phase equilibria under various oxidation and Li off-stoichiometry conditions.

From Figure 3-6, we can obtain the predicted temperatures necessary to achieve reduction of LiFePO_4 and $\text{Fe}_2\text{P}_2\text{O}_7$ to the iron phosphides. In the absence of reducing agents, the formation of iron phosphides from reduction of LiFePO_4 is predicted to occur at > 1500 K. In the presence of carbon, however, the predicted transition temperature decreases to around 1100 K (assuming CO is produced at the reference partial pressure). In a H_2 atmosphere, the predicted transition temperature is even lower at around 900 K (again assuming H_2 and H_2O are at the reference partial

pressure). For formation of the iron phosphides from $\text{Fe}_2\text{P}_2\text{O}_7$, the phase diagrams indicate that this happens through a two-stage reduction where $\text{Fe}_2\text{P}_2\text{O}_7$ decomposes first to $\text{Fe}_3(\text{PO}_4)_2$, which is in turn reduced to the iron phosphides. The latter process is predicted to take place at slightly lower temperatures than that for reduction of LiFePO_4 .

Comparing with the experimental literature, the following observations can be made:

1. The predicted temperatures for C/CO-CTR of LiFePO_4 compare well with those in experimental literature, which are generally in the range of 800-900°C (1073-1173 K).
2. Herle *et al.*[20] has observed that LiFePO_4 samples synthesized from non-carbon containing precursors do not become electrically conducive at any of the temperatures investigated. This observation is consistent with the high thermal reduction temperatures predicted for stoichiometric LiFePO_4 in the absence of reducing agents.
3. Ellis *et al.*[22] has reported that CTR of $\text{Fe}_2\text{P}_2\text{O}_7$ to iron phosphides takes place at around 800°C, compared with 850°C for LiFePO_4 . Reduction in a 7% H_2 - N_2 atmosphere was found to take place at an even lower temperature and shorter sintering times. These observations are again consistent with the predictions from our modified Ellingham diagram.

Overall, we found that the predicted phase equilibria and transition temperatures from our first principles phase diagram and modified Ellingham diagram agree remarkably well with the findings in the experimental literature surveyed. While there are some differences in some of the phases and temperatures predicted, these errors do not seem to affect in a significant way the phase evolution as function of composition or reduction conditions.

3.7 Applications

Having validated the diagrams with experimental literature, they can be used to evaluate current approaches to synthesizing LiFePO_4 and in the development of new synthesis routes to achieve desired properties.

Yamada *et al.*[14] identified two key challenges to achieving optimal performance for LiFePO_4 : i) undesirable particle growth at $T > 600^\circ\text{C}$ and ii) the presence of residual non-crystalline Fe^{3+} phase at $T < 500^\circ\text{C}$. Based on our literature survey, current approaches to addressing these obstacles seem to primarily focus on tuning the oxidation environment and Li off-stoichiometry. Indeed, our phase diagrams show that the nature and degree of Li off-stoichiometry is an important factor in influencing the eventual phase equilibria obtained. For instance, an excess of lithium is often introduced during LiFePO_4 synthesis to compensate for lithium volatility at high temperature firing conditions. As can be seen from Figures 3-2 to 3-4, a Li-excess stoichiometry is likely to result in the formation of undesirable iron oxides at low temperatures, while higher temperatures may lead to excessive particle growth. The phase diagrams provide a means to identify possible phase equilibria which may offer better performance. Applying the lever rule on the phase diagrams also provides a means to determine the stoichiometric proportions needed to achieve a desired balance of LiFePO_4 and impurity phases, and the modified Ellingham diagram provides a method for fine-tuning the chemical and physical environments to achieve the desired degree of reduction of LiFePO_4 and impurity phases.

Indeed, other off-stoichiometries to achieve “useful” impurity phases are the subject of a recent paper by Kang *et al.*[75] Using our computed phase diagrams, Kang *et al.* synthesized $\text{LiFe}_{0.9}\text{P}_{0.95}\text{O}_{4-\delta}$, an off-stoichiometry designed to achieve the formation of glassy lithium phosphates that are well known to be good, stable Li^+ conductors (see Figure 3-4(b), along the $\text{Li}_4\text{P}_2\text{O}_7$ - LiFePO_4 composition line). The result is an extremely high-rate LiFePO_4 material where capacities in excess of 100C were achieved, and Li^+ diffusion in and out of the active material is aided by the highly ionically conductive surface coating. Kang *et al.* also used a similar approach

to improve the electrochemical performance of LiMnPO_4 based on the Li-Mn-P-O phase diagram calculated from first principles in this thesis (see Chapter 4), albeit with less success than LiFePO_4 .^[76]

While our main motivation for this work is to apply the phase diagrams to LiFePO_4 synthesis, this is by no means the only phase of interest in the Li-Fe-P-O system. For example, iron phosphates, in particular FePO_4 , has been used as a catalyst for oxidative dehydrogenation reactions for many years,^[77] while Li_3PO_4 is used as a solid electrolyte in film batteries. The phase diagrams developed can be provide a better understanding of redox phase relations for these phases.

3.8 Conclusion

We have characterized the phase diagram of the Li-Fe-P-O system as a function of oxidation conditions using first principles techniques. As we only consider the entropy of gaseous phases, temperature and oxygen partial pressure can be put on the same scale. By incorporating experimental thermodynamic data, we were also able to construct a modified Ellingham diagram to provide a visual representation of the relation between the temperatures, oxygen partial pressures and chemical environment necessary to achieve a desired reduction reaction. The predicted phase equilibria and reduction temperatures compare well to experimental findings on stoichiometric and off-stoichiometric LiFePO_4 reactions. The combined application of the phase diagrams and Ellingham diagram provides a means to more efficiently focus experimental efforts to optimize synthesis approaches for LiFePO_4 , and has indeed been applied to the development of a high-rate LiFePO_4 with highly conductive glassy impurity phases.

Chapter 4

Estimating the thermal stability of intercalation electrodes

4.1 Thermal stability in olivine cathodes

In recent years, there has been increasing interest in LiMnPO_4 , LiCoPO_4 and LiNiPO_4 which could potentially deliver higher theoretical energy densities than LiFePO_4 due to their higher measured/predicted voltages of 4.1 V, 4.8 V and 5.1 V vs Li/Li^+ respectively.[23, 24, 18] Of these promising alternatives, LiMnPO_4 has garnered the most interest because its voltage of 4.1 V is higher than LiFePO_4 (3.5 V) but well within the limitations of current organic electrolytes. While focus has been on understanding LiMnPO_4 's poor rate performance due to low ionic and electronic conductivities,[25] a high surface energy barrier for Li diffusion,[26] or significant volume change at the phase boundary,[13, 16, 27] it has been tacitly assumed that the charged compound, MnPO_4 , would match the excellent thermal stability of FePO_4 . Two recent investigations by Kim *et al.*[28] and Chen *et al.*[29] have cast doubt on that assumption by demonstrating that while fully lithiated LiMnPO_4 remains stable up to fairly high temperatures, delithiated MnPO_4 decomposes at temperatures of around 150-200°C, evolving O_2 and heat in the process. This is in stark contrast to delithiated FePO_4 which has been shown to be stable for temperatures up to 500-600°C.[30] There is also experimental evidence that the other higher voltage olivines, LiCoPO_4

and LiNiPO_4 , are similarly thermally unstable upon delithiation. Using synchrotron diffraction and differential thermal analysis, Bramnik *et al.*[31] found that delithiated Li_xCoPO_4 ($x = 0.6, 0$) decomposes readily around 100-200°C. Preliminary work by Wang *et al.*[32] also found LiNiPO_4 to be unstable upon delithiation, and $\text{Ni}_2\text{P}_2\text{O}_7$ is formed.

In this thesis, we constructed the oxygen grand potential phase diagrams for the Li-M-P-O ($M = \text{Fe}, \text{Mn}, \text{Ni}, \text{Co}$) systems using the methodology in Chapter 2.[1] We were able to confirm the lower stability of delithiated MnPO_4 , CoPO_4 and NiPO_4 , and demonstrate that the difference in the relative stabilities of the delithiated MPO_4 phases can be explained in terms of the competing phases present in the phase diagrams.[2]

4.2 Computational details

In this portion of the thesis, we utilized the high-throughput computational infrastructure developed as part of the Materials Genome project at the Massachusetts Institute of Technology. While the essential thermodynamic methodology for phase diagram construction is the same as that outlined in Chapter 2, there were slight differences in the computational parameters due to efficiency and other considerations inherent in a high-throughput project.

We calculated the energies of all structural prototypes in the Li-M-P-O systems in the 2006 version of the Inorganic Crystal Structure Database.[52] Compounds having partial occupancies were related to the ordered structure with lowest electrostatic energy[78, 79] at the same or close composition from a group of representative structures enumerated with a technique similar to that proposed by Hart *et al.*[80]

U values of 3.9 eV, 4.0 eV and 6.0 eV were used for Mn, Fe, and Ni respectively, following Wang *et al.*'s method[59] of fitting the calculated binary oxide formation enthalpies to experimental values from the Kubaschewski tables.[60] For Co, a U value of 5.7 eV was used based on the average of the values determined by Zhou *et al.*[23] for the olivine system. The reason why a different scheme was used for Co is because

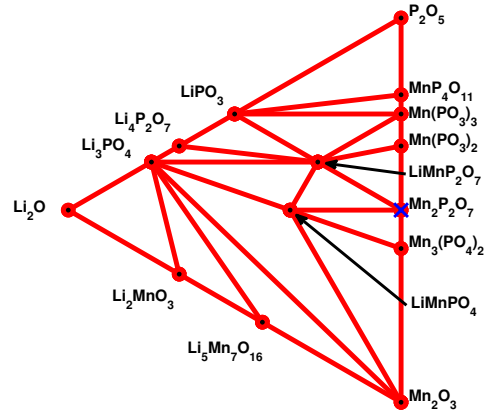
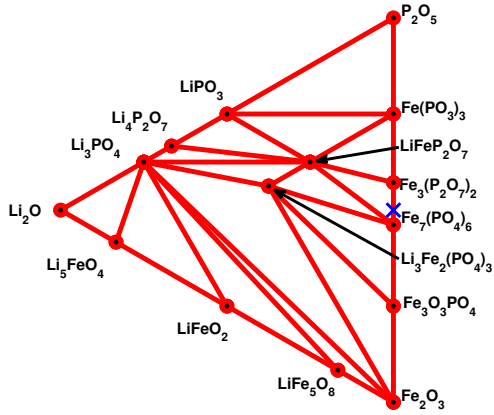
the U value of 3.4 eV determined using Wang *et al.*'s method led to a significant underestimation of the voltages, while Zhou *et al.*'s value led to much better agreement with experiments. A plane wave energy cut-off of 520eV and k -point density of at least 500/(number of atoms in unit cell) were used for all computations. All calculations were spin-polarized starting from a high-spin ferromagnetic configuration for Fe, Mn, Co and Ni.

4.3 Phase diagrams at critical μ_{O_2} for reduction

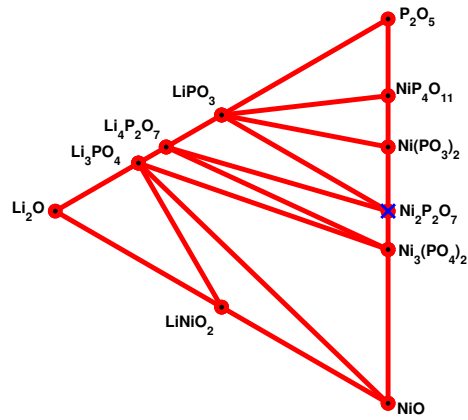
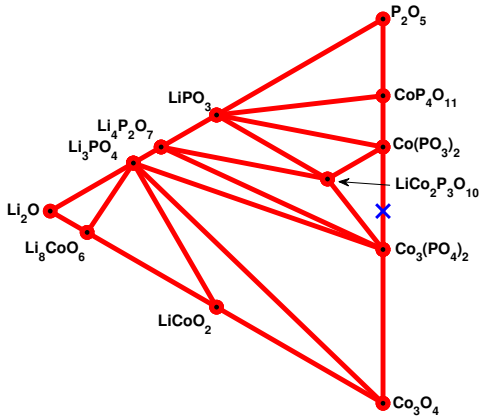
To investigate the stability of delithiated MPO_4 , we have constructed the phase diagrams at various μ_{O_2} . Increased temperature and lowering oxygen partial pressures leads to a more reducing condition, i.e., more negative μ_{O_2} . In this work, we have set the reference oxygen chemical potential to be zero at the room temperature air (298K, 0.21atm) value obtained with the calculated value of E_{O_2} in equation 2.5. This calculated value has been corrected for the O_2 binding energy error and GGA error associated with adding electrons to the oxygen p orbital when O^{2-} is formed through a constant -1.36eV shift.[59] Experimental entropy data for O_2 at 0.1MPa were obtained from the JANAF thermochemical tables.[71]

The critical temperature for reduction of the MPO_4 corresponds to an μ_{O_2} below which the compound decomposes. The equilibrium reduction products are given by the phases stable below this critical μ_{O_2} . Figure 4-1 show the oxygen grand potential phase diagrams for the Li-M-P-O systems at μ_{O_2} just below that required for the reduction of the delithiated olivine MPO_4 phase. It should be noted that the delithiated olivine is not the ground state structure for the $FePO_4$ composition, and the trigonal ground state phase and all phases lower in energy than the olivine phase[81] have been removed from the dataset to determine the non-equilibrium reduction pathway. We will discuss the consequence of this removal in the next section.

Reduction of $FePO_4$ takes place at a much lower μ_{O_2} of -1.72 eV ($\approx 700^\circ C$ under air) compared to $MnPO_4$, which reduces at μ_{O_2} of -0.83 eV ($\approx 370^\circ C$). Our calculations predict $CoPO_4$ and $NiPO_4$ to be even less stable than $MnPO_4$ and reduce even



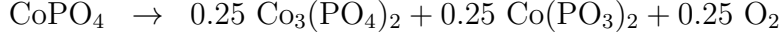
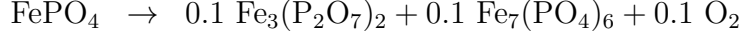
(a) Li-Fe-P-O phase diagram at $\mu_{O_2} = -1.72$ eV ($T \approx 700^\circ\text{C}$) (b) Li-Mn-P-O phase diagram at $\mu_{O_2} = -1.72$ eV ($T \approx 700^\circ\text{C}$).



(c) Li-Co-P-O phase diagram at $\mu_{O_2} = 0$ eV ($T \approx 25^\circ\text{C}$) (d) Li-Ni-P-O phase diagram at $\mu_{O_2} = 0$ eV ($T \approx 25^\circ\text{C}$).

Figure 4-1: Li-M-P-O ($M = \text{Fe, Mn, Co, Ni}$) phase diagrams for μ_{O_2} just below critical values where delithiated MPO_4 olivine decomposes. The composition of MPO_4 is marked with an X.

at μ_{O_2} of 0 eV ($\approx 25^\circ C$). From the phase triangle bounding the MPO_4 compositions, we can see that the delithiated MPO_4 undergo the following initial reduction reactions:



The predicted reduction temperatures and products are in fairly good agreement with experimental findings. Delacourt *et al.*[30] have previously reported the formation of the mixed valence $Fe_7(PO_4)_6$ phase for Li_xFePO_4 ($x \ll 1$) at 500-600°C. Kim *et al.*[28] and Chen *et al.*[29] also reported that the decomposition of $MnPO_4$ leads to the formation of $Mn_2P_2O_7$ at 150-200°C. Bramnik *et al.*[31] has found that delithiated Li_xCoPO_4 ($x = 0.6, 0$) are unstable upon heating, and decompose readily in the range 100-200°C. $Co_2P_2O_7$ was found as the decomposition product, which differs from the prediction of our phase diagram. However, $Co_2P_2O_7$ is only less than 1 meV above the convex hull formed by $Co_3(PO_4)_2$ and $Co(PO_3)_2$, which is well within the error tolerance we expect from our DFT calculations. Preliminary work by Wang *et al.*[32] found $LiNiPO_4$ to be unstable upon delithiation and immediately decomposes to $Ni_2P_2O_7$ with the evolution of oxygen gas.

The calculated temperatures may differ from experimentally measured temperatures for several reasons. Firstly, a 100K temperature difference corresponds to about 10 meV, well within the errors of our DFT calculations and entropy approximations. Secondly, the presence of reducing agents such as the electrolyte and carbon under experimental conditions will tend to decrease the actual decomposition temperatures. We also observe that in $MnPO_4$ decomposition, the Mn/P ratio stays constant and only O_2 release takes place, while for $FePO_4$, longer range transport will be needed to create phases with Fe/P ratio different from 1.

4.4 O₂ evolved versus temperature

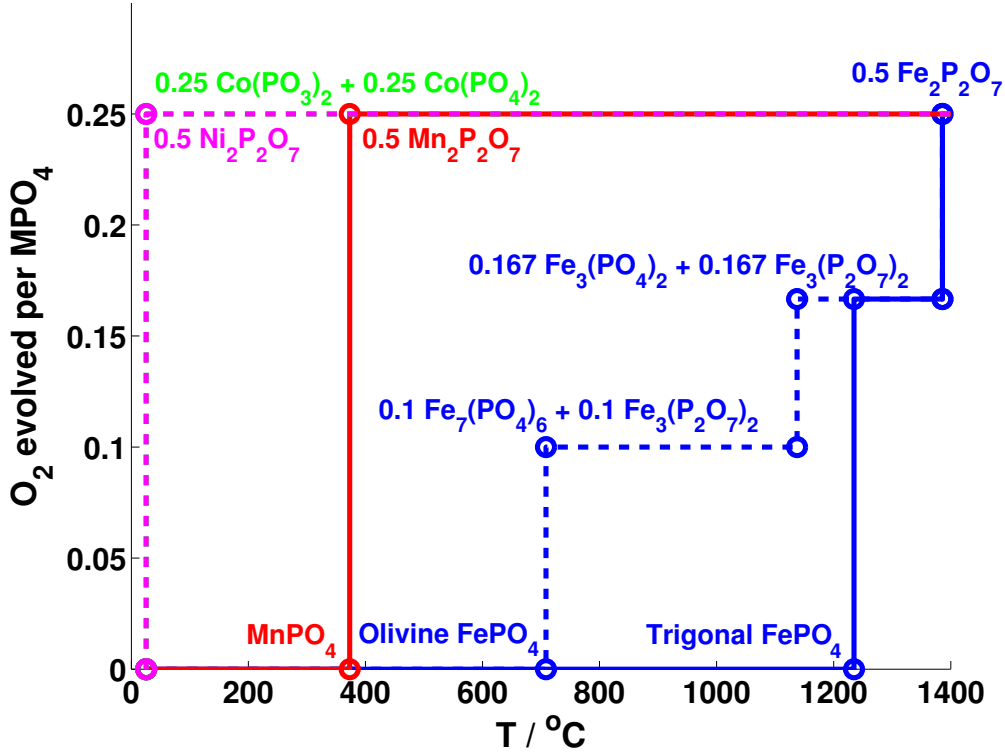


Figure 4-2: O₂ evolved vs temperature for delithiated MPO₄ (M=Fe, Mn, Co, Ni).

Figure 4-2 summarizes the O₂ evolution versus temperature for the reduction paths of FePO₄, MnPO₄, CoPO₄ and NiPO₄. Both the non-equilibrium paths and the equilibrium paths are shown for FePO₄. The non-equilibrium path corresponds to the likely reaction path if the FePO₄ olivine is unable to transform to the lowest energy trigonal structure[82, 83] (space group $P3_121$) due to kinetic limitations, and proceeds to reduce into other phases with the evolution of oxygen. The equilibrium path assumes that olivine FePO₄ is able to transform first into the trigonal phase before undergoing reduction.

For FePO₄, O₂ evolution takes places at a much lower temperature for the non-equilibrium path as compared to the equilibrium path. The path taken depends on the relative kinetics, which is affected by experimental conditions and Li content. Stability investigations by Yang *et al.* and Rousse *et al.*[82, 83] have shown

that orthorhombic FePO_4 transforms irreversibly to trigonal FePO_4 only at fairly high-temperatures of 600-700°C, though there is some controversy as to the transition temperature for this structural transformation.[81] Regardless, the fact that the mixed valence $\text{Fe}_7(\text{PO}_4)_6$ was observed by Delacourt *et al.*[30] during Li_xFePO_4 ($x \ll 1$) decomposition at 500-600°C suggests that some degree of non-equilibrium decomposition does take place under certain experimental conditions. For MnPO_4 , the olivine phase is the lowest energy structure. Nonetheless, the critical temperature for the onset of O_2 evolution in non-equilibrium FePO_4 reduction is still much higher than that for MnPO_4 . Both CoPO_4 and NiPO_4 are predicted to be unstable and undergo immediate decomposition.

From Figure 4-2, we may also observe that initial reduction of FePO_4 evolves 0.1 moles of oxygen per mole of cathode, compared to 0.25 moles for initial reduction of MnPO_4 , CoPO_4 and NiPO_4 . Hence, not only does MnPO_4 , CoPO_4 and NiPO_4 reduce at a much lower temperature than FePO_4 , they also evolve 2.5 times the amount of O_2 . Even at higher temperatures between 1100°C and 1300°C, FePO_4 only evolves 0.17 moles of oxygen per mole of cathode, significantly less than MnPO_4 , CoPO_4 and NiPO_4 . This greater amount of O_2 evolved presents a significant safety hazard as O_2 released can ignite the organic electrolytes used in rechargeable Li batteries.

4.5 Implications for cathode design

Our results show that delithiated FePO_4 is inherently more thermally stable than MnPO_4 , CoPO_4 and NiPO_4 , and the amount of O_2 evolved upon initial decomposition is also much less. Specifically, the greater stability of FePO_4 over MnPO_4 may be explained through ligand field theory.[84] It is well-known that in an octahedral environment such as MO_6 in olivines, half-filled high-spin $t_{2g}^3 e_g^2$ is a highly stable electronic configuration due to the exchange stabilization arising from the five parallel-spin electrons. We would therefore expect that Fe^{3+} and Mn^{2+} , both of which have the half-filled high-spin $t_{2g}^3 e_g^2$ configuration, to have greater stability as compared to Fe^{2+} and Mn^{3+} respectively. Indeed, there is a greater proportion of Mn^{2+} phases relative to

Mn³⁺ in the Li-Mn-P-O phase diagram, whereas the situation is reversed in the case of Fe. Furthermore, LiMnPO₄ is stable over a much wider range of oxygen chemical potentials ($-0.56eV < \mu_{O_2} < -7.02eV$) than LiFePO₄ ($-2.36eV < \mu_{O_2} < -6.24eV$). A similar argument has been used to explain why the LiFePO₄ voltage is unusually low.[23]

The key factor influencing the amount of O₂ evolved is the competing phases present in the system, which is also related to the relative stabilities of the +2 and +3 oxidation states. In the Fe system, the relative stability of the Fe³⁺ oxidation state leads to the presence of the mixed valence Fe₇(PO₄)₆ and Fe₃(P₂O₇)₂ phases, which results in a smaller amount of O₂ evolved. On the other hand, MnPO₄ immediately reduces to Mn₂P₂O₇, which has the Mn²⁺ oxidation state, resulting in significantly higher O₂ evolution. Similarly, the dearth of mixed valence Co and Ni phases also explains the relatively high O₂ evolution in these systems.

Huggins[85] has previously performed a thermodynamic analysis of the relationship between equilibrium Li voltages and oxygen partial pressure for a number of ternary oxide systems. He found that extrapolation of the observed trends indicates high values of equilibrium O₂ partial pressures in high voltage materials. Our results similarly suggest that there could be some tradeoff between higher voltage and thermal stability of the charged cathode. However, the voltage of a rechargeable Li battery cathode material is related to the difference in energies between the delithiated and lithiated phases.[23] Therefore, a **higher voltage can come from either a more stable lithiated phase, or a less stable delithiated phase**. So this tradeoff between higher voltage and thermal stability of the charged cathode may not be absolute. We also note that coating strategies have been successfully employed to stabilize the charged cathode in LiCoO₂ batteries,[86, 87] and similar strategies could possibly be developed for the olivine cathodes to mitigate safety concerns.

4.6 Thermal stability as a design criteria in a high-throughput materials search

The technique developed in this work can be adapted to be a design criteria for a high-throughput search. The chemical potential range for which a delithiated cathode is stable can be obtained easily from the oxygen chemical potentials of the facets bounding that phase in the relevant composition phase diagram. Then, by constructing the oxygen grand potential phase diagram for that system just outside of those limits, we can obtain the decomposition phases and the amount of O_2 evolved. **The critical μ_{O_2} for reduction to take place and the amount of O_2 evolved can therefore serve as thermal stability design criteria for a high-throughput materials search, be it for intercalation electrodes or other materials.**

However, we would like to point out an inherent limitation of the approach. These design criteria are based on a thermodynamic analysis and does not take into account kinetic limitations. While a material may be thermodynamically unstable under certain conditions, it could be kinetically stable (e.g., diamond carbon under standard conditions). As such, these design criteria should be used only as a broad initial screening tool. For the case of $FePO_4$ in our work, we did approximate kinetic effects by considering the non-equilibrium pathway for decomposition, but this analysis is not amenable to scaling to high-throughput analysis.

4.7 Conclusion

In this work, we analyzed the thermal stabilities of delithiated MPO_4 ($M = Fe, Mn, Co, Ni$) by constructing the oxygen grand potential phase diagrams of the Li-M-P-O systems using first-principles calculations. Our observations indicate, in agreement with recent experiment findings,[28, 29] that $MnPO_4$ reduces with substantial oxygen release at a much lower temperature than $FePO_4$. Hence, the Mn system may trade off its somewhat higher energy density with considerably lower safety. The difference in relative stabilities of $FePO_4$ and $MnPO_4$ may be explained by the competing phases

present in the phase diagrams and relative stabilities of the M^{2+} and M^{3+} as explained by ligand field theory. Similarly, delithiated CoPO_4 and NiPO_4 are predicted to be extremely unstable, in agreement with the experimental findings of Bramnik *et al.*[31] and the preliminary findings of Wang *et al.*[32]

Chapter 5

Beyond DFT: Hybrid functional calculations of redox energies

5.1 Redox energies in DFT

Reduction and oxidation (redox) reactions are relevant in many technological applications and environmental processes, from electrochemical generation and storage systems such as fuel cells and rechargeable Li-ion batteries to corrosion processes. Owing to their importance, the development of first-principles techniques to study redox reactions has therefore been an area of considerable research interest.[88, 89, 90, 59, 91]

In redox reactions, electrons are transferred from one species to another. Previous work[90, 59] has shown that the standard local density (LDA) and generalized gradient approximation (GGA) to density functional theory (DFT) lead to considerable errors in calculated redox energies. These errors can be attributed in part to the lack of self-interaction error cancellation when the redox electron is transferred between significantly different environments, such as between metallic Li and an ionic transition metal (TM) environment in the case of Li intercalation compounds. Zhou *et al.*[90] demonstrated that treating the self-interaction error by means of the DFT+ U method,[43, 42, 44, 57] where the U parameter is determined by a linear response scheme, leads to predicted Li intercalation potentials for TM compounds that are in much better agreement with experiments. Wang *et al.*[26] found that the DFT+ U

method can similarly be applied to correct for self-interaction errors in the calculated reaction energies of TM oxides.

In this thesis, we revisited the calculation of Li intercalation potentials and formation energies of TM compounds, in the context of hybrid density functionals.[5] The hybrid density functional modification of the DFT scheme has predominantly been used in molecular chemistry applications,[92] but has more recently gained momentum in the solid state community, possibly due to the introduction of hybrids functionals that are not specifically tailored for molecular chemistry applications.[93, 3, 94, 4]

5.2 Hybrid functionals

The exact Hartree-Fock (HF) exchange energy cancels the self-interaction error in the electron energy by construction.[45] It follows that the hybrid scheme of using a fraction of the HF exchange energy plus a fraction of a conventional semi-local functional cancels more of this error than using only the latter. Hybrid functionals, such as B3LYP, have also been found successful for calculations on simple TM oxides.[95, 96, 97] The improvement of the self-interaction error is expected to reduce the unwanted electron self-repulsion and thus, at least partially, avoid the well-known problem of over-delocalized electrons in LDA or GGA. Zhou *et al.*[90] argued that it was precisely such over-delocalization of *d*-orbital electrons on the TM ions that was responsible for the poor performance of conventional functionals for redox reactions, which prompted their use of DFT+*U*. This argument thus motivates us to investigate the performance of hybrid functionals in the same type of applications. Furthermore, hybrid functionals provide a more general treatment of the self-interaction error over all species, as opposed to the treatment of specific orbitals of specific species in typical DFT+*U* implementations. While the HSE06 functional[3, 94, 4] used in this thesis do have a number of adjustable parameters, such as the screening parameter and the fraction of exact exchange (see the next few paragraphs), none of these parameters are typically determined on a chemistry-specific basis, i.e., a common set of parameters is used for all chemistries. This is unlike the case for DFT+*U* where a oxidation

state and local environment-dependent U value has to be determined for each individual species.[90] Hence, hybrid functionals could provide for a more straightforward, though more expensive, prediction of redox energies.

The HSE06 functional starts from the PBE0 functional,[93] which is an implementation of the Becke three-parameter hybrid formula[92, 98] that combines PBE exchange E_x^{PBE} and correlation E_c^{PBE} with HF exchange E_x^{HF} ,

$$E_{xc}^{\text{PBE0}} = \frac{1}{4}E_x^{\text{HF}} + \frac{3}{4}E_x^{\text{PBE}} + E_c^{\text{PBE}} \quad (5.1)$$

In HSE06, the exchange terms are divided into short-range (SR) and long-range (LR) parts, and to avoid the expensive calculation of long-range HF exchange, this term is replaced by long-range PBE exchange,

$$E_{xc}^{\text{HSE}} = \frac{1}{4}E_x^{\text{HF,SR}}(\mu) + \frac{3}{4}E_x^{\text{PBE,SR}}(\mu) + E^{\text{PBE,LR}}(\mu) + E_c^{\text{PBE}} \quad (5.2)$$

where the screening parameter $\mu = 0.207 \text{ \AA}^{-1}$ was determined as a compromise between speed and accuracy from a test set of molecules and solids.[3] The screening approach of HSE06 produces a hybrid functional that has a similar accuracy to PBE0, but is less computationally demanding.

5.3 Methods

5.3.1 Intercalation potentials of electrode materials

The average intercalation potential, $\langle V \rangle$, when lithiating a material Li_xX from $x = x_1$ to x_2 vs. Li/Li^+ can be calculated using the following expression[99]:

$$\langle V \rangle = \frac{-[E(\text{Li}_{x_2}\text{X}) - E(\text{Li}_{x_1}\text{X}) - (x_2 - x_1)E(\text{Li})]}{(x_2 - x_1)e}, \quad (5.3)$$

where E is the total energy as calculated using DFT, and e the absolute value of the electron charge. To calculate average Li intercalation potentials, we considered

complete, topotactic delithiation. Experimental lithiated structures were taken from the Inorganic Crystal Structure Database (ICSD),[52] and delithiated structures were obtained by removing all Li atoms from the lithiated structures.

The intercalation materials studied were chosen to represent the major classes of intercalation materials currently used or under consideration as positive electrode materials in Li-ion batteries.

1. The traditional positive electrode materials are the LiMO_2 layered oxides ($M=\text{Co}, \text{Ni}$), which are favored for their high intercalation potentials and energy densities. The LiMO_2 layered oxides are O3-type structures, where the oxygen planes have an ABCABC stacking sequence.[100] In these structures, Li intercalates between layers of TM-centered oxygen octahedra. After complete delithiation, the MO_2 layers are weakly bound by van der Waals forces.[101] The layered oxides have been extensively studied both experimentally[102, 103] and theoretically.[99, 104, 105, 106]
2. Two Ti-containing materials were chosen to study materials having weakly localized $3d$ electrons. Li_xTiS_2 and $\text{Li}_x\text{Ti}_2\text{O}_4$ both display metallic conductivities;[107, 108] consequently, the delocalized Ti d states should not require the use of a U correction. The layered dichalcogenide, LiTiS_2 was once considered as a positive electrode material, but its Li intercalation potential of 2.0 V was deemed too low to achieve reasonable energy densities.[107] Li_xTiS_2 is an O1-type layered structure, where the sulfur planes have an ABAB stacking sequence. Spinel LiTi_2O_4 also has a low Li intercalation potential (1.3 V) but can be used as a negative electrode in applications requiring excellent safety and power capability.[108] It is the only electrode material considered that does not undergo complete topotactic delithiation. In its lithiated state, $\text{Li}_2\text{Ti}_2\text{O}_4$, the Li atoms reside on the octahedral $16c$ sites of the $Fd3m$ (227) space-group, whereas in its delithiated state, LiTi_2O_4 , the Li atoms reside on the tetrahedral $8a$ sites of the same space group.[109]
3. The spinel-like LiMn_2O_4 is popular for its high voltage (4.1 V) and reasonable

cost.[102, 110] It is isostructural with the spinel mineral MgAl_2O_4 and presents a three-dimensional network of face-sharing oxygen tetrahedra and octahedra. The Mn atoms reside in MnO_6 octahedra. In the lithiated structure, the Mn ions are evenly distributed in nominal Mn^{3+} and Mn^{4+} states.[111]

4. The olivine structures, LiMPO_4 (M=Mn, Fe, Co, Ni) studied in the preceding chapters were also studied in this work.[14, 24, 18, 112] The olivine structures comprise vertex-sharing MO_6 octahedra, and PO_4 tetrahedra that share one edge and all vertices with MO_6 octahedra. The olivines are differentiated from the previously mentioned oxides, which will be referred to as “simple” oxides, by the presence of PO_4 polyanions. It is believed that the TM ions hybridize less with the PO_4 groups than with oxygen atoms of simple oxides.[9] The lack of hybridization should lead to a greater degree of localization of the $3d$ electrons on the TM ions, and thereby increase the self-interaction error of LDA/GGA.

5.3.2 Oxide Formation Energies

Formation energies were calculated for 26 oxides for which experimental formation enthalpies are available.[71, 60] The choice of oxides follows closely that of Wang *et al.*[59] The chosen oxides can be separated into two categories. The first category is comprised of oxides containing main group elements (Li, Na, Mg, Al, Ca) and elements with weakly localized $3d$ electrons (Ti), while the second category consists of TMs with strongly localized $3d$ electrons (V, Cr, Mn, Fe, Co, Ni, Cu). Following the methodology of Wang *et al.*[59], the formation energy per O_2 molecule ΔH_O for an oxide XO_x was calculated using the following expression:

$$\Delta H_O = \frac{2}{x} [E(\text{XO}_x) - E(\text{X})] - E(\text{O}_2), \quad (5.4)$$

where $E(\text{X})$ is the energy of X in its elemental state, and $E(\text{O}_2)$ is the energy of an isolated O_2 molecule.

5.3.3 Computational Methods

Similar to the work in the preceding chapters, all spin-polarized total energy calculations and structure relaxations were performed with the Vienna *ab initio* simulation package (VASP), using a 500 eV energy cut-off and appropriate k -point meshes to obtain a convergence of better than 10 meV per formula unit. Structural relaxations were performed to a tolerance of 2×10^{-4} eV/atom in the total energy, yielding average forces of 0.01 eV/Å. TM atoms were initialized in high spin and low spin states, as well as in ferromagnetic (FM) and anti-ferromagnetic (AFM) orderings when relevant. The configuration yielding the lowest energy was kept as the groundstate. In the case of Jahn-Teller active ions (Mn^{3+} , Ni^{3+}), Jahn-Teller distortions were allowed by explicitly breaking the symmetry of the cell. Primitive cells were used in all calculations except for LiNiO_2 , where a cell of 6 formula units was used to allow Jahn-Teller distortions.

All GGA calculations were performed with the Perdew-Burke-Ernzerhof (PBE) functional.[113] For GGA+ U calculations, the rotationally invariant,[44] spherically averaged[57] version of GGA+ U was used, where only a single effective interaction parameter, U , is required to characterize the localization of the $3d$ electrons. Table 5.1 lists the U values used for the calculation of intercalation potentials. These values were obtained by averaging the U values found in [90] over the redox states found in the lithiated/delithiated structures.

Table 5.1: Values of the U parameters in eV.

	Olivine	Layered	Spinel
Mn	4.5	-	4.8
Fe	4.3	-	-
Co	5.7	5.1	-
Ni	6.1	6.4	-

Table 5.2: Average Li intercalation potentials vs. Li/Li⁺ in volts, obtained using GGA, GGA+ U , and HSE06 for complete delithiation compared to experiment. Parentheses indicate the use of the GGA value ($U = 0$). Experimental potentials have an estimated error of ± 0.1 V.

	GGA	GGA+ U	HSE06	Expt.	Ref.
LiCoO ₂	3.38	3.85	4.51	4.1	[101]
LiNiO ₂	3.08	3.92	4.14	3.9	[103]
LiTiS ₂	1.91	(1.91)	2.06	2.1	[107]
Li ₂ Ti ₂ O ₄ ¹	1.05	(1.05)	1.19	1.3	[108]
LiMn ₂ O ₄	3.37	4.04	4.25	4.1	[110]
LiMnPO ₄	2.99	4.01	3.87	4.1	[24]
LiFePO ₄	2.84	3.47	3.33	3.5	[14]
LiCoPO ₄	3.62	4.63	4.57	4.8	[18]
LiNiPO ₄	4.15	5.00	5.41	5.3 ²	[112]
Mean	2.93	3.54	3.70	3.69	
MAE ³	0.76	0.15	0.19	-	

5.4 Comparison of calculated intercalation potentials

Lithium intercalation potentials are obtained using Equation 5.3. Table 5.2 lists the Li intercalation potentials obtained with GGA, GGA+ U and HSE06, while Figure 5-1 shows the intercalation potential errors with respect to experiment.

For the layered oxides, HSE06 yields potentials that are significantly overestimated. As previously published,[99, 90] GGA severely underestimates the potentials by 0.7 V on average, while GGA+ U with a linear response U yields values close to experiment.

The Ti-containing structures (LiTiS₂, Li₂Ti₂O₄) do not require the use of a U correction because of the absence of localized 3d electrons in Ti. This is confirmed by the agreement with experiment of the GGA Li intercalation potentials for these structures. The agreement with experiment of the GGA intercalation potentials is significantly better for the Ti-containing compounds than for any of the other TM-containing compounds. The potentials obtained with HSE06 are greater than those obtained with GGA by 0.15 V and are in better agreement with experiment.

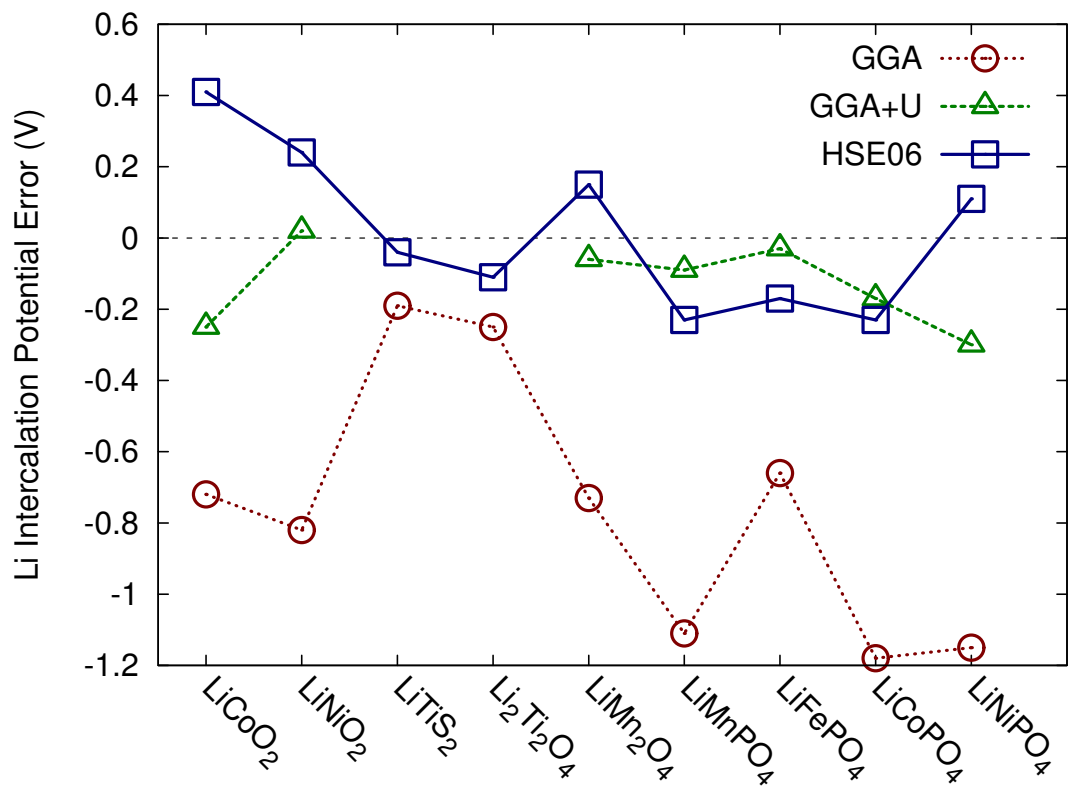


Figure 5-1: Difference between calculated and experimental Li intercalation potentials for GGA, GGA+*U*, and HSE06.

The Li intercalation potentials obtained for LiMn_2O_4 with HSE06 and GGA+ U are both nearly within experimental error. The HSE06 potential is greater than the one obtained with GGA+ U by 0.21 V. Once more, GGA underestimates the potential by approximately 0.7 V.

The olivines (LiMPO_4 , M=Mn, Fe, Co, Ni) yield potentials that are underestimated on average by 1 V with GGA. The Mn, Fe, and Co olivines are the only materials where the Li intercalation potentials obtained with HSE06 are smaller than those obtained with GGA+ U and by experiment. The smaller Li intercalation potentials obtained with HSE06 are correlated with the presence of the PO_4 polyanion. As opposed to the other olivines, the Li intercalation potential obtained for LiNiPO_4 with HSE06 is greater than those obtained with GGA+ U and by experiment. NiPO_4 is also the only olivine structure where the Ni magnetic moments obtained with HSE06 are greater than those obtained with GGA+ U .

5.5 Comparison of oxide formation energies

The O_2 molecule has an experimental binding energy of -5.12 eV.[71] GGA is known to overbind for O_2 , and a value of -6.04 eV was obtained with GGA in good agreement with previous calculations.[59, 114] HSE06 yields a binding energy of -5.16 eV, in much better agreement with experiment than GGA. According to the methodology of Ref. [59], one would therefore not expect HSE06 to introduce significant O_2 binding errors in the calculation of formation energies for non-transition metal oxides, where there is little correlation error on the metal oxidation.

Figure 5-2 shows the formation energy of various oxides when starting from their elemental form as calculated with GGA and HSE06, compared to experiment.[71, 60] The GGA formation energies are consistent with those of Ref. [59].

The GGA formation energy of the oxides of metals without localized $3d$ electrons (Li, Na, Mg, Al, Ca, Ti) is underestimated by a nearly constant error of 1.18 eV compared to experiment (the exclusion of Ti-containing oxides yields an average error of 1.32 eV, in agreement with Ref. [59]). The TM oxides containing atoms with

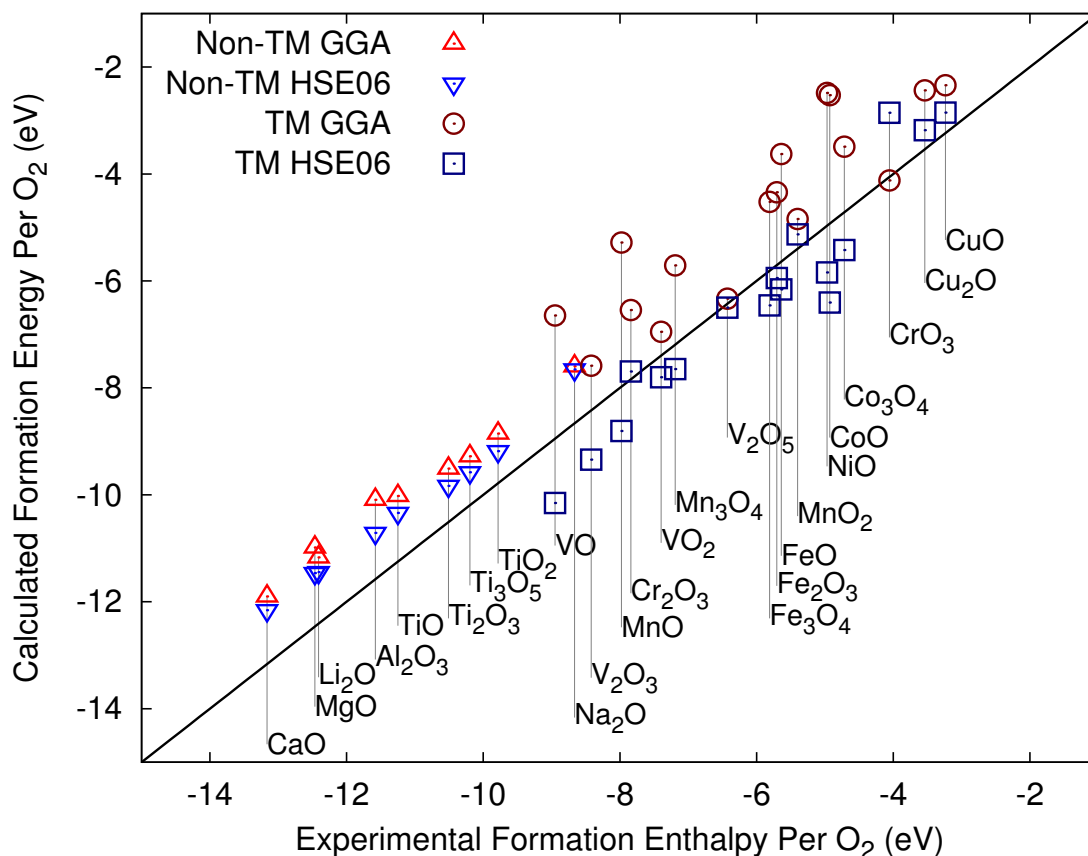


Figure 5-2: Formation energies of oxides per O_2 calculated with GGA and HSE06 plotted against experimental formation enthalpies.[71, 60]

localized $3d$ electrons (V, Cr, Mn, Fe, Co, Ni, Cu) have much more scatter in their calculated GGA formation energies and have an average error of 1.32 eV ($\sigma=0.20$ eV).

The HSE06 non-transition metal oxide formation energies are very similar to those obtained with GGA, although the average error is slightly less at 0.85 eV. The TM oxides with HSE06 yield formation energies that have less scatter than with GGA and have an average error of -0.35 eV ($\sigma=0.15$ eV). The agreement with experiment of formation energies for TM oxides is therefore better with HSE06 than with GGA.

5.6 Relationship between charge transfer and voltage in electrode materials

HSE06 is much more successful than GGA in predicting intercalation potentials in the presence of localized electrons with a mean absolute error of 0.2 V compared to 0.9 V with GGA. In the absence of localized electrons, such as in Ti-oxides or sulfides, HSE06 and GGA yield similar intercalation potentials. GGA+ U with a linear response U successfully reproduces experimental intercalation potentials with a mean absolute error of 0.1 V for TM-containing electrode materials with localized d electrons. The *average error* is therefore smaller for GGA+ U than HSE06 though it is not clear whether this difference in accuracy between GGA+ U and HSE06 is statistically significant given our small dataset. In GGA+ U , a correction to the self-interaction energy is only applied to the projected d states of the TM atoms. However, in HSE06 the use of HF exchange leads to corrections of self-interaction errors directly on all occupied eigenstates. The HSE06 functional should correct self-interaction errors in oxygen atoms as well, and the bonding environment of the oxygen atoms may therefore have a greater impact on redox energies in HSE06 than in GGA+ U . This indeed appears to be the case as HSE06 yields higher intercalation potentials than GGA+ U for simple oxides (LiCoO₂, LiNiO₂, LiMn₂O₄), but lower intercalation potentials for the polyanion-containing olivines (LiMPO₄, M=Mn, Fe, Co).

Figure 5-3 shows the difference in charge densities obtained with HSE06 and GGA+ U ($\rho^{\text{HSE06}} - \rho^{\text{GGA+U}}$) for the layered oxides at an isosurface level of ± 0.02 electron/ \AA^3 . GGA+ U calculations were performed with HSE06 geometries in order to obtain comparable charge densities. The yellow and blue isosurfaces indicate where HSE06 respectively locates more or less charge than GGA+ U . It is clear that GGA+ U locates more charge on the TM atom, while HSE06 locates more charge on the oxygen atom in both the lithiated and delithiated layered oxides. HSE06 therefore tolerates hybridization between the oxygen p and TM d orbitals more than GGA+ U , which forces localization in the TM d orbitals. The effect appears to be more pronounced for

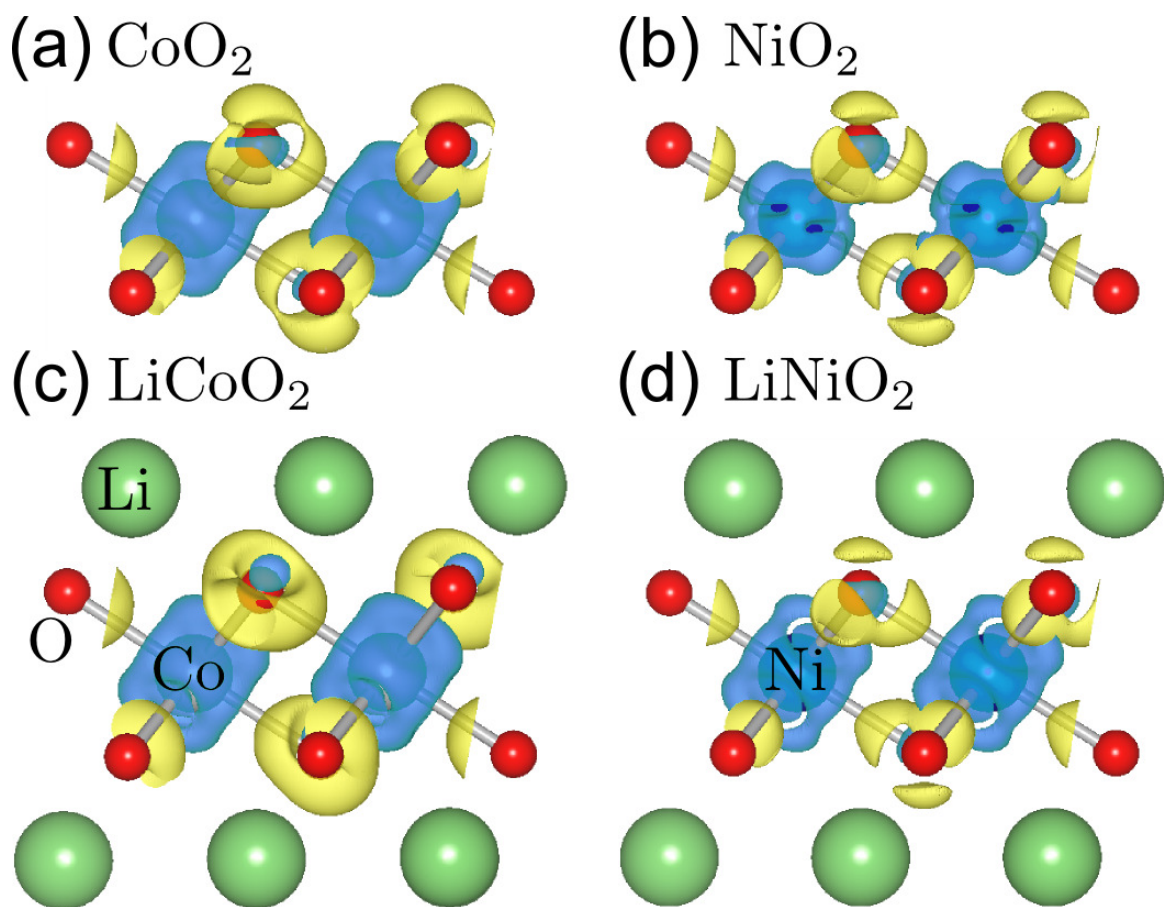


Figure 5-3: Isosurface of the difference between charge densities obtained with HSE06 and GGA+ U ($\rho^{\text{HSE06}} - \rho^{\text{GGA+U}}$). The yellow and blue represent the positive and negative 0.02 electron/ \AA^3 isosurfaces respectively. View along $[01\bar{1}]$, rendered using VESTA.[115]

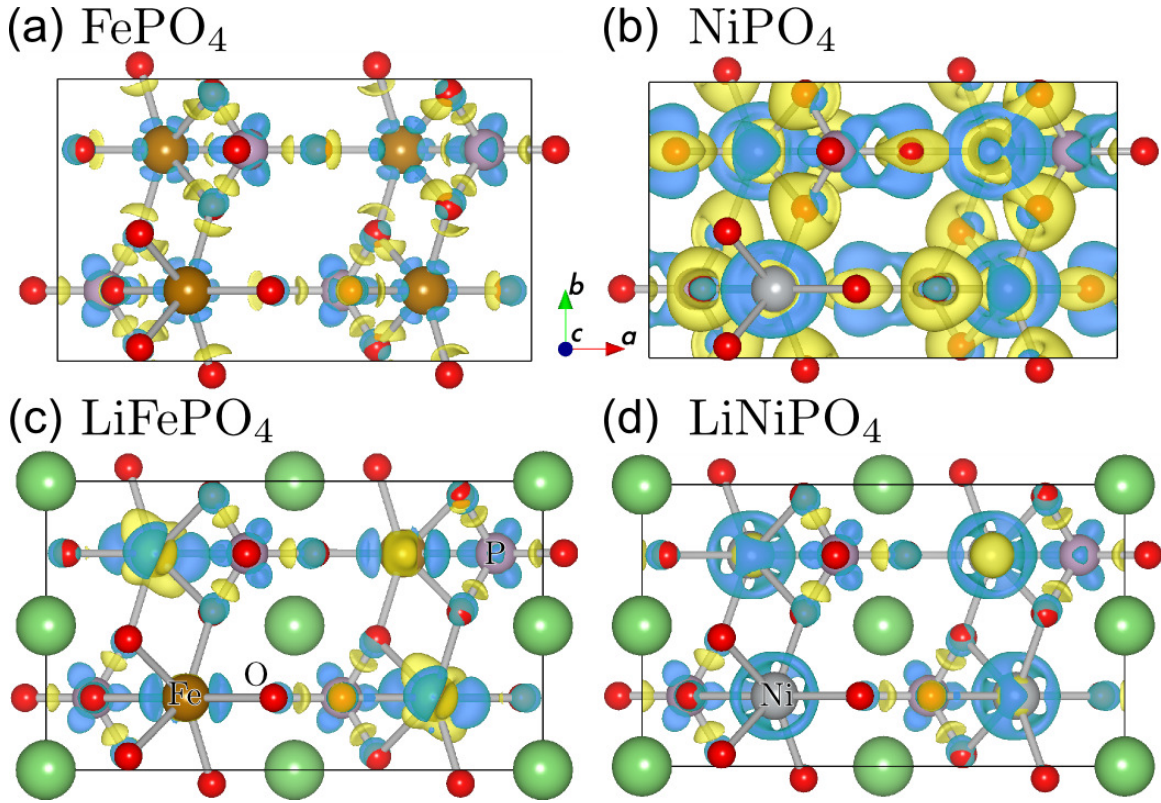


Figure 5-4: Isosurface of the difference between charge densities obtained with HSE06 and GGA+ U ($\rho^{\text{HSE06}} - \rho^{\text{GGA+U}}$). The yellow and blue represent the positive and negative 0.02 electron/ \AA^3 isosurfaces respectively.

Li_xCoO_2 than for Li_xNiO_2 as the isosurface volumes of Li_xCoO_2 are larger, which may be a reflection of more delocalized states and of the metallic nature of Li_xCoO_2 .^[116] Figures 5-1 and 5-3 respectively show a higher intercalation potential and greater localization of charge on the oxygen atoms with HSE06 for Li_xCoO_2 than for Li_xNiO_2 . Indeed, the intercalation potential obtained with HSE06 for LiCoO_2 is 0.7 V greater than with GGA+ U , compared to 0.22 V for LiNiO_2 . The Li intercalation potential depends on the energy difference between the lithiated and delithiated structures. One may speculate that the correction of self-interaction errors with HSE06 in the simple oxides stabilizes charge localization on the oxygen, thereby stabilizing the lithiated state and consequently raising the intercalation potential.

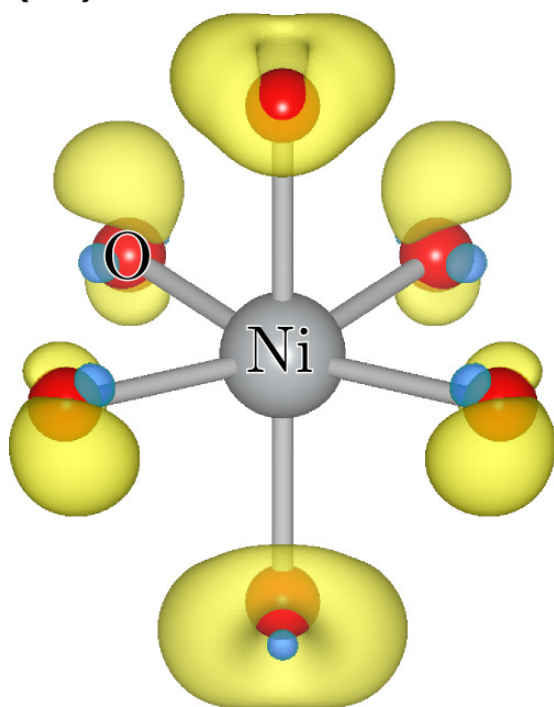
As opposed to the simple oxides, for the LiMPO_4 (M=Mn, Fe, Co) olivines, HSE06 underestimates the Li intercalation potentials compared to GGA+ U . Figure 5-4 shows the difference in charge densities obtained with HSE06 and GGA+ U ($\rho^{\text{HSE06}} -$

$\rho^{\text{GGA}+U}$) for MPO_4 and LiMPO_4 ($\text{M}=\text{Fe}, \text{Ni}$) at an isosurface of ± 0.02 electron/ \AA^3 . Figure 5-4(a) shows that in FePO_4 , $\text{GGA}+U$ localizes slightly more charge on the Fe and P ions than HSE06, and less around the oxygen atom along the Fe-O and P-O bonds. Figure 5-4(c) shows that in LiFePO_4 $\text{GGA}+U$ once again localizes more charge on the Fe ion than HSE06. Comparison of Figures 5-4(a) and (c) shows that differences in charge densities between HSE06 and $\text{GGA}+U$ in the PO_4 polyanion are practically unchanged upon lithiation from FePO_4 to LiFePO_4 . The $(\rho^{\text{HSE06}} - \rho^{\text{GGA}+U})$ charge density differences obtained for the simple oxides in Figure 5-3 are greater than the charge density differences obtained for Li_xFePO_4 in Figures 5-4(a) and (c). Indeed, the greater charge localization on the oxygen obtained with HSE06 compared to $\text{GGA}+U$ is more pronounced in the simple oxides than in the olivines. This is likely the cause of the lower HSE06 intercalation potentials for the olivines compared to $\text{GGA}+U$ and the higher HSE06 intercalation potentials for the simple oxides compared to $\text{GGA}+U$. The strong covalent bonding in the PO_4 group leads to less M-O hybridization. The decreased M-O hybridization in the olivines leads to less charge transfer to the oxygen upon lithiation than in the simple oxides. Hence, the correction of the self-interaction errors on oxygen orbitals by HSE06 may therefore have less of an impact in the olivines, and stabilization of the lithiated state by HSE06 may therefore not be as pronounced with the olivines than with the simple oxides, leading to lower intercalation potentials compared to $\text{GGA}+U$.

The Li intercalation potential obtained for LiNiPO_4 is higher with HSE06 than with $\text{GGA}+U$. Li_xNiPO_4 therefore behaves differently than the other olivines, which yield higher intercalation potentials with $\text{GGA}+U$. Figures 5-4(b) and (d) show the difference in charge densities obtained with HSE06 and $\text{GGA}+U$ for NiPO_4 and LiNiPO_4 . Figures 5-4(c) and (d) are very similar, showing LiFePO_4 and LiNiPO_4 have very similar differences in charge densities. However, a comparison of Figures 5-4(a) and (b) shows a marked contrast between the differences in charge densities for FePO_4 and NiPO_4 . Figure 5-4(b) shows HSE06 and $\text{GGA}+U$ yield electronic structures for NiPO_4 that are much more different than for the other olivines.

Charge transfer in electrode materials can be studied by subtracting the charge

(a) GGA+U



(b) HSE06

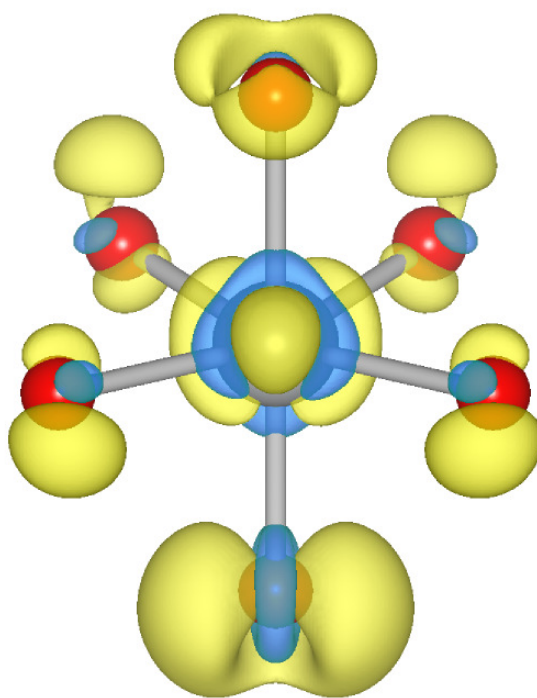


Figure 5-5: Isosurfaces of the change in charge density upon lithiation of NiPO_4 to LiNiPO_4 ($\rho_{\text{LiNiPO}_4} - \rho_{\text{NiPO}_4}$) with (a) GGA+ U and (b) HSE06. The yellow and blue represent the positive and negative 0.054 electron/ \AA^3 isosurfaces respectively. Only the NiO_6 octahedra is shown as no difference was visible on the P atom at the chosen isosurface value.

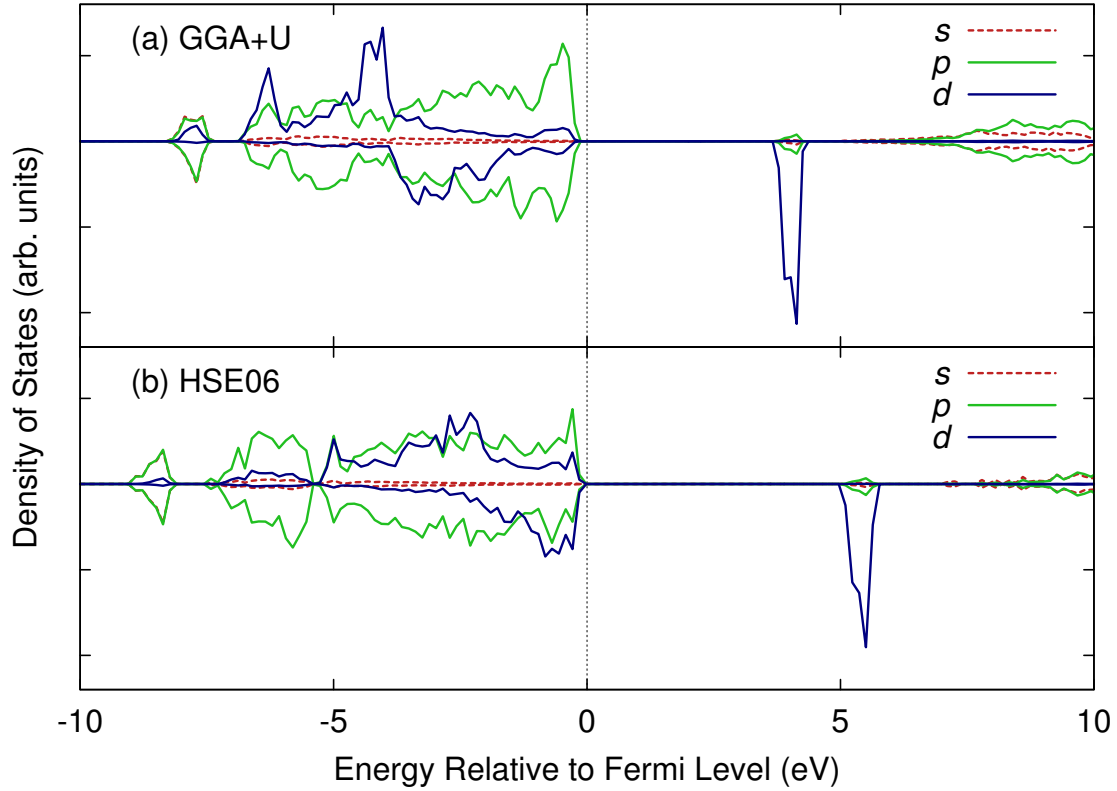


Figure 5-6: Summed projected DOS of atoms having parallel magnetic moments in AFM LiNiPO_4 calculated using (a) GGA+ U and (b) HSE06.

densities of lithiated and delithiated structures.[99] This was done for $\text{LiNiPO}_4/\text{NiPO}_4$ with HSE06 and GGA+ U . Figure 5-5 shows the ± 0.054 electron/ \AA^3 isosurfaces for the charge density differences: $(\rho_{\text{LiNiPO}_4}^{\text{HSE06}} - \rho_{\text{NiPO}_4}^{\text{HSE06}})$, and $(\rho_{\text{LiNiPO}_4}^{\text{GGA+U}} - \rho_{\text{NiPO}_4}^{\text{GGA+U}})$. Figure 5-5(a) shows there is no charge transfer occurring on the Ni ion with GGA+ U upon lithiation of NiPO_4 at this isosurface level. The absence of charge transfer on the Ni atom indicates the Ni atom is in the same valence state in both NiPO_4 and LiNiPO_4 with GGA+ U . Based on the magnetic moment of the Ni ion, it appears Ni is found in a Ni^{2+} state in both NiPO_4 and LiNiPO_4 with GGA+ U . Figure 5-5(b) shows the Ni ion gains charge upon lithiation with HSE06, furthermore the positive isosurface shape is characteristic of a t_{2g} orbital, which is consistent with a Ni^{3+} to Ni^{2+} reduction with both ions in a high spin state.

Based on the observed charge transfer upon Li insertion, we can argue that in GGA+ U , the relative position of the Ni and oxygen electronic levels near the Fermi

level in Li_xNiPO_4 is different than in HSE06, we can further confirm this by examining the projected DOS. Figure 5-6 shows the summed projected DOS of the atoms in LiNiPO_4 having parallel magnetic moments. Because the ground state magnetic ordering of LiNiPO_4 is AFM, excluding the contributions to the projected DOS of the atoms having antiparallel magnetic moments allows the identification of the spin features in the DOS. Figure 5-6 shows the oxygen levels are higher in energy than the Ni levels with GGA+ U , while oxygen and Ni levels are found at similar energies and have greater hybridization with HSE06. Observations of a similar nature have previously been reported for NiO. Indeed, the relative position of Ni and oxygen levels in NiO have been investigated both experimentally[117, 118] and theoretically.[119] When a Ni^{2+} is replaced by a Li^+ in a NiO crystal, the resulting hole is seen to reside on the oxygen. The removal of Li from LiNiPO_4 can be seen as the addition of a hole. GGA+ U places the hole on the oxygen, while HSE06 distributes the hole over both Ni and O. The presence of a PO_4 polyanion makes Li_xNiPO_4 significantly different from NiO, and it is not obvious which result more accurately represents reality. Agreement with the experimental Li intercalation potential may not be the best metric since the intercalation potential of Li_xNiPO_4 is very high and above the potential of standard electrolytes. Furthermore, only a single account of electrochemical cycling of LiNiPO_4 was found in the literature and the intercalation potential was determined from only one cycle.[112] Assuming HSE06 yields a more accurate description of the physics occurring in Li_xNiPO_4 , one may speculate GGA+ U is in fact underestimating the Li intercalation potential of Li_xNiPO_4 .

5.7 Oxides

The formation of oxides requires the transfer of electrons between significantly different environments. Wang *et al.*[59] have shown that oxide formation energies obtained with GGA have errors stemming from two main causes. The first is the overbinding of the O_2 molecule. The second is the lack of correction for self-interaction errors found in correlated states such as TM $3d$ orbitals.

The overbinding of the O₂ molecule in GGA can be addressed by artificially using a corrected value for the O₂ energy. Highly correlated electrons can be addressed by using GGA+ U in the oxides. However, GGA+ U with the same U cannot be used for TMs in their elemental forms as correct metallic states will not be obtained. GGA+ U can therefore only be used for reaction energies involving solely oxides.

HSE06 yields an accurate bonding energy for the O₂ molecule, and largely corrects self-interaction errors in localized electronic states. One would therefore expect HSE06 to give significantly more accurate oxide formation energies than GGA. Figure 5-2 shows that HSE06 does indeed produce slightly more accurate formation energies for the non-transition metal oxides, as well as more accurate and less scattered formation energies for the TM oxides. However, it is surprising to realize that after correcting the non-transition metal oxide formation energies for the binding error in the O₂ molecule, the GGA results are actually closer to experiment than HSE06. After correction, the average errors compared to experiment are 0.26 eV and 0.81 eV for GGA and HSE06 respectively. For the TM oxides, after correcting for the O₂ binding energy, HSE06 is only slightly more accurate than GGA.

5.8 Benefits and drawbacks of hybrids compared to GGA+ U

The greatest drawback of hybrid methods compared to GGA+ U is computational cost. While the screening introduced in HSE06 makes it less costly than its unscreened limit, PBE0,[120] computational cost with HSE06 is still on average 40× greater than with GGA+ U for the calculations in this work. The intercalation potential of LiNiO₂ was calculated with PBE0 to verify that the screening introduced in HSE06 did not significantly affect the values of calculated intercalation potentials. The intercalation potential obtained with PBE0 was only 20 mV greater than the one obtained with HSE06. The PBE0 and HSE06 calculations were performed with identical k -point grids, and therefore, the PBE0 result is not as well converged as the HSE06 result.

Indeed, the screening of HSE06 facilitates the energy convergence with respect to k -points.[94]

The greatest advantage of HSE06 over GGA+ U is that it is a chemistry and structure agnostic functional. In GGA+ U , the U parameter is species- and environment-dependent. It is therefore up to the user to determine if the U parameter is appropriate for a given species in a given structure and calculations with different U parameters cannot directly be used together, giving GGA+ U calculations with a specific value of U limited span in composition space. This is not the case with HSE06, as it does not contain any species- or environment-dependent parameters. However, HSE06 does contain fixed parameters that could be varied, namely the HF mixing ($\frac{1}{4}$) and screening (μ) of Equation 5.2.

The choice between HSE06 and GGA+ U will therefore depend on the resources available. For simple intercalation potential calculations, if a U parameter is available, HSE06 does not present major advantages that outweigh its greater cost. HSE06 and GGA+ U yielded significantly different physics only in the case of Li_xNiPO_4 , which has an extremely high intercalation potential. However, HSE06 may be required to study specific questions that benefit from the correction of self-interaction errors for all occupied eigenstates as opposed to only the ones treated with a U parameter. We will demonstrate one such example in Chapter 6, where the use of HSE06 is necessary to achieve the localization of polaronic charge carriers in LiMnPO_4 . In addition, HSE06 is a consistent approach that can be used across all oxidation states, whereas the U parameter in GGA+ U would change with valence state and would not be applicable to the metallic state.

5.9 Conclusion

Redox reactions are important in many technological and environmental processes. DFT calculations using GGA functionals fail to model these reactions when they involve localized electrons, such as the $3d$ electrons of TMs. The applicability of screened hybrid methods to the study of redox reactions in the presence or absence

of localized electrons has been demonstrated.

The screened hybrid functional HSE06 was compared to GGA and GGA+ U for the study of electrode materials and oxide formation. The correction of self-interaction errors in HSE06 through the use of HF exchange leads to a more accurate treatment of the $3d$ electrons in TM atoms. HSE06 and GGA+ U with a linear response U yield similar accuracies for Li intercalation potentials. However, HSE06 does not require any adjustable parameters and is applicable irrespective of the type of atoms present in the structures of interest.

The prediction of Li intercalation potentials with HSE06 is sensitive to the bonding environment of the oxygen, in a way not found in GGA+ U . The correction of self-interaction errors for all eigenstates with HSE06 appears to lead to greater charge localization on the oxygen orbitals in the simple oxides. The correction of self-interaction errors stemming from the oxygen atoms may stabilize charge transfer to the oxygen and be the cause of the higher intercalation potentials obtained with HSE06 for the simple oxides. The presence of PO_4 polyanions appear to mitigate this effect, leading to lower intercalation potentials with HSE06.

HSE06 yields more accurate oxide formation energies than uncorrected GGA. GGA+ U cannot be used for the calculation of oxide formation energies involving TMs because the same U cannot be used to properly model the metallic states of TMs in their elemental form.

The computational cost is greater for HSE06 than for GGA or GGA+ U . For the study of redox reactions involving localized electrons, the choice between HSE06 and GGA+ U will therefore hinge on the availability of an appropriate U , whether metallic states need to be modeled, and the available computational resources.

Chapter 6

Polaron migration and phase separation in LiMnPO_4 and LiFePO_4 using hybrid functionals

6.1 Polaronic conductivity in the LiMnPO_4 and LiFePO_4

A slow moving electron or hole in a dielectric crystal induces a local lattice distortion, which acts as a potential well that causes the charge carrier to become self-trapped.[121] The quasiparticle formed by the charge carrier and its self-induced distortion is called a small polaron if the range of the lattice distortion is of the order of the lattice constant. Previous theoretical work by Maxisch *et al.*[122] and various experimental works[123, 124] have provided evidence of a small polaron[125, 121] diffusion mechanism of electronic conduction in LiFePO_4 . Electronic conduction in the structurally similar LiMnPO_4 is likely to be via a similar mechanism. Indeed, Yamada *et al.*[16, 12] postulated that a large polaron effective mass in the Mn olivine due to the Jahn-Teller active Mn^{3+} ion is the likely explanation for the observed low electronic conductivities. Yamada *et al.* also suggested large local lattice deformation due to Mn^{3+} during phase transformation to be a further factor limiting the intrinsic

sic kinetics in LiMnPO_4 . Kang *et al.*'s attempts to optimize LiMnPO_4 [76] using a proven off-stoichiometric optimization approach for LiFePO_4 [75] have also met with limited success, suggesting that there are other intrinsic kinetic limitations compared to LiFePO_4 .

In this thesis, we investigated the polaron migration and phase separation in LiMnPO_4 and LiFePO_4 using hybrid density functional theory based on the Heyd-Scuseria-Ernzerhof (HSE06) functional.[3, 4, 94] In Chapter 5, we have demonstrated the effectiveness of hybrid functionals, and in particular the HSE06 functional, as an alternative approach to dealing with the over-delocalization of d -orbitals in transition metal ions by conventional semi-local functionals, albeit at a significantly higher computational cost than $\text{GGA}+U$. In recent years, hybrid calculations have seen greater use in solid-state applications, such as the study of redox potentials[5] and polarons in doped BaBiO_3 [126] and cuprates.[127] The advantage of hybrid functionals over $\text{GGA}+U$ is the lack of a species-specific U parameter and perhaps more importantly, a more universal treatment of the self-interaction error over all species and occupied states rather than specific atomic orbital projections on specific ions.

6.2 Methods

6.2.1 Small polaron migration

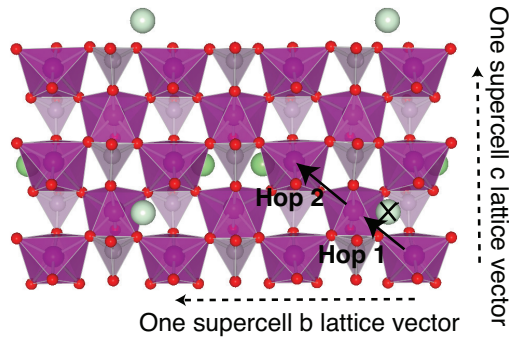


Figure 6-1: Single layer viewed in projection along the $[100]$ direction showing polaron hops considered. The lithium atom marked with the X is the atom removed when calculating polaron barriers in the presence of vacancies.

We adopted the same methodology used by Maxisch *et al.*[122] for their GGA+*U* study of polarons in the Fe olivine as well as Iordanova *et al.*[128, 129] for their study of polarons in oxides. We will briefly summarize the methodology here, and interested readers are referred to that work for more details.

The olivine LiMPO₄ compounds have an orthorhombic *Pnma* spacegroup (Fig. 1-2) where the transition metal (M) ions are sixfold coordinated by oxygen ions forming layers of edge-sharing octahedra. Because the layers are separated by PO₄ tetrahedra, we can assume that electron transfer is confined to a single layer, and no charge transfer occurs between layers (hop 1 in Fig. 6-1). To fulfill the requirements of spin conservation and the Frank-Condon principle, we calculated the polaron migration barriers using an A-type anti-ferromagnetic structure.[130] A 1 × 2 × 2 supercell containing 16 formula units was used to minimize the interaction between periodic images, while keeping computational costs at a reasonable level.

In LiMPO₄, polaronic charge carriers are holes on M³⁺ sites whereas in MPO₄, the charge carriers are electrons on M²⁺ sites. A hole (electron) polaron was formed on one of the transition metal ions by removing (adding) an electron to the fully relaxed LiMPO₄ (MPO₄) supercell. Overall charge neutrality was preserved via a compensating background charge. If $\{\mathbf{q}_i\}$ and $\{\mathbf{q}_f\}$ denote the initial and final ion positions respectively, the migration of the polaron can then be described by the transfer of the lattice distortion over a one-dimensional Born-Oppenheimer surface, with a energy maximum at a configuration between $\{\mathbf{q}_i\}$ and $\{\mathbf{q}_f\}$. To determine this maximum, we computed the energies for a set of cell configurations $\{\mathbf{q}_x\}$ linearly interpolated between $\{\mathbf{q}_i\}$ and $\{\mathbf{q}_f\}$, i.e., $\{\mathbf{q}_x\} = (1-x)\{\mathbf{q}_i\} + x\{\mathbf{q}_f\}$ where $0 < x < 1$.

During the charging and discharging of a battery, lithium or vacancies are injected in the pristine olivine structure respectively. To study polaron migration in the presence of lithium and vacancies, we introduced a single lithium or vacancy into the supercell and calculated the barrier for the polaron to migrate from a M site nearest to the lithium ion/vacancy to a M site further away within the same layer (hop 2 in Fig. 6-1).

6.2.2 Phase separation behavior

To study the phase separation behavior of the Mn and Fe olivines, we calculated the formation energies $\Delta E(x)$ of Li_xMPO_4 at $x = 0.25, 0.5, 0.75$, which is given by the following equation:

$$\Delta E(x) = E(\text{Li}_x\text{MPO}_4) - (1 - x) \times E(\text{MPO}_4) - x \times E(\text{LiMPO}_4) \quad (6.1)$$

For the formation energy calculations, only a single unit cell of LiMPO_4 was used, and all symmetrically distinct charge ordering configurations at each concentration were calculated. The magnetic moments were initialized in the ground state anti ferromagnetic configuration, and the net difference in the number of spin-up and spin-down electrons was fixed at the value expected from the number of M^{2+} and M^{3+} ions present in the structure. For example, for $\text{Li}_{0.25}\text{FePO}_4$, one of the four Fe ions in the unit cell is a Fe^{2+} , and the remaining Fe ions are Fe^{3+} , resulting in an expected +1 net difference in the number of spin-up and spin-down electrons in the unit cell.

6.2.3 Computational methodology

With the exception of the k -point grid for the polaron supercell calculations, all calculations in this work was performed using the same Vienna *ab initio* simulation package (VASP) and parameters (energy cutoff, etc.). For the polaron supercell calculations, a minimal Γ -centered $1 \times 1 \times 1$ k -point grid was used to keep computational cost at a reasonable level. No k -point convergence study was done as any increase in the k -point grid size rendered the computation far too expensive. Nonetheless, given the size of the supercell, we would expect the calculations to be reasonably converged. The single unit cell Li_xMPO_4 formation energies were calculated using a larger k -point grid chosen such that total energies were converged to within 10 meV/formula unit.

Table 6.1: Average M-O bond lengths of polaron and non-polaron sites in the Mn and Fe olivines in angstroms. Ranges are shown in brackets for the polaron sites.

	Average M-O bond length in LiMPO ₄ (Å)		Average M-O bond length in MPO ₄ (Å)	
	hole polaron site	non-polaron site	electron polaron site	non-polaron site
Mn	2.07 (1.92-2.28)	2.20	2.18 (2.02-2.38)	2.07
Fe	2.06 (1.99-2.13)	2.16	2.13 (1.97-2.26)	2.03

6.3 Polaron bond lengths and electronic structure

Table 6.1 summarizes the average M-O bond lengths for the polaron and non-polaron sites in the supercell structures. Though the average polarization induced by polaron formation appear to be similar for the Mn and Fe systems, the actual lattice distortions are very different, as evidenced by the much wider range of bond distances for both the hole and electron Mn polarons. This observation may be attributed to the fact that Mn³⁺ is a Jahn-Teller active ion for which orbital degeneracy is usually broken by a distortion of the MO₆ octahedron.[131]

Figure 6-2a-d shows the densities of states (DOSs) stacked area plots for the LiMPO₄ structures where we attempted to localize a single hole polaron using HSE06 and GGA+*U*. To obtain a more accurate DOS, a non-self-consistent run using a 2 × 2 × 2 Monkhorst-Pack *k*-point grid on the structure optimized using the default single Γ point was performed.

For LiFePO₄, clear evidence of a localized polaron can be seen in the GGA+*U* and HSE06 DOSs. Fe²⁺ has a high-spin $t_{2g}^3(\uparrow)t_{2g}^1(\downarrow)e_g^2(\uparrow)$ electronic configuration. Removal of an electron to form a hole polaron should result in a spin-down state being pushed above the Fermi level, which can be seen in Figures 6-2(c) and 6-2(d). We also note that the polaron states and the states near the Fermi level have predominantly *d* character in the Fe olivine.

For LiMnPO₄, we were unable to localize a hole polaron using GGA+*U*. The electronic structure of Mn²⁺ is $t_{2g}^3(\uparrow)e_g^2(\uparrow)$. Removal of an electron to form a hole polaron should result in a spin-up state being pushed above the Fermi level. No such state was observed in the GGA+*U* DOS (Figure 6-2(a)), while clear evidence of a localized hole polaron in LiMnPO₄ was seen in the HSE06 DOS (Figure 6-2(b)).

Similar observations were made for electron polaron localization in FePO_4 and MnPO_4 based on the DOSs (Figure 6-2e-h).

The reason for this failure of $\text{GGA}+U$ is apparent when we consider the HSE06 orbital-projected DOSs, which clearly shows a significant contribution from the oxygen p orbitals in the polaron states and the states near the Fermi level. This observation points to an inherent difference between the electronic structures of LiMnPO_4 and LiFePO_4 ; the transition metal is much more strongly hybridized with the nearest neighbor oxygen atoms in the Mn olivine compared to the Fe olivine. Indeed, the hole polaron charge densities clearly showed a greater localization of charge on the Fe ion in LiFePO_4 , while the polaron charge carrier appeared to have localized in Mn- d -O- p hybrid orbitals in LiMnPO_4 (see Figure 6-3). In their investigation of polaronic hole trapping in doped BaBiO_3 , Franchini *et al.*[126] found that they were unable to stabilize a bipolaron using a one-center $\text{LDA}+U$ treatment because the Bi s orbitals were too delocalized. In the case of the Mn olivine, we believe that the reason for the failure of $\text{GGA}+U$ is different: the relevant localized orbitals in which to apply self-interaction correction are not the onsite atomic transition metal d orbitals, but rather the hybridized molecular orbitals formed by specific transition metal d orbitals and oxygen p orbitals. To our knowledge, no existing DFT code provides a functionality to apply Hubbard U corrections to non-atomic orbitals. A recent work by Ylvisaker *et al.* applied a novel tight-binding Hamiltonian approach to apply U corrections to molecular oxygen π^* orbitals in RbO_2 ,[132] but the greater complexity of the olivine structure makes developing a similar model difficult. In this work, we chose to avoid the issue of applying a Hubbard U on hybridized orbitals by using hybrid functionals.

6.4 Polaron migration barriers

Figure 6-4 shows the calculated LiMPO_4 free hole and MPO_4 free electron polaron migration barriers. For the Fe olivine system, we performed both HSE06 and $\text{GGA}+U$ calculations to compare the differences in the predictions between the two treatments

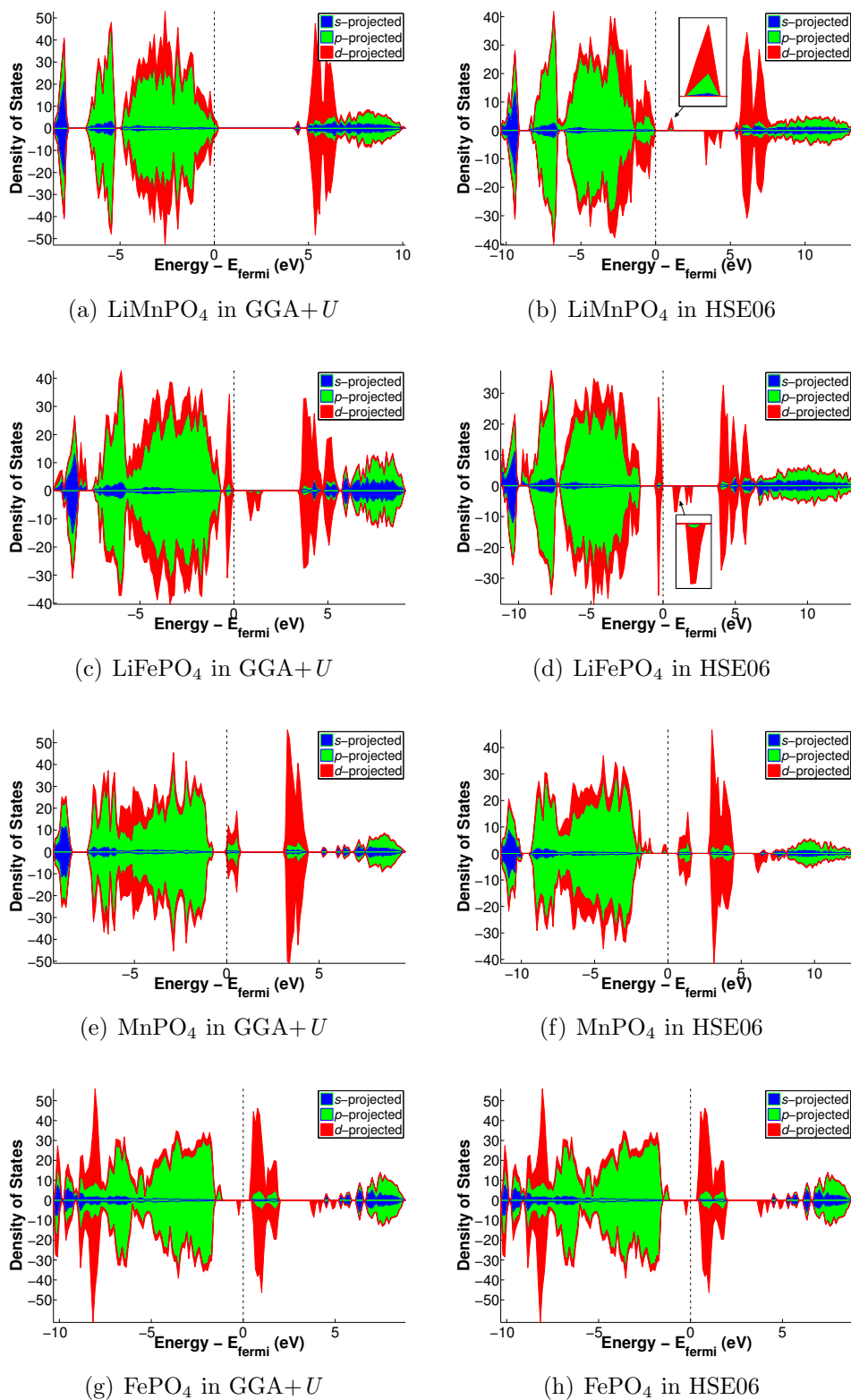
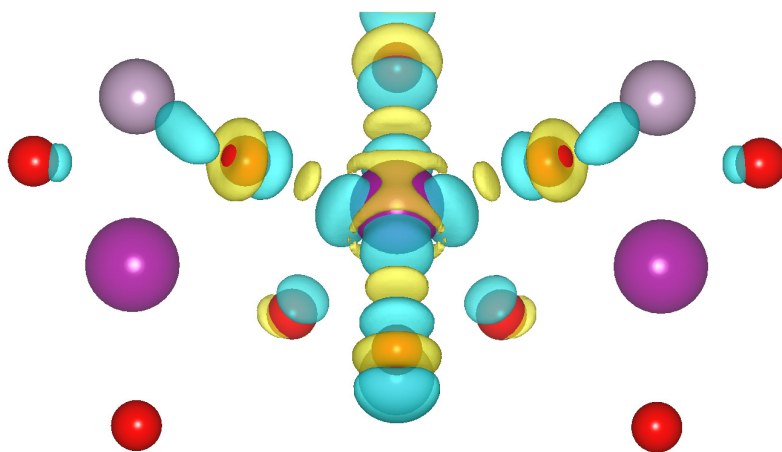
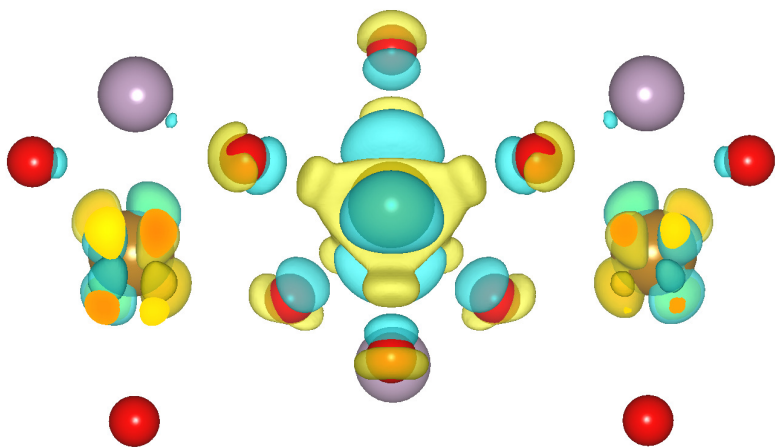


Figure 6-2: DOS stacked area plots for LiMPO_4 and MPO_4 olivines containing a single hole and electron polaron respectively. The height of each colored area shows the contribution of each orbital type at each energy level.



(a) LiMnPO₄ hole polaron



(b) LiFePO₄ hole polaron

Figure 6-3: Isosurface of LiMPO₄ hole polaron differential charge density ($\rho_{\text{polaron cell}} - \rho_{\text{neutral cell}}$) at a 0.005 electron \AA^{-3} level calculated in HSE06.

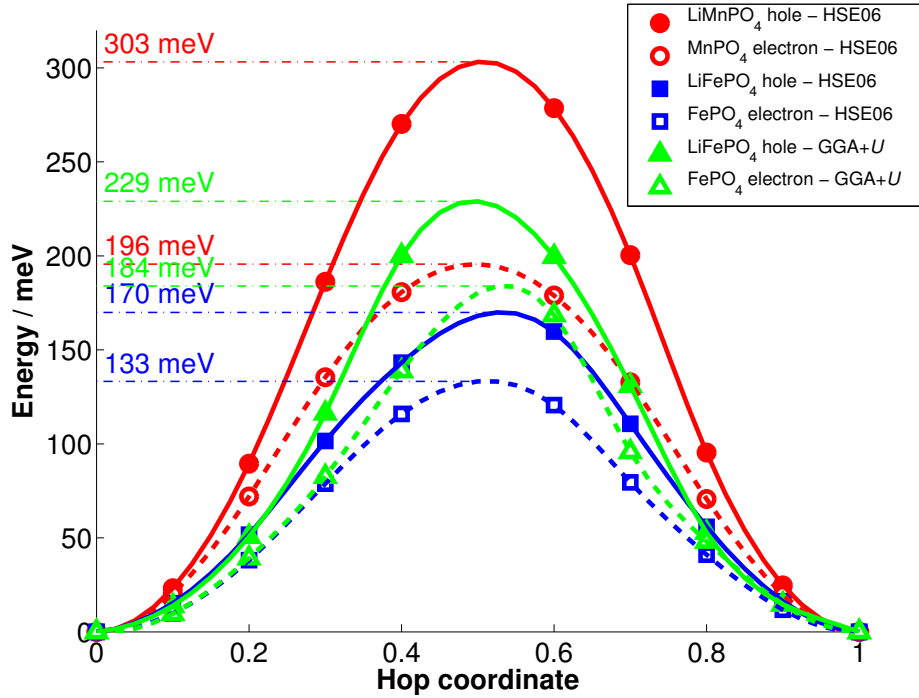


Figure 6-4: Calculated free polaron migration barriers in HSE06 and GGA+ U .

of the polaron problem. Only HSE06 results are presented for the Mn system as we were unable to localize polarons using GGA+ U with the self-consistently determined U .

For LiFePO₄ and FePO₄, the HSE06 polaron migration barriers were smaller than the GGA+ U ones. As highlighted in previous work,[5], we found that HSE06 in general tends to result in a smaller amount of charge localization as compared to GGA+ U . Hence, it is likely that the polaron migration is artificially aided by some residual itinerant character of the charge carriers. The GGA+ U migration barriers are in good agreement with the values previously calculated by Maxisch *et al.*[122]

Comparing the Mn versus Fe HSE06 barrier values, we see that the free polaron migration barriers in the Mn olivine system are significantly higher than in the Fe olivine. The free hole polaron migration barrier in LiMnPO₄ is around 135 meV higher than that in LiFePO₄, while the free electron polaron migration barrier in MnPO₄ is around 72 meV higher. Such significantly higher polaron migration barriers would imply much lower electronic conductivities in the Mn olivine in both the charged and

discharged state compared to the Fe olivine.

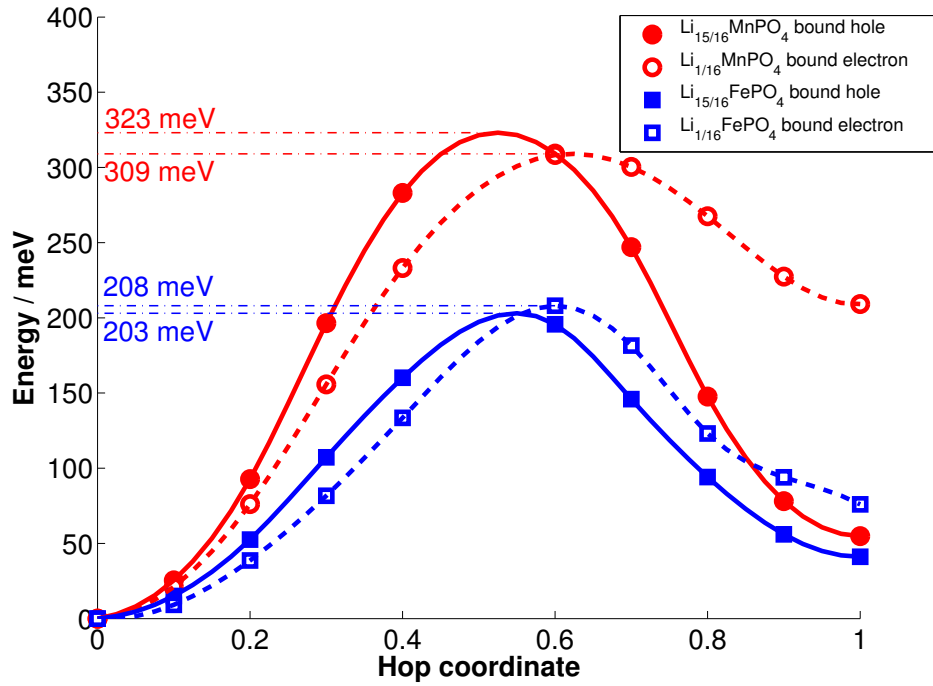


Figure 6-5: Calculated bound polaron migration barriers in HSE06.

We also investigated the polaron migration barriers in the presence of lithium ions (in MPO_4) or vacancies (in LiMPO_4) to simulate electronic conduction during the initial stages of charging or discharging. Figure 6-5 shows the calculated barriers for polaron migration from a site nearest to the lithium ion or vacancy to a site further away. As we are only interested in relative barriers, we made no corrections for the interactions between periodic images of the lithium ion or vacancy and charge carriers, as was done in Maxisch *et al.* work[122] (because the charges and structures are similar in all instances, the corrections would amount to approximately the same additive term).

We may observe that the bound polaron migration barriers are higher than the free polaron migration barriers. In particular, the electron polaron migration barrier in $\text{Li}_{1/16}\text{MnPO}_4$ increases significantly, and both hole and electron migration barriers are around 100-120 meV higher in the Mn olivine than the Fe olivine. Hence, polarons have a tendency to become trapped by the presence of lithium ions and vacancies,

further reducing electronic conductivity.

In a recent work, Seo *et al.*[133] reported a GGA+ U polaron migration barrier of more than 808 meV in Li_xMnPO_4 calculated via a nudged elastic band method and noted this value to be “over 100 meV” higher than the barrier in Li_xFePO_4 calculated by Maxisch *et al.*[122] However, the barrier calculated by Seo *et al.* is for an “undefined” combination of a lithium migration and a polaron migration process, and hence cannot be compared directly to either Maxisch *et al.*’s work or the barriers calculated in this work. Furthermore, Seo *et al.* used a supercell with an approximate 1/3 Li concentration. Polaron migration barriers under 1/3 Li concentration are likely to be different from the far more dilute 1/64 concentration investigated by Maxisch *et al.* and 1/16 concentration investigated in this work.

6.5 Li_xMPO_4 formation energies

The structural evolution of an electrode material upon delithiation can be evaluated by computing the formation energies of states with lithium content intermediate between the lithiated and fully delithiated states. The formation energy of Li_xMPO_4 , $\Delta E(x)$, is its energy minus the concentration weighted average of MPO_4 and LiMPO_4 . A large positive $\Delta E(x)$ indicates that no intermediate phases form and a two-phase reaction is likely, while a negative $\Delta E(x)$ indicate the presence of ordered Li-vacancy solid solutions.

Figure 6-6 presents the formation energies of Li_xMPO_4 calculated using different functionals. In agreement with the previous work of Zhou *et al.*,[134] standard GGA led to qualitatively incorrect negative or near-zero formation energies for the intermediate phases in the Li_xMPO_4 system. Both LiFePO_4 and LiMnPO_4 are well-known to undergo a two-phase reaction upon delithiation,[9, 16] implying that the formation energy should be positive. GGA+ U with the self-consistently determined U gives positive formation energies. Zhou *et al.* has conclusively shown that accounting for the correlation between the localized d -orbitals of the transition metal is necessary to obtain this phase separating behavior. We would like to note that the GGA+ U

formation energy for $\text{Li}_{0.5}\text{FePO}_4$ we calculated (≈ 13 meV) is much lower than the value reported for $U = 4.5$ eV (≈ 80 meV) in ref [26], but is very close to the lowest formation energy for the same structure reported in a later work by the same author[135] for a set of 245 calculated structures used to fit a cluster expansion.[136]

The HSE06 formation energies for the Li_xMnPO_4 structures are higher than the GGA+ U values and predicts qualitatively correct phase separating behavior.

However, the results of the HSE06 Li_xFePO_4 formation energies are surprising. We would expect that a functional that is designed to explicitly treat the self-interaction error would result in at least qualitatively correct formation energies. As can be seen from Figure 6-6, the HSE06 formation energies for Li_xFePO_4 for $x = 0.25, 0.75$ are even more negative than the GGA formation energies. This is despite us having achieved the proper charge localization for these structures, *i.e.*, the calculated magnetic moments of the Fe ions confirmed that $\text{Li}_{0.25}\text{FePO}_4$ contains one Fe^{2+} and three Fe^{3+} ions, while $\text{Li}_{0.75}\text{FePO}_4$ contains one Fe^{3+} and three Fe^{2+} ions (see Appendix A).

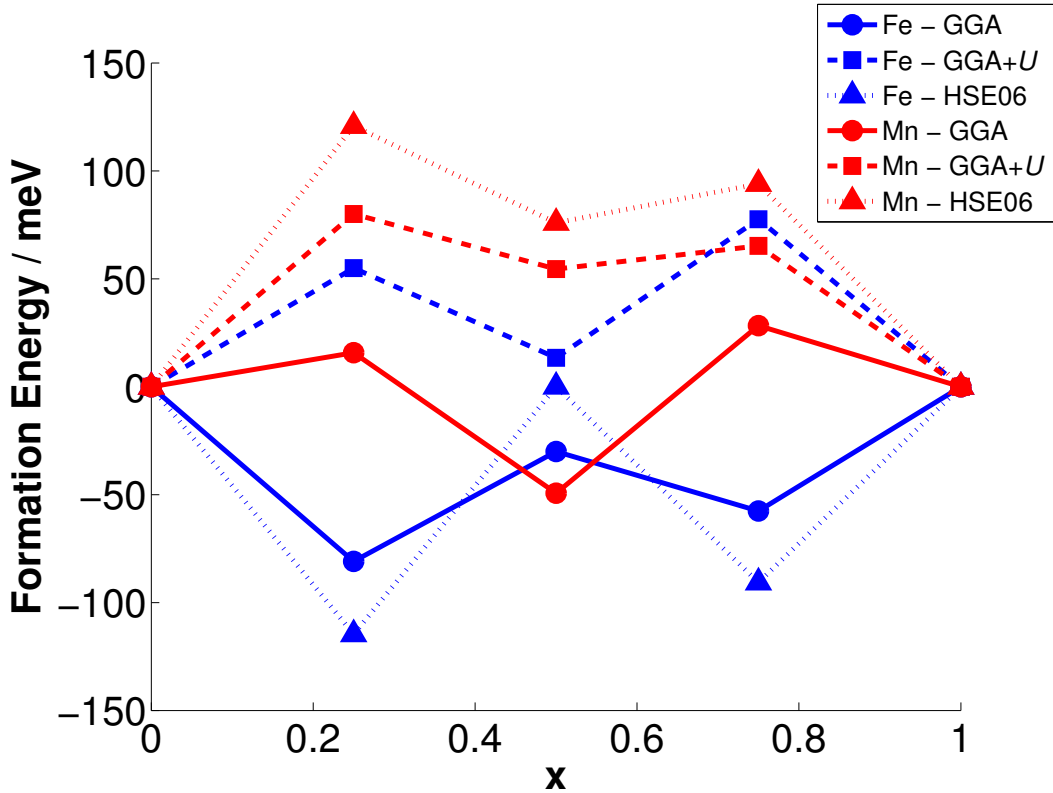


Figure 6-6: Formation energies of Li_xMPO_4 using different functionals.

6.6 Intrinsic kinetic differences between the Mn and Fe olivines

Our results show that there are intrinsic differences in the electronic structures and kinetics of LiMnPO_4 and LiFePO_4 . The free hole and electron polaron migration barriers in the Mn olivine are predicted to be 133 meV and 63 meV higher than that in Fe olivine respectively. In the presence of lithium ions or vacancies, both the hole and electron polaron migration barriers are $\approx 100\text{-}120$ meV higher in the Mn olivine relative to the Fe olivine. In terms of the formation energies of the partially lithiated LiMPO_4 structures, we found that the Mn and Fe systems had approximately the same formation energies in $\text{GGA}+U$, and that the HSE06 formation energies for the Mn olivine were similar to the $\text{GGA}+U$ values.

Using the calculated polaron migration barriers, we may make an approximation to the difference in electronic conductivities between the Mn and Fe olivines. Assuming the same attempt frequency and a simple Arrhenius like relationship, the **free hole polaron migration is predicted to be about 177 times slower in LiMnPO_4 than in LiFePO_4 at room temperature, while the electron polaron migration is predicted to be about 11 times slower in MnPO_4 than in FePO_4 .** In the presence of Li ions or vacancies, both hole and electron migration are predicted to be around 77 times slower in the Mn olivine as compared to the Fe olivine. These predictions are in good agreement with the results of Yonemura *et al.*[12] who measured conductivities of $< 10^{-10} \text{ Scm}^{-1}$ for LiMnPO_4 compared to 10^{-8} Scm^{-1} for LiFePO_4 . It should be noted that there are some discrepancies in the literature. For instance, Delacourt *et al.*[25] found that LiMnPO_4 had a five orders of magnitude lower conductivity, which implies a factor of two higher activation energy, compared to LiFePO_4 . Nonetheless, the qualitative assessment that the Mn olivine has a much lower electronic conductivity still stands.

There are several implications from the much lower conductivity for LiMnPO_4 relative to LiFePO_4 . Firstly, size effects would be far more pronounced, and indeed Drezen *et al.*[137] found that a reduction in particle size from 270 nm to 140 nm sig-

nificantly improved the rate capability of LiMnPO_4 as an electrode, and even better performance was subsequently achieved by Martha *et al.*[41] with carbon-coated 30-nm particles. It should be noted that carbon coating merely improves inter-particle conductivity and not intra-particle conductivity; hence a small particle size is still necessary to achieve low transport distances. If the requisite particle sizes to achieve a similar performance as LiFePO_4 are significantly smaller, the overall effective gravimetric and volumetric capacity of the cathode could be adversely affected, and the potential thermal stability issues in the charged state[28, 29, 2] could be further exacerbated.

The GGA+ U formation energies for states with intermediate lithium concentration in the Fe and Mn olivine are similar and consistent with the observed two-phase equilibria in both systems. The HSE06 formation energies were too unreliable for us to make any reasonable assessment. While we are unable to provide a quantitative discussion of the phase separation kinetics in the olivines, we note two observations from our work that may point to slower phase separation kinetics in LiMnPO_4 . Firstly, lower electronic conductivities arising from higher polaron migration barriers in the Mn olivine may impede phase transformation because both Li and electrons must diffuse to the site of transformation for phase transformation to occur. Secondly, the greater lattice mismatch between the delithiated and lithiated phases of the Mn olivine suggests that nucleation barriers in the the Mn olivine are likely to be higher than in the Fe olivine due to higher coherency strain at the phase transformation interface.

6.7 Successes and limitations of HSE06

Beyond the insights into the differences between the Mn and Fe olivines, our investigations also highlighted the successes and limitations of the HSE06 hybrid density functional versus conventional DFT based on GGA+ U . On one hand, the HSE06 functional was essential in achieving a proper localization of the polaron in the more strongly hybridized Mn olivine system where the GGA+ U was unable to achieve such

a localization. On the other, it failed to predicted even qualitatively correct formation energies for the Li_xFePO_4 . Our results suggest that while the HSE06 functional provides a more universal treatment of self-interaction over all atomic species, its treatment of electron correlation in strongly localized transition metal states such as those in the Fe olivine is still deficient. This deficiency is likely to be present in all hybrid functionals derived from PBE0 with a 0.25 fraction of exact exchange.

Despite this noted failure and significantly higher computational costs, we believe that the more universal approach to treating self-interaction offered by hybrid functionals such as HSE06 is important in capturing the essential physics of systems with strongly hybridized localized states that are not captured in current formulations of $\text{DFT}+U$. But our results also show that the hybrid functionals in their current state of development cannot be regarded as a panacea to self-interaction error correction, and in some systems, $\text{DFT}+U$ provides a better qualitative description.

6.8 Conclusion

In this work, we studied polaron migration and phase separation in olivine LiMnPO_4 and LiFePO_4 using hybrid density functional theory based on the HSE06 functional. The barriers for free hole and electron polaron migration in the Mn olivine system are 133 meV and 63 meV higher than that in the Fe olivine system respectively, suggesting 177 times slower electronic conduction in LiMnPO_4 and 11 times slower electronic conduction in MnPO_4 relative to the Fe analogues. In the presence of lithium vacancies or ions, the barriers for both hole and electron polaron migration were found to be around 100-120 meV higher in the Mn olivine. The HSE06 functional, with its more universal treatment of self-interaction error, was found to be essential to the proper localization of a polaron in the Mn olivine, but predicted qualitatively incorrect phase separation behavior in the Li_xFePO_4 system.

Chapter 7

Approximating the electrochemical windows of room-temperature ionic liquids

7.1 Room-temperature ionic liquids as potential electrolytes

In recent years, there has been a steadily growing interest in using room-temperature ionic liquids (ILs) as electrolytes in electrochemical applications such as supercapacitors [138, 139, 140] and rechargeable lithium batteries.[34, 35, 36, 37] ILs have several advantages over traditional organic electrolytes such as ethylene carbonate (EC) or dimethylcarbonate (DMC). They generally exhibit low volatility, low flammability and high thermal stability, which provides significant safety advantages over flammable organic compounds. This is particularly important in the application of Li-batteries beyond small-scale portable electronics to large-scale applications such as hybrid electric vehicles (HEVs) and electric vehicles. Many ILs also exhibit wide electrochemical windows of approximately 5-6 V or more[38], which are considerably larger than the 4.3-4.4 V electrochemical windows of current organic electrolytes in use. A more electrochemically stable electrolyte could unlock the potential of

high-voltage cathodes with higher power density. For example, LiNiPO_4 , which is predicted to have a potential near 5 V[23], would have 50% higher energy density than the Fe-based LiFePO_4 system currently under development for HEVs.

In electrochemical applications, the stability of the IL electrolyte against reduction (cathodic limit) and oxidation (anodic limit) is a key property of interest. In certain applications (e.g., supercapacitors), it is the electrochemical window, i.e., the difference between anodic and cathodic limits, that is of interest. In others, the electrolyte's stability relative to a particular electrode could be a limiting factor. For example, lithium at the graphitic node in rechargeable lithium batteries will reduce most organic solvents. Current organic electrolytes (e.g., EC/DMC with LiPF_6 added for Li^+ conductivity) work because of the formation of a passivating solid-electrolyte interphase (SEI) layer which prevents further electrolyte decomposition.[141]

Typically, the electrochemical window is determined experimentally by performing a linear sweep voltammetry using inert electrodes (e.g., Pt or Au) and measuring the cathodic and/or anodic currents, which are indicative of electrolyte reduction or oxidation. However, measured electrochemical windows depend heavily on the measurement conditions (e.g., type of electrode)[142] and also on the arbitrary current cut-off used to determine the onset of redox processes (typically between 0.1 and 1.0 mA cm^{-2}). Comparison of data from various experimental sources is made more difficult by the different references used, some of which may not be strictly electrochemically defined. In the case of ILs, this is further compounded by their sensitivity to water, air and other impurities.[143, 144, 145] For example, Randstrom et al.[144] have recently shown that while the innate cathodic stability of *pure and dry* ILs are generally set by the reduction potential of the cation, anion reduction[146] may occur at a higher potential than cation reduction in the presence of water and oxygen.

Koch *et al.*[147] demonstrated earlier that the experimentally measured electrochemical anodic stability of several ILs comprising 1,2-dimethyl-3-propylimidazolium cations paired with the PF_6 , AsF_6 , bis(trifluoromethylsulfonyl)imide (TFSI) and tris(trifluoromethylsulfonyl)methide anions correlates strongly with the highest occupied molecular orbital (HOMO) energies calculated using *ab initio* methods. In addi-

tion, there is also a significant body of work in the application of computational chemistry techniques to study redox potentials of conventional organic electrolytes[148, 149, 150] or the anions of lithium battery salts dissolved in these electrolytes.[151, 152] In particular, Ue *et al.*[151] examined the anodic stability of several anions used in Li-salt additives for Li-battery electrolytes, and found that experimental oxidation potentials are highly correlated with the HOMO energies and the ionization potentials calculated using density functional theory (DFT) and molecular orbital theories.

We investigated the trends in gas-phase electron affinities (EAs) of IL cations and ionization energies (IEs) of IL anions using computational chemistry methods.[6] The advent of efficient computational chemistry codes and inexpensive computing resources has made it possible to probe the large chemical space of IL ion structures in a systematic fashion to study how increasing “alkylation” and the substitution of electron-donating and electron-withdrawing functional groups affect the EA and IE of an ion. We will show that the qualitative trends obtained agree well with previous experimental and theoretical results, and suggest potential directions for IL design for electrochemical applications.

7.2 Systematic transversal of IL ion chemical space

Our investigative approach is to systematically traverse the IL ion chemical space to establish trends in the EAs and IEs. To this end, we have developed a simple substitution code to replace symmetrically-distinct terminal atoms in an IL ion structure (H for cations, and F for anions) with various functional groups (see Table 7.3) using optimized structure templates. This process can be repeated with new structures generated and in this manner, we can span the entire chemical space for a given set of basic ion structures and functional groups. In this work, we investigated how the calculated *gas-phase* EAs and IEs of common IL ions are affected by alkylation (the term “alkylation” is used loosely to refer to both alkyl group (C_nH_{2n+1}) substitutions on cations and fluoroalkyl group (C_nF_{2n+1}) substitutions on anions) and other functional group substitutions, as follows:

- To systematically probe the chemical space of alkylated ion structures, we started with an basic ion structure (e.g., simple ammonium cation, NH_4^+). Based on the point group symmetry of the ion (T_d in the case of NH_4^+), we substituted *symmetrically distinct* terminal atoms with methyl groups (trifluoromethyl, or CF_3 groups in the case of anions) to obtain a new set ion structures. Recursive substitutions result in increasing alkylation, allowing us to sample the complete space of alkylated ions. However, given that substitution tends to break symmetry, the number of structures rapidly become unmanageable. Hence, only the cation with the lowest computed EA or the anion with the highest computed IE was retained for the next stage of substitution, i.e., a “best-first” search algorithm with minimization of the EA or maximization of the IE as the objective function. While this could theoretically mean that we may miss possible cation structures with lower EAs or anion structures with higher IEs, in practice, there is usually more than one search path to the same structure and hence, we would expect most of the likely optimal structures to be found by our sampling method.
- A similar approach was used to investigate the effect of the different functional groups such as amine (NH_2), hydroxyl (OH), cyanide (CN), fluorine (F) and carboxyl (COOH) on a cation structure. Non-alkyl group investigations have been limited to single substitutions, and we have not explored recursive substitutions to obtain more complex ion structures.

We have focused on six cation and three anion structures commonly found in ILs (see Tables 7.1 and 7.2), and a mix of seven functional groups with known electron-donating (ED) and/or electron-withdrawing (EW) effects (see Table 7.3). ED groups tend to stabilize cations and destabilize anions while EW groups tend to stabilize anions and destabilize cations. Functional groups donate and withdraw electron density from a system through either inductive or resonance effects.[153] The inductive effect is related to the differences in electronegativity between elements, and transfer of electron density takes place primarily through σ bonds. Resonance effects refer

to the movement of electron density through delocalization effects, e.g., interaction between lone pairs and the π -bonding system in aromatic compounds.

Table 7.1: Cations investigated.

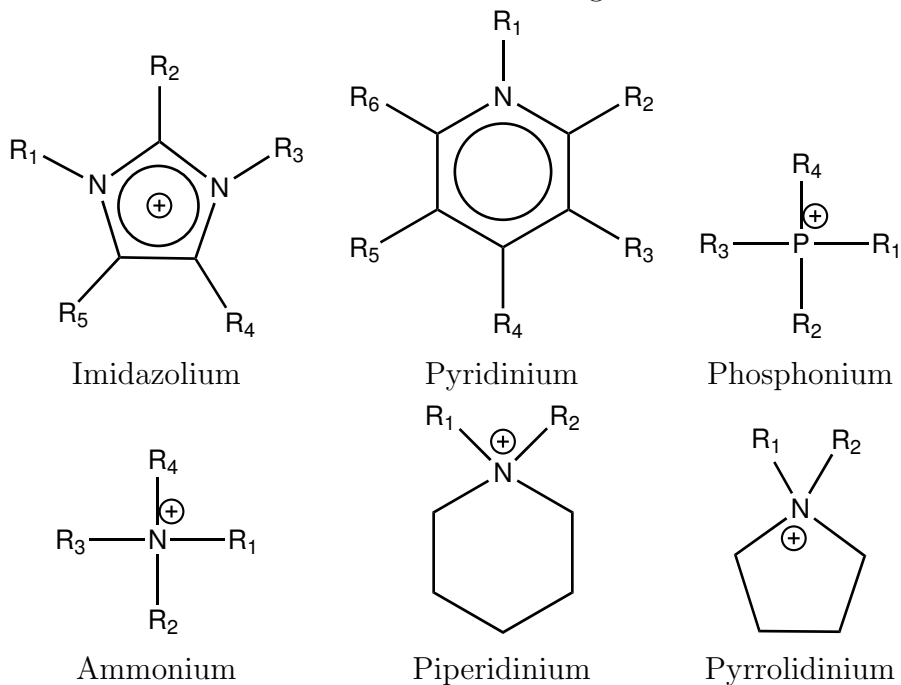
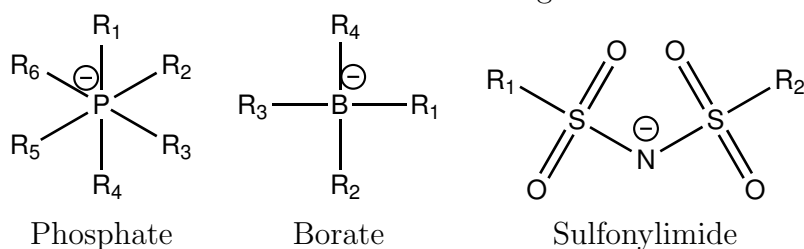


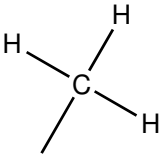
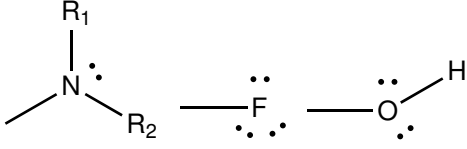
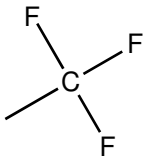
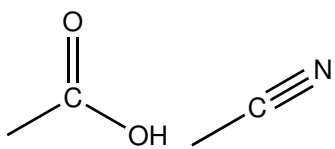
Table 7.2: Anions investigated.



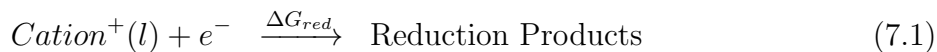
7.3 Proxy measure for electrochemical stability

In pure ILs, the cathodic and anodic limits are typically set by the reduction potential of the cation, and the oxidation potential of the anion.[154, 38] In principle, the reduction potential of the cation, V_{red} , and oxidation potential of the anion, V_{ox} , in the liquid can be calculated from the free energy changes of the redox reactions, ΔG_{red}

Table 7.3: Functional groups investigated and their known electron-donating (ED) and electron-withdrawing (EW) effects.[153]

ED by Inductive Effect	EW through inductive effect ED through resonance effect
	
EW by Inductive Effect	EW by Resonance Effect
	

and ΔG_{ox} , as follows:



$$V_{red} = -\frac{\Delta G_{red}}{e} \quad (7.3)$$

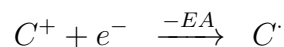
$$V_{ox} = \frac{\Delta G_{ox}}{e} \quad (7.4)$$

where all voltages are measured in volts and free energy changes are in electron-volts per ion. The resulting potential is with respect to the reference reaction that absorbs or donates the electron.

However, the redox decomposition products are in general not *a priori* known. While an exhaustive computational search can be done to find the most likely redox products,[155] such an approach is too expensive to be scaled to modeling hundreds of possible ion structures. Koch *et al.*[147] and Ue *et al.*[151] demonstrated the correlation between experimentally measured oxidation potentials and calculated HOMO energies of anions. We therefore have reason to postulate that the reduction and oxidation potentials of a pure IL to be correlated to the electron affinity (EA) of its cation and ionization energy (IE) of its anion respectively. The lower (higher) the EA (IE) of a cation (anion), the greater its intrinsic stability against reduction

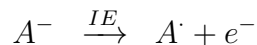
(oxidation).

The EA of a singly-charged cation, C, is defined as the energy released when an electron is added to a cation to form a neutral radical, i.e.,



It is well-established that calculated lowest unoccupied molecular orbital (LUMO) energies by time-independent quantum chemical methods are generally poor indicators of experimental EAs due to the poor description of virtual orbitals.[156] Hence, we have calculated the EA by explicitly taking the difference in energies between the cation and neutral radical. We calculated both the *vertical* EA, which is the energy difference between the cation and radical at the cation geometry, and the *adiabatic* EA, where both the cation and radical geometries were optimized.

Similarly, the ionization energy (IE) of a singly-charged anion, A, is defined as the energy needed to remove an electron from the anion to form a neutral radical, i.e.,



The anion IEs were calculated in a similar fashion to the cation EAs.

The gas-phase EA or IE is an intrinsic property of the isolated ion. It should be noted that this does not take into account possible chemical reactivity with electrode materials, and hence, trends in the calculated EAs and IEs should be compared with redox potentials measured using inert electrodes only. Possible chemical reactions with electrodes found in real-world electrochemical systems may lower the accessible electrochemical window significantly. Furthermore, gas-phase calculations do not take into account the effect that the local environment in the electrolyte has on the redox stability of the ion in the liquid state. While methods such as continuum solvation models and cluster approaches[157] can take into account local environment effects to varying degrees of approximation, these approaches either require additional input parameters such as the dielectric constant that are not available for all the ILs being explored, and/or are too computationally expensive for a high-throughput

investigation involving hundreds of different IL structures.

All calculations were performed using the Gaussian 03 quantum chemistry package.[158] Geometry optimizations were carried out at the B3LYP/6-31+G(d) level and were followed by single-point energy calculations at the B3LYP/6-311+G(2d,p) level. The hybrid B3LYP density functional based on Becke’s three-parameter exchange functional[92] and the correlation functional of Lee, Yang and Parr[159] was chosen as it has been shown to provide good accuracy for EAs and IEs at a reasonable computation cost. Curtiss *et al.*[160] found that the average absolute deviation of EAs and IEs of the G2 molecule test set predicted by B3LYP to be around 0.131 eV and 0.177 eV respectively. While compound methods (e.g., G3 theory[161]) and higher levels of ab initio molecular orbital theory (e.g., coupled cluster methods[162]) could potentially yield more accurate predictions, such methods are far too computationally expensive to be used to investigate hundreds of ions. The accuracy in EAs and IEs predicted by B3LYP is sufficient for the establishment of qualitative trends, though we do not expect to achieve quantitatively accurate results given the various approximations inherent in our approach. The inclusion of diffuse functions in the basis sets was also deliberate to ensure an adequate description of the diffuse electron cloud of anions, as well as the radicals formed from cation reduction. Close-shell restricted wave function calculations were used in the treatment of the cations and anions, while unrestricted open-shell wavefunctions were used for the radicals which have singly occupied orbitals. Frequency analysis was performed to ensure that structures obtained were minimum energy structures rather than transition structures, and also to obtain the thermochemical corrections for the Gibbs Free Energy, which were then scaled using the factor of 0.9806 determined earlier by Scott *et al.*[163] for the B3LYP/6-31G(d) model chemistry.

7.4 Geometry relaxation of cations and anions upon reduction and oxidation

For alkylated IL ion structures, we investigated approximately 170 unique cation and 30 unique anion structures.

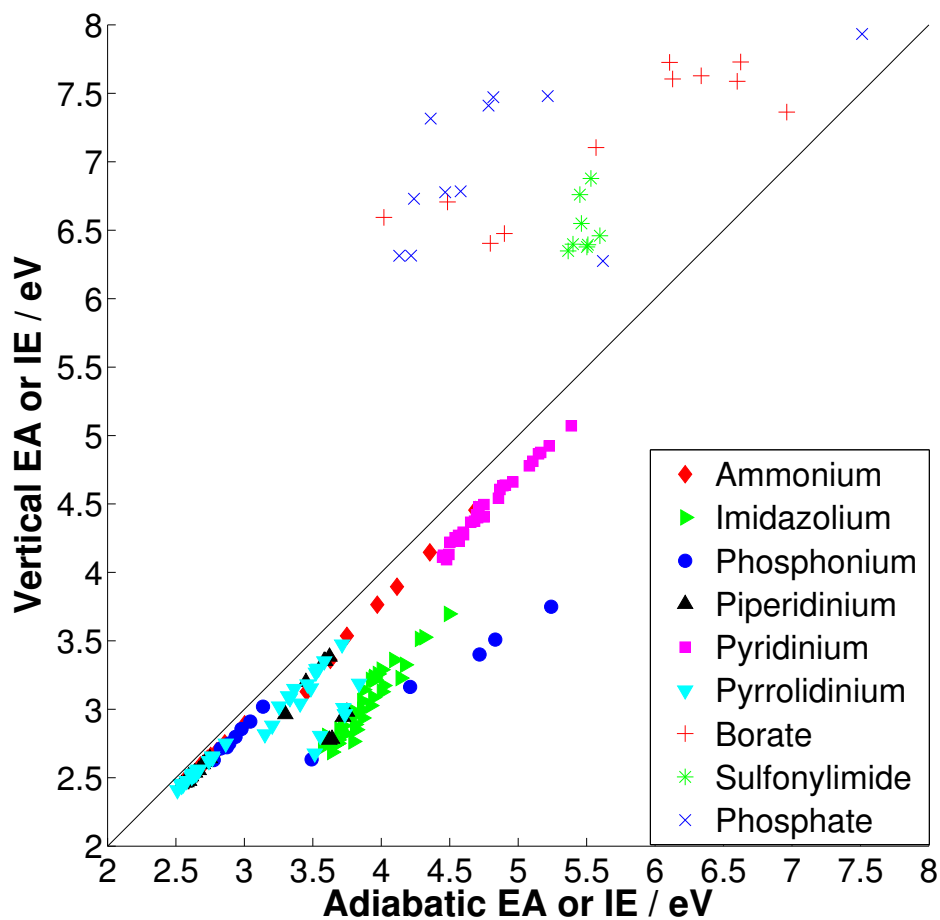


Figure 7-1: Plot of the calculated vertical EAs against calculated adiabatic EAs for alkylated IL cations, and calculated vertical IEs against calculated adiabatic IEs for alkylated IL anions.

Figure 7-1 shows a composite plot of the calculated vertical EAs against adiabatic EAs of alkylated IL cations, and the calculated vertical IEs against adiabatic IEs of alkylated IL anions. Six cation structures and one anion structure for which an opti-

mized radical structure could not be found are excluded, but these do not materially affect the trends obtained. The relaxation from geometry optimization means that adiabatic EAs > vertical EAs and adiabatic IEs < vertical IEs. In general, we find that the vertical and adiabatic EAs are fairly similar for most of the cations. However, we may observe that imidazolium cations appear to undergo a greater degree of geometrical relaxation upon reduction than other ions, as well as some of the smaller phosphonium, pyrrolidinium and piperidinium cations. For the anions, most appear to undergo significant geometry relaxation upon oxidation.

The neutral geometry-optimized radical is typically a reaction intermediate, and not the final product of the redox reaction. For instance, Kroon *et al.*[155] had investigated various reduction reaction paths for the 1,1-butylmethylpyrrolidinium and 1-butyl-3-methylimidazolium cations where radicals undergo decomposition into neutral fragments and smaller more stable radicals, react to form neutral molecules, or combine with one of the electrons of the π -bond to form a larger radical. They then verified that the predicted reduction products are indeed found experimentally. For the purposes of our work, though we would expect the adiabatic EA (IE) to be closer to the true reduction (oxidation) potential of the cation (anion), there is no way to *a priori* determine how far the neutral radical is to the final redox products energetically, which renders a comparison of the adiabatic EAs or IEs unreliable. Furthermore, there is also the practical issue that for some ions, a neutral geometry-optimized radical simply could not be obtained by adding or subtracting an electron to the ion. We have therefore chosen to look at the trends in the vertical EAs and IEs, which is indicative of how susceptible a cation (anion) is to accepting (donating) an electron, absent of geometrical relaxation effects.

7.5 Effect of alkylation on EAs of cations

In Figure 7-2, the calculated vertical EAs of alkylated cations are plotted against the molecular weight of the ion. Increasing molecular weight represents increasing alkylation. From the figure, we may make the following observations:

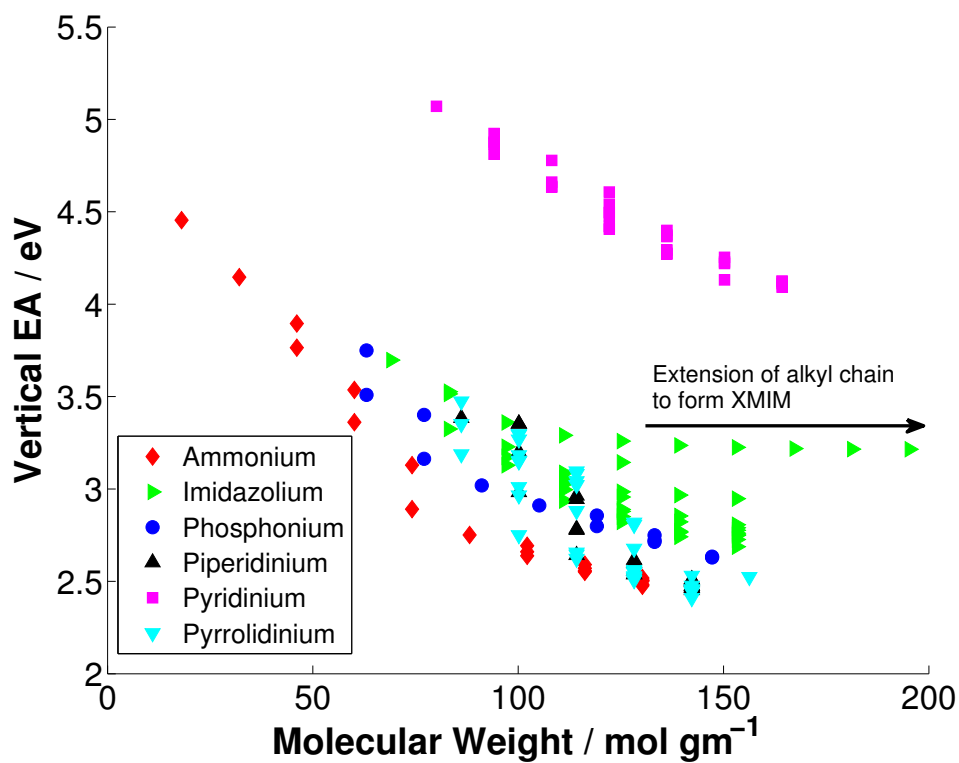


Figure 7-2: Effect of Increasing Alkylation on Vertical EA of IL Cations. XMIM refers to the 1-alkyl-3-methylimidazolium cation, where X ranges from ethyl (2 carbon atoms) to octyl (8 carbon atoms).

- In general, the EAs of alkylated ammonium, pyrrolidinium and phosphonium cations are lower than those of imidazolium and pyridinium ions. This is consistent with experimental evidence that ILs containing these aliphatic cations are in general more stable against reduction as compared to ILs containing the aromatic cations.[164, 165] Our results also predict imidazolium-based cations to have better cathodic stability than pyridinium-base cations, which is consistent with a comparison of experimentally measured cathodic and anodic stabilities of several IL systems (corrected to a common ferrocene reference) compiled by Matsumoto.[166]
- Increasing alkylation leads to a lowering of the EA and greater stability against reduction. This is consistent with the fact that alkyl groups are electron-donating in nature and hence would tend to stabilize a cation against reduction. Fitchett *et al.*[143] had earlier investigated the effect of increasing alkyl side chain lengths on the electrochemical windows of 1-alkyl-3-methylimidazolium bis(perfluoroalkylsulfonyl)imide ILs and observed a widening of the electrochemical window with increasing alkyl-chain length. More recently, Appetecchi *et al.*[167] has shown that the cathodic limit potential of N-alkyl-N-methylpyrrolidinium TFSI ILs steadily increases from -3.73 to -3.89 V in going from a propyl to a heptyl side chain. Though Appetecchi *et al.* had attributed the increase in cathodic potential to the increasing shielding effect of the positively charged nitrogen in the pyrrolidinium ring with the length of the side chain, our calculations show that there is an intrinsic stabilization effect arising from an increase in the strength of the electron-donating effect from longer alkyl chains.
- The initial effect of alkylation on the EA is greater than subsequent alkylation. This may be explained by the fact that the initial alkylation typically takes place at hydrogens connected to the aromatic ring structure (in the case of imidazolium or pyridinium based ions) or the atom of formal positive charge (e.g., N atom in ammonium-based cations), and hence result in a greater decrease in the EA. The effect is especially pronounced when comparing the EAs of the

XMIM cations against another imidazolium cation alkylated at the ring with the same molecular weight, i.e., the minimum EA structures at each molecular weight. Extending the alkyl side chain results in a very small decrease in the EA, while alkylation at the ring results in a much greater decrease.

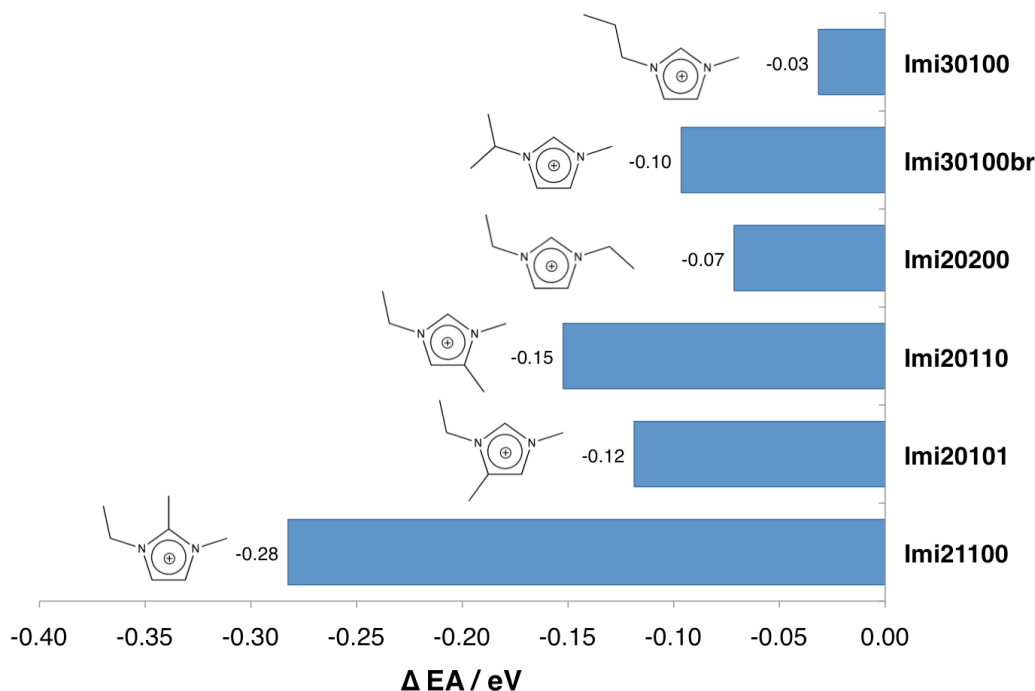


Figure 7-3: Effect of alkylation on the EA of 1-ethyl-3-methylimidazolium (EMIM) cation. The naming convention is based on the length of the alkyl chain attached to each ring atom, starting from the leftmost N atom and going around in a clockwise direction. Hence, Imi20100 \equiv EMI cation, Imi21100 \equiv 1-ethyl-2,3-dimethylimidazolium, etc. Imi30100 refers to the cation having an n-propyl group attached to the leftmost N atom, while Imi30100br refers to having an isopropyl group attached at the leftmost N atom.

We have also looked at how the EA of the 1-ethyl-3-methylimidazolium (EMIM) cation is modified by alkylation at the various positions (see Figure 7-3). Bonhote *et al.*[168] had earlier demonstrated that the 1-ethyl-2,3-dimethylimidazolium TFSI IL exhibits a much wider electrochemical windows than EMIM TFSI. The results from our calculations show that the greatest decrease in the EA of the EMI cation does indeed come from alkylation at the C(2) position. Again, we observe that substitution at the ring positions (Imi21100, Imi20110 and Imi20101 in Figure 7-3) results in a

greater lowering of the EA than an extension of an existing alkyl chain (Imi20200 and Imi30100).

7.6 Effect of alkylation on IEs of anions

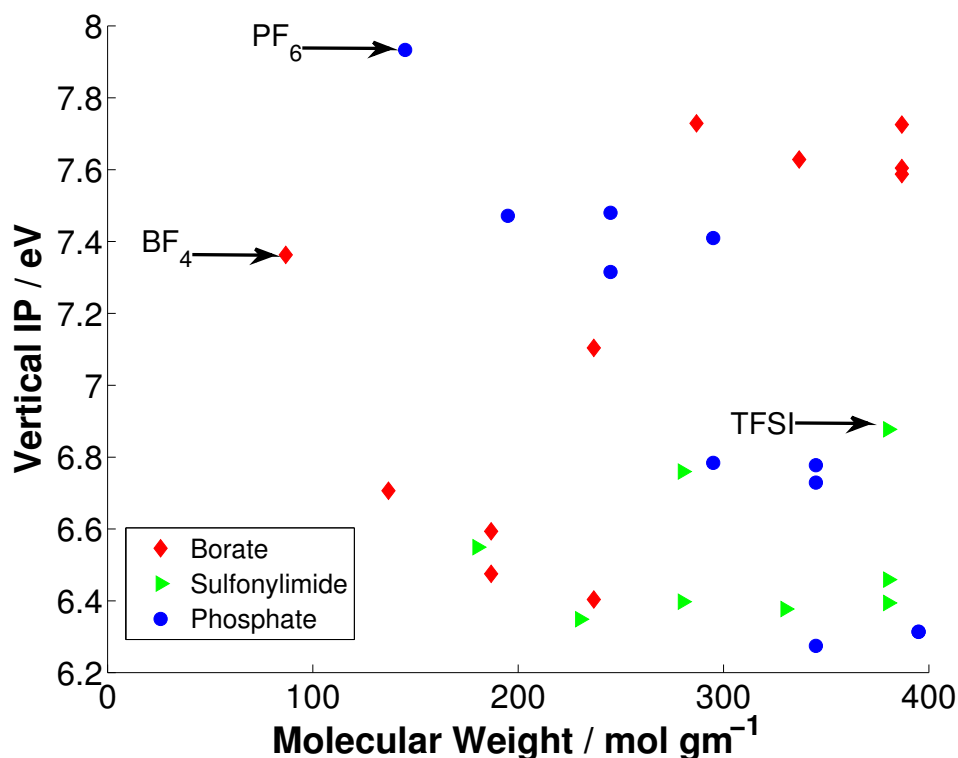


Figure 7-4: Effect of increasing alkylation on vertical IP of IL anions.

Figure 7-4 shows a similar plot of the calculated vertical IEs of alkylated anions against the molecular weight of the ion. From the figure, we may make the following observations:

- Our results predict the relative stabilities of the common IL anions, PF₆, BF₄ and bis(trifluoromethylsulfonyl)imide (TFSI) to be PF₆ > BF₄ > TFSI. This is consistent with the *ab initio* calculations and experimental measurements by Ue *et al.*[151], though it is inconsistent with earlier results of Koch *et al.*[147]
- Unlike the monotonically decreasing trend of EAs with increasing alkylation for cations, no monotonic increasing trend in IE with increasing molecular weight

is observed in the case of anions for the range of molecular weights considered. This could be explained by the fact that current IL anions are already based on fluorinated organic and inorganic ions. Fluorine is the most electronegative element and hence, would already have a great inductive stabilization effect on the anions. Initial substitution of fluorine with CF_3 groups therefore do not result in significantly increased stabilization. However, subsequent alkylation does appear to yield some additional stability in some instances, e.g., in the case of BF_4 and fluorosulfonylimide anions, within the range of molecular weights explored. The decreasing trend of IE with increasing alkylation for PF_6 could possibly be due to steric hindrance effects.

7.7 Effect of functional group substitutions

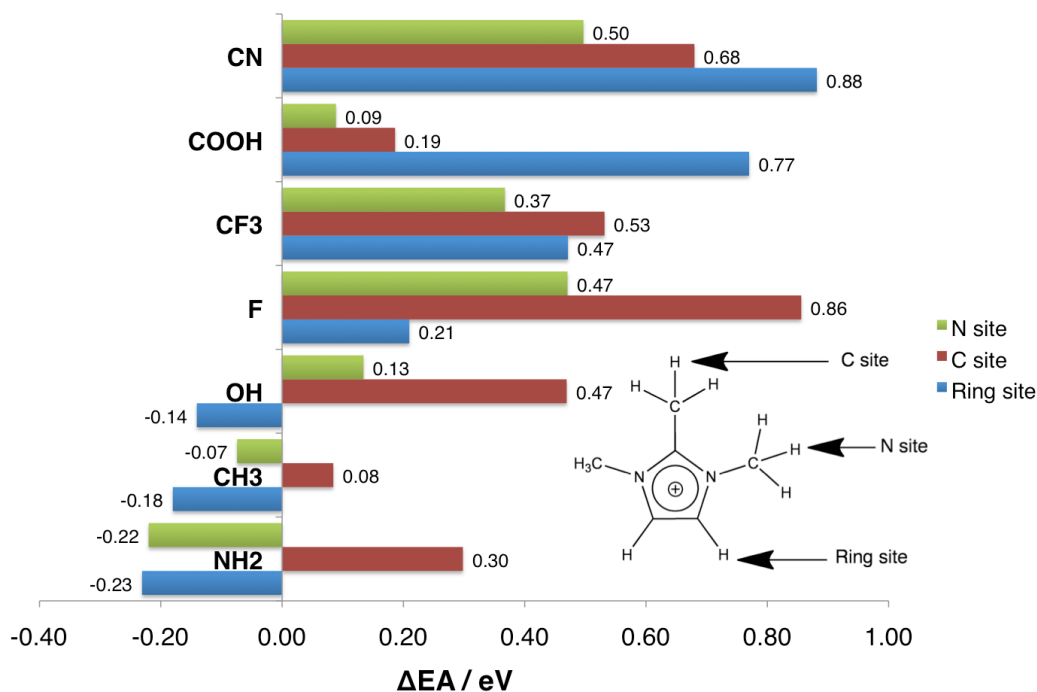


Figure 7-5: Effect of functional group substitutions on EA of 1,2,3-trimethylimidazolium (TMIM). The change in EA from the TMI cation is plotted, i.e., difference in EA between the functionalized cation and the non-functionalized cation.

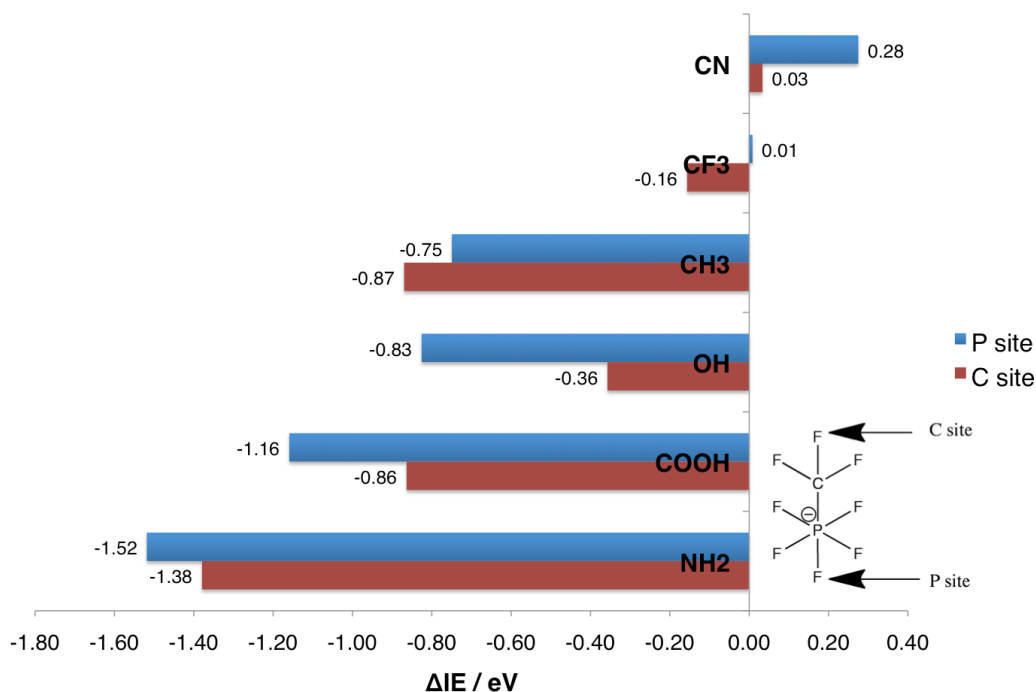


Figure 7-6: Effect of functional group substitutions on IE of PF_5CF_3 . The change in IE from the PF_5CF_3 anion is plotted, i.e., difference in IE between the functionalized anion and the non-functionalized anion.

We have investigated the effect of functional group substitutions on a few cation and anion structures. Figures 7-5 and 7-6 are representative plots showing the effect of different functional group substitutions on the EA of the 1,2,3-trimethylimidazolium (TMIM) cation and the IE of the PF_5CF_3 anion respectively. We have selected these ions as there are several distinct kinds of sites where substitution can be performed, which would provide additional insight on how the position of substitution affects the type and strength of the effect observed. For the TMIM cation, three distinct sites can be identified, namely a hydrogen attached to the imidazolium ring (“Ring site”), a hydrogen on the methyl group attached to a nitrogen atom (“N site”), or a hydrogen on the methyl group attached to the carbon atom between the two nitrogen atoms (“C site”). For the PF_5CF_3 anion, there are two distinct sites, namely a F atom directly attached to the P atom (“P site”), or an F atom attached to the existing CF_3 group (“C site”).

From the figures, we may make the following observations:

- As expected, electron-donating (ED) groups such as alkyl, NH_2 and OH groups generally stabilize the cation (leads to lower EAs) and destabilize the anion (lower IEs) while electron-withdrawing (EW) groups such as halogen, cyanide and trifluoromethane groups destabilizes the cation (increases EA) and stabilizes the anion (increases IE).
- Functional groups donate or withdraw electrons through inductive and resonance effects. For some functional groups, these two effects are in competition. For instance, NH_2 and OH groups withdraw electrons inductively but donate electrons through resonance. The overall effect on the EA or IE thus depends on which effect is stronger. For these two groups, we may note that the decrease in EA of the TMIM cation follows the trend : Ring site > N site > C site. Substitution at a ring site results in a decrease in the EA, while substitution at the C site results in an increase in an EA. This could be explained by the fact that substitution at the ring site results in a direct electron donation from the lone pairs on these functional groups to the delocalized π orbitals in the imidazolium ring, and thus the ED resonance effect dominates over the EW inductive effect. When attached to the C site, the opposite is true and the inductive effect dominates. The same observation can be made for the functional groups which are EW by resonance such as CN and COOH . For these groups, the greatest increase in EA occurs when substitution occurs at the ring site.
- Similarly for the PF_5CF_3 anion, we may observe that the greatest increase in IE comes when a group with a strong EW resonance effect (e.g., CN) is attached directly to the P site, which is the site of formal negative charge, while the greatest decrease in IE comes when a group with a strong ED resonance effect (e.g., NH_2 or OH) is attached directly to the P site. Substitutions at the C site result in a significantly weaker effect.

7.8 IL design strategies

Our results have shown that trends in the vertical EAs and IEs calculated using DFT methods are in qualitative agreement with relative experimental redox stabilities of ILs formed from various cations and anions, and with the general observed trend of increased cathodic stability resulting from alkylation of cations. Attaching electron-donating (ED) functional groups such as alkyl and amine groups generally decreases the EA of the cation and IE of the anion, and hence increases the stability of the cation against reduction but decreases the stability of the anion against oxidation. The reverse is true for electron-withdrawing (EW) functional groups. A monotonic decreasing trend of cation EA with increasing alkylation was observed, while no apparent trend was observed for increasing alkylation of anions within the range of molecular weights explored. We have also demonstrated that the position of substitution is important in determining the strength of the ED or EW effects. Resonance effects are especially pronounced when the functional group is attached to an aromatic ring or the atom of formal positive/negative charge (e.g., N atom in NH_4^+ or P atom in PF_6^-).

Given that we find reasonable trends, computational chemistry techniques can contribute to a more focused development of ILs for electrochemical applications. ILs are highly customizable solvents, and current research into ILs has barely scratched the surface of the massive chemical space for IL structures. For instance, most current research on ILs for Li-battery electrolytes has been limited to traditional ILs formed from alkylated imidazolium and ammonium-based cations with the BF_4 , PF_6 and TFSI anions. One possible strategy for future IL Li-battery electrolyte development would be to functionalize existing cations with other ED groups to achieve better cathodic stability. On the anodic side, the potential for increasing the oxidation limit of anions appear to be more limited as current anions are already based on fluorinated organic and inorganic anions for which there is a strong inductive stabilization effect. Even so, our results suggest that the cyanide group could be an excellent candidate to functionalize anions. It should also be noted that the base ions and functional

groups explored in this work are by no means a comprehensive list, and there could be other ions and functional groups that provide better electrochemical stability.

In real-world electrochemical applications, the electrochemical stability is but one factor to be optimized in IL electrolytes. There are other important properties affecting electrochemical performance, most notably the ionic conductivity of the IL. Nonetheless, the insights gained from our high-throughput exercise will enable the more targeted design of ILs to satisfy the various requirements of a particular application. For instance, there is evidence that reducing the symmetry of the constituent ions generally leads to a lowering of the viscosity and increase in ionic conductivity of an IL.[169] A common approach to reduce the symmetry is to attach functional groups of different kinds or sizes to the ion. Hence, the trends obtained in our work could provide insights on which functional groups can be attached such that the electrochemical stability is improved as well, or at the very least, minimize any adverse impact on the electrochemical stability.

We should also point that out while the qualitative trends are consistent with experimental observations, gas-phase EA and IE calculations are insufficient to produce **quantitative predictions** of redox stability in real-world applications. By their very nature, gas-phase calculations ignore local environment effects present in the liquid, such as dielectric screening, the effect of the counter-ion and packing in the liquid state. Also, EAs and IEs are only approximate proxies for the redox stability, and possible chemical reactivity with real-world electrodes may significantly shrink the electrochemical window.

7.9 Conclusion

We have investigated the electron affinities and ionization energies of a large spectrum of cations and anions for ionic liquids using *ab initio* molecular orbital theory at the B3LYP/6-311+G(2d,p)//B3LYP/6-31+G(d) level. We found that the trends in calculated EAs and IEs of alkylated IL cations and anions compare well with observed experimental trends in relative cathodic and anodic stabilities of various

ILs. We also investigated the effect of functional group substitutions on the EA of the 1,2,3-trimethylimidazolium cation and IE of the PF_5CF_3 anion, and explained the effects in terms of the known electron-donating and electron-withdrawing inductive and resonance effects of the functional groups. It is our belief that the insights obtained from these trends could provide the basis for a more focused approach to IL design and customization for electrochemical applications.

Chapter 8

Conclusion

In this thesis, we have leveraged on first principles computational materials science techniques to advance our understanding of Li-ion battery technology. Two major components in a Li-ion battery were studied, namely the cathode and electrolyte. Simultaneous advances in both these areas are needed to increase the energy density and improve the safety of Li-ion batteries, which are two key design criteria as Li-ion batteries move beyond consumer applications to larger scale applications such as PHEV and HEVs.

1. The phase diagram of the technologically important Li-Fe-P-O was calculated as a function of oxidation conditions.[1] The oxygen grand potential phase diagram thus constructed have provided a better understanding of phase equilibria under typical experimental synthesis and investigation conditions. The predictions of the calculated diagram agrees well with previous experimental findings. The combined application of the phase diagrams and Ellingham diagram provides a means to more efficiently focus experimental efforts to optimize synthesis approaches for LiFePO_4 , and has indeed been applied to the development of a high-rate LiFePO_4 with highly conductive glassy impurity phases.
2. Expanding on the oxygen grand potential phase diagrams, we developed a means to predict the thermal stability of a material by determining the oxygen evolution as a function of oxygen chemical potential / temperature.[2] We applied this

technique specifically to compare the relative thermal stabilities of the delithiated MPO_4 olivines ($\text{M} = \text{Fe}, \text{Mn}, \text{Co}, \text{Ni}$). In agreement with previous experimental findings, delithiated FePO_4 was predicted to be the most thermally stable, while delithiated MPO_4 was found to be less stable. The delithiated high-voltage NiPO_4 and CoPO_4 were found to be the least stable, suggesting a correlation between voltage and thermal stability. This technique has been adapted as a design criteria for high-throughput materials search as part of the Materials Genome at the Massachusetts Institute of Technology.

3. We revisited the calculation of lithium intercalation potentials and oxide redox energies in the context of hybrid density functional theory based on the Heyd-Scuseria-Ernzerhof (HSE06)[3, 4] hybrid functional.[5] We found the HSE06 functional to be effective in treating the self-interaction error inherent in standard DFT approaches, and perform similarly to $\text{DFT}+U$ in the prediction of lithium intercalation potentials and oxide redox energies, albeit at a significantly higher computational cost than $\text{GGA}+U$. The advantage of hybrid functionals over $\text{GGA}+U$ is the lack of a species-specific U parameter and perhaps more importantly, a more universal treatment of the self-interaction error over all species and occupied states rather than specific atomic orbital projections on specific ions.
4. We investigated the polaron migration barriers and phase separation energies of LiMnPO_4 and LiFePO_4 using the HSE06 functional. We found that the more general treatment of self-interaction error by the HSE06 functional is necessary to properly localize charge carriers in LiMnPO_4 because of the more strongly hybridized Mn-O bonds in this material. The polaron migration barriers were found to be significantly higher in the Mn olivine as compared to the Fe olivine, and indicates approximately two orders of magnitude difference in conductivity between the two materials. This prediction is in agreement with previous experimental findings.
5. On the electrolyte front, we explored room-temperature ionic liquids (ILs) as po-

tential replacement electrolytes for Li-ion batteries.[6] ILs offer significant safety advantages over flammable organic compounds as they exhibit low volatility, low flammability and high thermal stability, with the added benefit that their larger electrochemical windows could unlock higher voltage cathodes currently under development. Specifically, we investigated the trends in gas-phase electron affinities (EAs) of IL cations and ionization energies (IEs) of IL anions by systematically transversing the IL ion chemical space using computational chemistry methods. Our results have shown that trends in the vertical EAs and IEs calculated using DFT methods are in qualitative agreement with relative experimental redox stabilities of ILs formed from various cations and anions, and with the general observed trend of increased cathodic stability resulting from alkylation of cations. We found that attaching electron-donating (ED) functional groups such as alkyl and amine groups generally decreases the EA of the cation and IE of the anion, and hence increases the stability of the cation against reduction but decreases the stability of the anion against oxidation. The reverse is true for electron-withdrawing (EW) functional groups. A monotonic decreasing trend of cation EA with increasing alkylation was observed, while no apparent trend was observed for increasing alkylation of anions within the range of molecular weights explored. We have also demonstrated that the position of substitution is important in determining the strength of the ED or EW effects. Resonance effects are especially pronounced when the functional group is attached to an aromatic ring or the atom of formal positive/negative charge (e.g., N atom in NH_4^+ or P atom in PF_6^-). These qualitative trends agree well with previous experimental and theoretical results.

The work in this thesis has highlighted some of the challenges in the development of lithium batteries with higher power and higher energy density. Prima facie, it would appear that the correlation between high voltage and low thermal stability does not bode well for the development of high voltage cathode materials. Our investigation of polaron migrations barriers indicate that besides the issue of thermal stability, LiMnPO_4 , the olivine material that is arguably the most promising immediate step up

from LiFePO_4 , also suffers from poor electronic conductivity and intrinsically poorer kinetics. Also, while ILs show great promise as safer, higher voltage electrolytes for lithium batteries, our calculations suggest that there is less scope for improvement in the anodic limit based on current anion forms. Furthermore, their typically higher viscosity and lower ionic conductivity over conventional organic electrolytes are other major impediments to their widespread adoption in Li-ion batteries.

Nonetheless, there is still much cause for optimism in the future development of Li-ion battery technology.

The olivine phosphates are but one class of materials, and there is still a huge chemical space that is being explored through the Materials Genome project. Preliminary results have indicated that while the correlation between high voltage and low thermal stability holds in general, there are many outlier compounds and chemical systems (e.g., silicates) that offer both high voltage and reasonable predicted thermal stabilities. Some of these compounds are currently undergoing experimental synthesis and verification of the predicted properties.

The advent of hybrid functionals tailored for solid-state applications such as HSE06 has provided us with an additional computational investigative tool. While significantly more computationally expensive than standard semi-local DFT functionals, hybrid functionals are able to treat the self-interaction error in a more general manner, which may be essential in the investigation of certain properties (e.g., polaron migration) in more strongly hybridized systems. Also, the issue of computational cost will be mitigated with advances in computational power and code development.

On the electrolyte front, there are also other electrolyte systems, such as fluorinated organic solvents, under investigation, which can potentially offer larger electrochemical windows while retaining the advantages of current organic electrolytes of high ionic conductivities and low cost. The screening framework for IL ions in this thesis can be extended for the computational screening of functionalized organic solvents. On a broader front, the screening framework can be potentially developed into a molecular parallel to the Materials Genome project, which in its present form focuses mainly on extended solid state systems.

Appendix A

Calculated magnetic moments of Li_xMPO_4

Table A.1: Calculated magnetic moments on each Fe ion in the unit cell of Li_xFePO_4 for the various functionals.

x	Functional	Fe1	Fe2	Fe3	Fe4
0	GGA	3.914	-3.914	-3.914	3.914
	GGA+ U	4.254	-4.254	-4.254	4.254
	HSE06	4.220	-4.220	-4.220	4.220
0.25	GGA	3.931	-3.737	-3.732	3.929
	GGA+ U	4.240	-4.238	-3.718	4.251
	HSE06	4.215	-4.124	-3.846	4.220
0.5	GGA	3.892	-3.289	-3.336	3.893
	GGA+ U	4.251	-3.720	-3.720	4.251
	HSE06	4.220	-3.664	-3.664	4.220
0.75	GGA	3.766	-3.479	-3.478	3.756
	GGA+ U	4.229	-3.717	-3.732	3.731
	HSE06	4.114	-3.669	-3.676	3.852
1	GGA	3.534	-3.534	-3.535	3.534
	GGA+ U	3.732	-3.732	-3.732	3.732
	HSE06	3.677	-3.679	-3.681	3.677

Table A.2: Calculated magnetic moments on each Mn ion in the unit cell of Li_xMnPO_4 for the various functionals.

x	Functional	TM1	TM2	TM3	TM4
0	GGA	3.552	-3.552	-3.552	3.552
	GGA+ U	3.903	-3.903	-3.902	3.902
	HSE06	3.715	-3.715	-3.715	3.715
0.25	GGA	3.542	-3.967	-3.994	3.542
	GGA+ U	3.920	-4.275	-4.393	3.911
	HSE06	3.723	-3.739	-4.535	3.695
0.5	GGA	4.002	-3.995	-3.995	4.005
	GGA+ U	4.000	-4.596	-4.596	4.000
	HSE06	3.717	-4.554	-4.554	3.717
0.75	GGA	3.856	-4.421	-4.432	4.142
	GGA+ U	4.083	-4.635	-4.638	4.569
	HSE06	3.750	-4.555	-4.564	4.549
1	GGA	4.441	-4.441	-4.441	4.441
	GGA+ U	4.637	-4.637	-4.637	4.637
	HSE06	4.562	-4.562	-4.562	4.562

Bibliography

- [1] Shyue Ping Ong, Lei Wang, Byoungwoo Kang, and Gerbrand Ceder. Li-Fe-P-O₂ Phase Diagram from First Principles Calculations. *Chemistry of Materials*, 20:1798–1807, March 2008.
- [2] Shyue Ping Ong, Anubhav Jain, Geoffroy Hautier, Byoungwoo Kang, and Gerbrand Ceder. Thermal stabilities of delithiated olivine MPO₄ (M=Fe, Mn) cathodes investigated using first principles calculations. *Electrochemistry Communications*, 12(3):427–430, 2010.
- [3] Jochen Heyd, Gustavo E. Scuseria, and Matthias Ernzerhof. Hybrid functionals based on a screened Coulomb potential. *The Journal of Chemical Physics*, 118(18):8207, 2003.
- [4] Jochen Heyd, Gustavo E. Scuseria, and Matthias Ernzerhof. Erratum: Hybrid functionals based on a screened Coulomb potential [J. Chem. Phys. 118, 8207 (2003)]. *The Journal of Chemical Physics*, 124(21):219906, 2006.
- [5] Vincent L. Chevrier, Shyue Ping Ong, Rickard Armiento, Maria K. Y. Chan, and Gerbrand Ceder. Hybrid density functional calculations of redox potentials and formation energies of transition metal compounds. *Physical Review B*, 82(7):075122, August 2010.
- [6] Shyue Ping Ong and Gerbrand Ceder. Investigation of the Effect of Functional Group Substitutions on the Gas-Phase Electron Affinities and Ionization Energies of Room-Temperature Ionic Liquids Ions using Density Functional Theory. *Electrochimica Acta*, 55(11):3804–3811, 2010.

- [7] M. Stanley Whittingham. Intercalation and lattice expansion in titanium disulfide. *The Journal of Chemical Physics*, 62(4):1588, September 1975.
- [8] K. Mizushima, P. C. Jones, P. J. Wiseman, and J. B. Goodenough. Li_xCoO_2 ($0 < x < 1$): A New Cathode Material for Batteries of High Energy Density. *Materials Research Bulletin*, 15(c):783–789, 1980.
- [9] AK Padhi, KS Nanjundaswamy, and JB Goodenough. Phospho-olivines as Positive-Electrode Materials for Rechargeable Lithium Batteries. *Journal of the Electrochemical Society*, 144(4):1188–1194, January 1997.
- [10] H Huang, S-C Yin, and LF Nazar. Approaching theoretical capacity of LiFePO_4 at room temperature at high rates. *Electrochemical and Solid-State Letters*, 4(10):A170–172, 2001.
- [11] J. Barker, M. Y. Saidi, and J. L. Swoyer. Lithium Iron(II) Phospho-olivines Prepared by a Novel Carbothermal Reduction Method. *Electrochemical and Solid-State Letters*, 6(3):A53, 2003.
- [12] Masao Yonemura, Atsuo Yamada, Yuki Takei, Noriyuki Sonoyama, and Ryoji Kanno. Comparative Kinetic Study of Olivine $\text{Li}_{x}\text{MPO}_{4}$ ($\text{M}=\text{Fe}, \text{Mn}$). *Journal of The Electrochemical Society*, 151(9):A1352, 2004.
- [13] Atsuo Yamada and Sai-Cheong Chung. Crystal Chemistry of the Olivine-Type $\text{Li}(\text{Mn}_{y}\text{Fe}_{1-y})\text{PO}_{4}$ and $(\text{Mn}_{y}\text{Fe}_{1-y})\text{PO}_{4}$ as Possible 4 V Cathode Materials for Lithium Batteries. *Journal of The Electrochemical Society*, 148(8):A960, 2001.
- [14] A Yamada, SC Chung, and K Hinokuma. Optimized LiFePO_4 for Lithium Battery Cathodes. *Journal of the Electrochemical Society*, 148(3):A224–229, 2001.
- [15] Atsuo Yamada, Yoshihiro Kudo, and Kuang-Yu Liu. Reaction Mechanism of the Olivine-Type $\text{Li}_{x}(\text{Mn}_{0.6}\text{Fe}_{0.4})\text{PO}_{4}$ ($0 < x < 1$). *Journal of The Electrochemical Society*, 148(7):A747–A754, July 2001.

- [16] Atsuo Yamada, Yoshihiro Kudo, and Kuang-Yu Liu. Phase Diagram of $\text{Li}_x(\text{Mn}_y\text{Fe}_{1-y})\text{PO}_4$ ($0 < x, y < 1$). *Journal of The Electrochemical Society*, 148(10):A1153, 2001.
- [17] Natalia N. Bramnik, Kirill G. Bramnik, Thorsten Buhrmester, Carsten Baetz, Helmut Ehrenberg, and Hartmut Fuess. Electrochemical and structural study of LiCoPO_4 -based electrodes. *Journal of Solid State Electrochemistry*, 8(8):558–564, 2004.
- [18] K Amine, H Yasuda, and M Yamachi. Olivine LiCoPO_4 as 4.8 V Electrode Material for Lithium Batteries. *In Situ*, 3(4):178–179, 2000.
- [19] Sung-Yoon Chung, Jason T Bloking, and Yet-Ming Chiang. Electronically conductive phospho-olivines as lithium storage electrodes. *Nature materials*, 1(2):123–8, October 2002.
- [20] PS Herle, B Ellis, N Coombs, and LF Nazar. Nano-network electronic conduction in iron and nickel olivine phosphates. *Nature materials*, 3(3):147–52, March 2004.
- [21] Y Rho, L Nazar, L Perry, and D Ryan. Surface Chemistry of LiFePO_4 studied by Mossbauer and X-ray Photoelectron Spectroscopy and Its Effect on Electrochemical Properties. *J. Electrochem. Soc.*, 4:A283–A289, 2007.
- [22] B. Ellis, P. Subramanya Herle, Y.-H. Rho, L. F. Nazar, R. Dunlap, Laura K. Perry, and D. H. Ryan. Nanostructured materials for lithium-ion batteries: Surface conductivity vs. bulk ion/electron transport. *Faraday Discussions*, 134:119, 2007.
- [23] F Zhou, M Cococcioni, K Kang, and G Ceder. The Li intercalation potential of LiMPO_4 and LiMSiO_4 olivines with $M = \text{Fe, Mn, Co, Ni}$. *Electrochem. Commun.*, 6:1144–1148, 2004.

- [24] Guohua Li, Hideto Azuma, and Masayuki Tohda. LiMnPO₄ as the Cathode for Lithium Batteries. *Electrochemical and Solid-State Letters*, 5(6):A135, 2002.
- [25] C. Delacourt, L. Laffont, R. Bouchet, C. Wurm, J.-B. Leriche, M. Morcrette, J.-M. Tarascon, and C. Masquelier. Toward Understanding of Electrical Limitations (Electronic, Ionic) in LiMPO₄ (M=Fe, Mn) Electrode Materials. *Journal of The Electrochemical Society*, 152(5):A913, 2005.
- [26] L. Wang, F. Zhou, and G. Ceder. Ab Initio Study of the Surface Properties and Nanoscale Effects of LiMnPO₄. *Electrochemical and Solid-State Letters*, 11(6):A94, 2008.
- [27] N. Meethong, H.-Y.S. Huang, S.a. Speakman, W.C. Carter, and Y.-M. Chiang. Strain Accommodation during Phase Transformations in Olivine-Based Cathodes as a Materials Selection Criterion for High-Power Rechargeable Batteries. *Advanced Functional Materials*, 17(7):1115–1123, 2007.
- [28] Sung-Wook Kim, Jongsoon Kim, Hyeokjo Gwon, and Kisuk Kang. Phase Stability Study of Li_{1-x}MnPO₄ (0<x<1) Cathode for Li Rechargeable Battery. *Journal of The Electrochemical Society*, 156(8):A635, 2009.
- [29] Guoying Chen and Thomas J. Richardson. Thermal instability of Olivine-type LiMnPO₄ cathodes. *Journal of Power Sources*, 195(4):1221–1224, February 2010.
- [30] Charles Delacourt, Philippe Poizot, Jean-Marie Tarascon, and Christian Masquelier. The existence of a temperature-driven solid solution in Li_xFePO₄ for 0 < x < 1. *Nature Materials*, 4(3):254–260, February 2005.
- [31] Natalia N. Bramnik, Kristian Nikolowski, Dmytro M. Trots, and Helmut Ehrenberg. Thermal Stability of LiCoPO₄ Cathodes. *Electrochemical and Solid-State Letters*, 11(6):A89, 2008.

- [32] Deyu Wang, Jie Xiao, Wu Xu, and Ji-Guang Zhang. Investigation of LiNiPO₄ as a Cathode Material for Lithium Ion Battery. In *International Meeting on Lithium Batteries 2010*, 2010.
- [33] Kang Xu. Nonaqueous Liquid Electrolytes for Lithium-Based Rechargeable Batteries. *Chemical Reviews*, 104(10):4303–4418, October 2004.
- [34] B Garcia, S Lavallée, G Perron, C Michot, and M Armand. Room temperature molten salts as lithium battery electrolyte. *Electrochimica Acta*, 49:4583–4588, 2004.
- [35] H Matsumoto, T Matsuda, and Y Miyazaki. Room Temperature Molten Salts Based on Trialkylsulfonium Cations and Bis(trifluoromethylsulfonyl)imide. *Chemistry Letters*, pages 1430–1431, 2000.
- [36] H Nakagawa, S Izuchi, K Kuwana, T Nukuda, and Y Aihara. Liquid and Polymer Gel Electrolytes for Lithium Batteries Composed of Room-Temperature Molten Salt Doped by Lithium Salt. *J. Electrochem. Soc.*, 150:A695—A700, 2003.
- [37] Hikari Sakaebe, Hajime Matsumoto, and Kuniaki Tatsumi. Application of room temperature ionic liquids to Li batteries. *Electrochimica Acta*, 53:1048–1054, 2007.
- [38] M Galinski, A Lewandowski, and I Stepniak. Ionic liquids as electrolytes. *Electrochim. Acta*, 51:5567–5580, 2006.
- [39] Draft Plug-In Hybrid Electric Vehicle R&D Plan, 2007.
- [40] J Dahn, E Fuller, M Obrovac, and U Vonsacken. Thermal stability of Li_xCoO₂, Li_xNiO₂ and λ-MnO₂ and consequences for the safety of Li-ion cells. *Solid State Ionics*, 69(3-4):265–270, August 1994.
- [41] S. K. Martha, B. Markovsky, J. Grinblat, Y. Gofer, O. Haik, E. Zinigrad, D. Aurbach, T. Drezen, D. Wang, G. Deghenghi, and I. Exnar. LiMnPO₄ [sub 4]

- as an Advanced Cathode Material for Rechargeable Lithium Batteries. *Journal of The Electrochemical Society*, 156(7):A541, 2009.
- [42] V I Anisimov, I V Solovyev, M A Korotin, M T Czyzyk, and G A Sawatzky. Density-Functional Theory And Nio Photoemission Spectra. *Phys. Rev. B*, 48:16929–16934, 1993.
- [43] V I Anisimov, J Zaanen, and O K Andersen. Band Theory And Mott Insulators - Hubbard-U Instead Of Stoner-I. *Phys. Rev. B*, 44:943–954, 1991.
- [44] A. I. Liechtenstein, V. I. Anisimov, and J. Zaanen. Density-functional theory and strong interactions: Orbital ordering in Mott-Hubbard insulators. *Physical Review B*, 52(8):R5467–R5470, August 1995.
- [45] Richard M. Martin. *Electronic Structure: Basic Theory and Practical Methods (Vol 1)*. Cambridge University Press, 2004.
- [46] L. Wang, T. Maxisch, and G. Ceder. A First-Principles Approach to Studying the Thermal Stability of Oxide Cathode Materials. *Chemistry of Materials*, 19(3):543–552, February 2007.
- [47] C. Bradford Barber, David P. Dobkin, and Hannu Huhdanpaa. The quick-hull algorithm for convex hulls. *ACM Transactions on Mathematical Software (TOMS)*, 22(4):469, 1996.
- [48] JM Sanchez and D de Fontaine. The fcc Ising model in cluster variation approximation. *Physical Review B*, 17(7):2926, 1978.
- [49] M Asta, R McCormack, and D de Fontaine. Theoretical-study of Alloy Phase-Stability in the Cd-Mg System. *Phys. Rev. B*, 48(2):748–766, 1993.
- [50] G D Garbulsky and G Ceder. Effect of Lattice-Vibrations on the Ordering Tendencies in Substitutional Binary-Alloys. *Phys. Rev. B*, 49:6327–6330, 1994.
- [51] G J Ackland. Calculation of free energies from ab initio calculation. *J. Phys.: Condens. Matter*, 14:2975–3000, 2002.

- [52] G Bergerhoff, R Hundt, R Sievers, and I D Brown. The Inorganic Crystal-Structure Database. *Journal of chemical information and computer sciences*, 23(2):66–69, 1983.
- [53] V I Anisimov, F Aryasetiawan, and A I Lichtenstein. First-principles calculations of the electronic structure and spectra of strongly correlated systems: The LDA+U method. *J. Phys.: Condens. Matter*, 9:767–808, 1997.
- [54] G Kresse and D Joubert. From ultrasoft pseudopotentials to the projector augmented-wave method. *Phys. Rev. B*, 59:1758–1775, 1999.
- [55] G Kresse and J Furthmuller. Efficient iterative schemes for ab initio total-energy calculations using a plane-wave basis set. *Phys. Rev. B*, 54:11169–11186, 1996.
- [56] R L Wang and J R Dahn. Computational estimates of stability of redox shuttle additives for Li-ion cells. *J. Electrochem. Soc.*, 153:A1922—A1928, 2006.
- [57] S L Dudarev, G A Botton, S Y Savrasov, C J Humphreys, and A P Sutton. Electron-energy-loss spectra and the structural stability of nickel oxide: An LSDA+U study. *Physical Review B*, 57(3):1505–1509, 1998.
- [58] Matteo Cococcioni and Stefano de Gironcoli. Linear response approach to the calculation of the effective interaction parameters in the LDA+U method. *Physical Review B*, 71(3):1–16, January 2005.
- [59] Lei Wang, Thomas Maxisch, and Gerbrand Ceder. Oxidation energies of transition metal oxides within the GGA+U framework. *Physical Review B*, 73(19):1–6, 2006.
- [60] O. Kubaschewski, C. B. Alcock, and P. J. Spencer. *Thermochemical Data*, chapter 5, page 376. Butterworth-Heinemann, sixth edition, 1993.
- [61] Geoffroy Hautier, Christopher C Fischer, Anubhav Jain, Tim Mueller, and Gerbrand Ceder. Finding Natures Missing Ternary Oxide Compounds Using

- Machine Learning and Density Functional Theory. *Chemistry of Materials*, (20):641–646, 2010.
- [62] C Delacourt, C Wurm, L Laffont, J Leriche, and C Masquelier. Electrochemical and electrical properties of Nb- and/or C-containing LiFePO₄ composites. *Solid State Ionics*, 177(3-4):333–341, January 2006.
- [63] R K Osterheld. Liquidus Diagram For System Lithium Orthophosphate-Lithium Metaphosphate. *J. Inorg. Nucl. Chem.*, 30(12):3173–3174, 1968.
- [64] V Raghavan. *Phase Diagrams of Binary Iron Alloys*. Indian Institute of Metals, 1989.
- [65] A Modaresi, JC Kaell, B Malaman, R Gerardin, and C Gleitzer. Etude Du Systeme Fe-P-O (Pour Fe/P) 1) Et D’une Famille : Les Oxyphosphates De Fer. *Mat. Res. Bull.*, 18:101–109, 1983.
- [66] Hiroaki Okamoto. *Handbook of Ternary Alloy Phase Diagrams*. ASM International(OH), 1995.
- [67] H Okamoto. *Phase Diagrams of Binary Iron Alloys*. ASM International, 1993.
- [68] J. Sangster, a. D. Pelton, and H. Okamoto. The Li-P (lithium-phosphorus) system. *Journal of Phase Equilibria*, 16(1):92–93, February 1995.
- [69] R Juza and K Langer. Ternary Lithium Phosphides and Arsenides with Iron Cobalt or Chromium of Cu₂Sb Type. *Zeitschrift Fur Anorganische Und Allgemeine Chemie*, 361(1-2):58, 1968.
- [70] S. Boyanov, J. Bernardi, F. Gillot, L. Dupont, M. Womes, J.-M. Tarascon, L. Monconduit, and M.-L. Doublet. FeP: Another Attractive Anode for the Li-Ion Battery Enlisting a Reversible Two-Step Insertion/Conversion Process. *Chemistry of Materials*, 18(15):3531–3538, July 2006.
- [71] M. W. Chase. *NIST-JANAF Thermochemical Tables, Vol 12*. American Chemical Society, New York, 1998.

- [72] H J T Ellingham. Reducibility of oxides and sulfides in metallurgical processes. *J Soc Chem Ind (London)*, 63:125, 1944.
- [73] D Kim, H Park, S Jung, Y Jeong, J Lee, and J Kim. Effect of synthesis conditions on the properties of LiFePO₄ for secondary lithium batteries. *Journal of Power Sources*, 159(1):237–240, September 2006.
- [74] I Belharouak, C Johnson, and K Amine. Synthesis and electrochemical analysis of vapor-deposited carbon-coated LiFePO₄. *Electrochemistry Communications*, 7(10):983–988, October 2005.
- [75] B Kang and G Ceder. Battery materials for ultrafast charging and discharging. *Nature*, 458(March):190–193, 2009.
- [76] Byoungwoo Kang and Gerbrand Ceder. Electrochemical Performance of LiMnPO₄ Synthesized with Off-Stoichiometry. *Journal of The Electrochemical Society*, 157(7):A808, 2010.
- [77] J E Miller, M M Gonzales, L Evans, A G Sault, C Zhang, R Rao, G Whitwell, A Maiti, and D King-Smith. Oxidative dehydrogenation of ethane over iron phosphate catalysts. *Applied Catalysis A-General*, 231 (1-2):281–292, 2002.
- [78] P P Ewald. The calculation of optical and electrostatic grid potential. *Annalen der Physik*, 64(3):253–287, 1921.
- [79] A. Toukmaji and J. A. Board. Ewald summation techniques in perspective: A survey. *Computer Physics Communications*, 95(2-3):73–92, 1996.
- [80] Gus L. W. Hart and Rodney W. Forcade. Algorithm for generating derivative structures. *Physical Review B*, 77(22):1–12, 2008.
- [81] M. E. Arroyo Y De Dompablo, N. Biskup, J. M. Gallardo-Amores, E. Moran, H. Ehrenberg, and U. Amador. Gaining Insights into the Energetics of FePO₄ Polymorphs. *Chemistry of Materials*, 8(10):091109144106046, November 2009.

- [82] S. Yang, Y. Song, P Y Zavalij, and M S Whittingham. Reactivity, stability and electrochemical behavior of lithium iron phosphates. *Electrochemistry Communications*, 4:239–244, 2002.
- [83] G. Rouse, J. Rodriguez-Carvajal, S. Patoux, and C. Masquelier. Magnetic Structures of the Triphylite LiFePO_4 and of Its Delithiated Form FePO_4 . *Chemistry of Materials*, 15(21):4082–4090, October 2003.
- [84] H. L. Schläfer and G. Gliemann. *Basic Principles of Ligand Field Theory*. Wiley-Interscience, New York, 1969.
- [85] Robert A. Huggins. Do You REALLY Want a High Potential Cathode? *ECS Transactions*, 16(29):37–47, 2009.
- [86] J Cho. Correlation between AlPO_4 nanoparticle coating thickness on LiCoO_2 cathode and thermal stability. *Electrochimica Acta*, 48(19):2807–2811, August 2003.
- [87] Anjuli T. Appapillai, Azzam N. Mansour, Jaephil Cho, and Yang Shao-Horn. Microstructure of LiCoO_2 with and without AlPO_4 Nanoparticle Coating: Combined STEM and XPS Studies. *Chemistry of Materials*, 19(23):5748–5757, November 2007.
- [88] Kevin S. Raymond, Anthony K. Grafton, and Ralph A. Wheeler. Calculated One-Electron Reduction Potentials and Solvation Structures for Selected p - Benzoquinones in Water. *The Journal of Physical Chemistry B*, 101(4):623–631, January 1997.
- [89] Merle Uudsemaa and Toomas Tamm. Density-Functional Theory Calculations of Aqueous Redox Potentials of Fourth-Period Transition Metals. *The Journal of Physical Chemistry A*, 107(46):9997–10003, November 2003.
- [90] F. Zhou, M. Cococcioni, C. A. Marianetti, D. Morgan, and G. Ceder. First-principles prediction of redox potentials in transition-metal compounds with LDA+U. *Physical Review B*, 70:235121, December 2004.

- [91] Christopher J Cramer and Donald G Truhlar. Density functional theory for transition metals and transition metal chemistry. *Physical chemistry chemical physics : PCCP*, 11(46):10757–816, 2009.
- [92] A Becke. Density Functional Thermochemistry III The Role of Exact Exchange. *J. Chem. Phys.*, 98:5648–5652, April 1993.
- [93] Carlo Adamo and Vincenzo Barone. Toward reliable density functional methods without adjustable parameters: The PBE0 model. *The Journal of Chemical Physics*, 110(13):6158, 1999.
- [94] J Paier, M Marsman, K Hummer, G Kresse, I C Gerber, and J G Angyán. Screened hybrid density functionals applied to solids. *The Journal of chemical physics*, 124(15):154709, April 2006.
- [95] Xiao-Bing Feng and N. Harrison. Metal-insulator and magnetic transition of NiO at high pressures. *Physical Review B*, 69(3), January 2004.
- [96] M. Alfredsson, G. David Price, C. Catlow, S. Parker, R. Orlando, and J. Brodholt. Electronic structure of the antiferromagnetic B1-structured FeO. *Physical Review B*, 70(16), October 2004.
- [97] Fabien Tran, Peter Blaha, Karlheinz Schwarz, and Pavel Novák. Hybrid exchange-correlation energy functionals for strongly correlated electrons: Applications to transition-metal monoxides. *Physical Review B*, 74(15), October 2006.
- [98] John P. Perdew, Matthias Ernzerhof, and Kieron Burke. Rationale for mixing exact exchange with density functional approximations. *The Journal of Chemical Physics*, 105(22):9982, 1996.
- [99] M K Aydinol, A F Kohan, G Ceder, K Cho, and J Joannopoulos. Ab initio study of lithium intercalation in metal oxides and metal dichalcogenides. *Physical Review B*, 56(3):1354–1365, 1997.

- [100] C Delmas, C Fouassier, and P Hagemuller. Structural classification and properties of the layered oxides. *Physica B+C*, 99(1-4):81–85, January 1980.
- [101] G. G. Amatucci, J. M. Tarascon, and L. C. Klein. CoO₂, The End Member of the Li_xCoO₂ Solid Solution. *Journal of The Electrochemical Society*, 143(3):1114–1123, March 1996.
- [102] M. M. Thackeray. Structural Considerations of Layered and Spinel Lithiated Oxides for Lithium Ion Batteries. *Journal of The Electrochemical Society*, 142(8):2558–2563, August 1995.
- [103] C Delmas, M. Menetrier, L. Croguennec, S. Levasseur, J.P. Peres, C. Poullerie, G. Prado, L. Fournes, and F. Weill. Lithium batteries: a new tool in solid state chemistry. *International Journal of Inorganic Materials*, 1(1):11–19, April 1999.
- [104] C. Wolverton and Alex Zunger. Prediction of Li Intercalation and Battery Voltages in Layered vs. Cubic Li_xCoO₂. *Journal of The Electrochemical Society*, 145(7):2424–2431, July 1998.
- [105] J. Reed, G. Ceder, and A. Van Der Ven. Layered-to-Spinel Phase Transition in Li_xMnO₂. *Electrochemical and Solid-State Letters*, 4(6):A78, 2001.
- [106] A. Van der Ven and G. Ceder. Lithium Diffusion in Layered Li_xCoO₂. *Electrochemical and Solid-State Letters*, 3(7):301–304, July 2000.
- [107] M S Whittingham. Electrical energy storage and intercalation chemistry. *Science*, 192(4244):1126–7, June 1976.
- [108] K.M. Colbow, J.R. Dahn, and R.R. Haering. Structure and electrochemistry of the spinel oxides LiTi₂O₄ and LiTiO₄. *Journal of Power Sources*, 26(3-4):397–402, May 1989.
- [109] R. J. Cava, D. W. Murphy, S. Zahurak, A. Santoro, and R. S. Roth. The Crystal Structures of the Lithium-Inserted Metal Oxides Li_{0.5}TiO₂ Anatase,

- LiTi₂O₄ Spinel, and Li₂Ti₂O₄. *Journal of Solid State Chemistry*, 53(1):64–75, June 1984.
- [110] María Ángeles Monge, José Manuel Amarilla, Enrique Gutiérrez-Puebla, Juan Antonio Campa, and Isidoro Rasines. Atomic Level Study of LiMn₂O₄ as Electrode in Lithium Batteries. *ChemPhysChem*, 3(4):367–370, April 2002.
- [111] J. Rodríguez-Carvajal, G. Rousse, C. Masquelier, and M. Hervieu. Electronic Crystallization in a Lithium Battery Material: Columnar Ordering of Electrons and Holes in the Spinel LiMn₂O₄. *Physical Review Letters*, 81(21):4660–4663, November 1998.
- [112] J Wolfenstine and J Allen. Ni²⁺/Ni³⁺ redox potential in LiNiPO. *Journal of Power Sources*, 142(1-2):389–390, March 2005.
- [113] John P. Perdew, Kieron Burke, and Matthias Ernzerhof. Generalized Gradient Approximation Made Simple. *Physical Review Letters*, 77(18):3865–3868, October 1996.
- [114] B. Hammer, L. Hansen, and J. Nørskov. Improved adsorption energetics within density-functional theory using revised Perdew-Burke-Ernzerhof functionals. *Physical Review B*, 59(11):7413–7421, March 1999.
- [115] Koichi Momma and Fujio Izumi. *VESTA*: a three-dimensional visualization system for electronic and structural analysis. *Journal of Applied Crystallography*, 41(3):653–658, June 2008.
- [116] C A Marianetti, G Kotliar, and G Ceder. A first-order Mott transition in Li_xCoO₂. *Nature materials*, 3(9):627–31, September 2004.
- [117] P. Kuiper, G. Kruizinga, J. Ghijsen, G. Sawatzky, and H. Verweij. Character of Holes in Li_xNi_{1-x}O and Their Magnetic Behavior. *Physical Review Letters*, 62(2):221–224, January 1989.

- [118] J. van Elp, H. Eskes, P. Kuiper, and G. Sawatzky. Electronic structure of Li-doped NiO. *Physical Review B*, 45(4):1612–1622, January 1992.
- [119] W Mackrodt. Direct evidence of O(p) holes in Li-doped NiO from Hartree-Fock calculations. *Chemical Physics Letters*, 250(1):66–70, February 1996.
- [120] Jochen Heyd and Gustavo E Scuseria. Efficient hybrid density functional calculations in solids: assessment of the Heyd-Scuseria-Ernzerhof screened Coulomb hybrid functional. *The Journal of chemical physics*, 121(3):1187–92, July 2004.
- [121] H. Fröhlich. Electrons in lattice fields. *Advances in Physics*, 3(11):325–361, July 1954.
- [122] Thomas Maxisch, Fei Zhou, and Gerbrand Ceder. Ab initio study of the migration of small polarons in olivine Li_xFePO_4 and their association with lithium ions and vacancies. *Physical Review B*, 73(10):1–6, 2006.
- [123] K. Zaghbib, a. Mauger, J. B. Goodenough, F. Gendron, and C. M. Julien. Electronic, Optical, and Magnetic Properties of LiFePO_4 : Small Magnetic Polaron Effects. *Chemistry of Materials*, 19(15):3740–3747, July 2007.
- [124] Brian Ellis, Laura K Perry, Dominic H Ryan, and L F Nazar. Small polaron hopping in $\text{Li}(x)\text{FePO}_4$ solid solutions: coupled lithium-ion and electron mobility. *Journal of the American Chemical Society*, 128(35):11416–22, September 2006.
- [125] C. G. Kuper and G. D. Whitfield. *Polarons and Excitons*. 1962.
- [126] C. Franchini, G. Kresse, and R. Podloucky. Polaronic Hole Trapping in Doped BaBiO_3 . *Physical Review Letters*, 102(25):256402, June 2009.
- [127] C. Patterson. Small polarons and magnetic antiphase boundaries in $\text{Ca}_2\text{xNa}_x\text{CuO}_2\text{Cl}_2$ ($x=0.06,0.12$): Origin of striped phases in cuprates. *Physical Review B*, 77(9):094523, March 2008.

- [128] N Iordanova, M Dupuis, and K M Rosso. Theoretical characterization of charge transport in chromia (α -Cr₂O₃). *The Journal of chemical physics*, 123(7):074710, August 2005.
- [129] N Iordanova, M Dupuis, and K M Rosso. Charge transport in metal oxides: a theoretical study of hematite α -Fe₂O₃. *The Journal of chemical physics*, 122(14):144305, April 2005.
- [130] E. O. Wollan and W. C. Koehler. Neutron Diffraction Study of the Magnetic Properties of the Series of Perovskite-Type Compounds [(1-x)La, xCa]MnO₃. *Physical Review*, 100(2):545–563, 1955.
- [131] C. Marianetti, D. Morgan, and G. Ceder. First-principles investigation of the cooperative Jahn-Teller effect for octahedrally coordinated transition-metal ions. *Physical Review B*, 63(22), May 2001.
- [132] E. R. Ylvisaker, R. R. P. Singh, and W. E. Pickett. Orbital order, stacking defects, and spin fluctuations in the p -electron molecular solid RbO₂. *Physical Review B*, 81(18):180405, May 2010.
- [133] Dong-Hwa Seo, Hyeokjo Gwon, Sung-Wook Kim, Jongsoon Kim, and Kisuk Kang. Multicomponent Olivine Cathode for Lithium Rechargeable Batteries: A First-Principles Study. *Chemistry of Materials*, 7(9):091223161926007, 2009.
- [134] F Zhou, C A Marianetti, M Cococcioni, D Morgan, and G Ceder. Phase separation in Li_xFePO₄ induced by correlation effects. *Physical Review B*, 69:201101, May 2004.
- [135] Fei Zhou. *Models for transition metal oxides and for protein design*. Thesis, Massachusetts Institute of Technology, 2006.
- [136] Fei Zhou, Thomas Maxisch, and Gerbrand Ceder. Configurational Electronic Entropy and the Phase Diagram of Mixed-Valence Oxides: The Case of Li_xFePO₄. *Physical Review Letters*, 97(15):155704, October 2006.

- [137] Thierry Drezen, Nam-Hee Kwon, Paul Bowen, Ivo Teerlinck, Motoshi Isono, and Ivan Exnar. Effect of particle size on LiMnPO₄ cathodes. *Journal of Power Sources*, 174(2):949–953, December 2007.
- [138] A B McEwen, S F McDevitt, and V R Koch. Nonaqueous electrolytes for electrochemical capacitors: Imidazolium cations and inorganic fluorides with organic carbonates. *J. Electrochem. Soc.*, 144:L84–L86, April 1997.
- [139] A B McEwen, H L Ngo, K LeCompte, and J L Goldman. Electrochemical properties of imidazolium salt electrolytes for electrochemical capacitor applications. *J. Electrochem. Soc.*, 146:1687–1695, May 1999.
- [140] A Lewandowski and M Galinski. Carbon-ionic liquid double-layer capacitors. *J. Phys. Chem. Solids*, 65:281–286, 2004.
- [141] Z. X. Shu, R. S. McMillan, and J. J. Murray. Electrochemical Intercalation of Lithium into Graphite. *Journal of The Electrochemical Society*, 140(4):922, 1993.
- [142] Emma I. Rogers, Biljana Sljukic, Christopher Hardacre, and Richard G. Compton. Electrochemistry in Room-Temperature Ionic Liquids: Potential Windows at Mercury Electrodes. *Journal of Chemical & Engineering Data*, 54(7):2049–2053, July 2009.
- [143] BD Fitchett, JB Rollins, and JC Conboy. 1-Alkyl-3-methylimidazolium Bis(perfluoroalkylsulfonyl)imide Water-Immiscible Ionic Liquids. *Journal of the Electrochemical Society*, 151(7):E219–E225, 2004.
- [144] S Randström, M Montanino, GB Appetecchi, C Lagergrenb, A Morenoa, and S Passerini. Effect of water and oxygen traces on the cathodic stability of N-alkyl-N-methylpyrrolidinium bis(trifluoromethanesulfonyl)imide. *Electrochimica Acta*, 53:6397–6401, 2008.
- [145] Aoife M. OMahony, Debbie S. Silvester, Leigh Aldous, Christopher Hardacre, and Richard G. Compton. Effect of Water on the Electrochemical Window and

- Potential Limits of Room-Temperature Ionic Liquids. *Journal of Chemical and Engineering Data*, 53(12):2884–2891, December 2008.
- [146] Patrick C Howlett, Ekaterina I Izgorodina, Maria Forsyth, and Douglas R Macfarlane. Electrochemistry at negative potentials in bis(trifluoromethanesulfonyl)amide ionic liquids. *Zeitschrift fur Physikalische Chemie*, 220:1483–1498, 2006.
- [147] VR Koch, LA Dominey, and C Nanjundiah. The Intrinsic Anodic Stability of Several Anions Comprising Solvent-Free Ionic Liquids. *Journal of the Electrochemical Society*, 143:798–803, 1996.
- [148] J M Vollmer, L A Curtiss, D R Vissers, and K Amine. Reduction mechanisms of ethylene, propylene, and vinylene carbonates - A quantum chemical study. *J. Electrochem. Soc.*, 151(1):A178–A183, 2004.
- [149] Suojiang Zhang, Ning Sun, Xuezhong He, Xingmei Lu, and Xiangping Zhang. Physical Properties of Ionic Liquids: Database and Evaluation. *Green Chemistry*, 35(4):1475, 2006.
- [150] Ken Tasaki, Katsuya Kanda, Takao Kobayashi, Shinichiro Nakamura, and Makoto Ue. Theoretical Studies on the Reductive Decompositions of Solvents and Additives for Lithium-Ion Batteries near Lithium Anodes. *Journal of the Electrochemical Society*, 153(12):2192–2197, 2006.
- [151] Makoto Ue, Akinori Murakami, and Shinichiro Nakamura. Anodic Stability of Several Anions Examined by Ab Initio Molecular Orbital and Density Functional Theories. *Journal of the Electrochemical Society*, 149(12):1572–1577, 2002.
- [152] P Johansson. Electronic structure calculations on lithium battery electrolyte salts. *Physical Chemistry Chemical Physics*, 9(August 2006):1493–1498, 2007.
- [153] John E. McMurry. *Chemistry of Benzene : Electrophilic Aromatic Substitution*, chapter 16, pages 547–598. Brooks Cole, 7th edition, 2007.

- [154] MC Buzzeo, C Hardacre, and RG Compton. Extended electrochemical windows made accessible by room temperature ionic liquid/organic solvent electrolyte systems. *ChemPhysChem*, 7:176 – 180, 2006.
- [155] MC Kroon, W Buijs, CJ Peters, and G-J Witkamp. Decomposition of ionic liquids in electrochemical processing. *Green Chemistry*, 8(October 2005):241–245, 2006.
- [156] G Zhang and C B Musgrave. Comparison of DFT methods for molecular orbital eigenvalue calculations. *Journal of Physical Chemistry A*, 111:1554–1561, March 2007.
- [157] J Tomasi, B Mennucci, and R Cammi. Quantum mechanical continuum solvation models. *Chemical Reviews*, 105:2999–3093, August 2005.
- [158] M J Frisch, G W Trucks, H B Schlegel, G E Scuseria, M A Robb, J R Cheeseman, J A Montgomery Jr., T Vreven, K N Kudin, J C Burant, J M Millam, S S Iyengar, J Tomasi, V Barone, B Mennucci, M Cossi, G Scalmani, N Rega, G A Petersson, H Nakatsuji, M Hada, M Ehara, K Toyota, R Fukuda, J Hasegawa, M Ishida, T Nakajima, Y Honda, O Kitao, H Nakai, M Klene, X Li, J E Knox, H P Hratchian, J B Cross, V Bakken, C Adamo, J Jaramillo, R Gomperts, R E Stratmann, O Yazyev, A J Austin, R Cammi, C Pomelli, J W Ochterski, P Y Ayala, K Morokuma, G A Voth, P Salvador, J J Dannenberg, V G Zakrzewski, S Dapprich, A D Daniels, M C Strain, O Farkas, D K Malick, A D Rabuck, K Raghavachari, J B Foresman, J V Ortiz, Q Cui, A G Baboul, S Clifford, J Cioslowski, B B Stefanov, G Liu, A Liashenko, P Piskorz, I Komaromi, R L Martin, D J Fox, T Keith, M A Al-Laham, C Y Peng, A Nanayakkara, M Challacombe, P M W Gill, B Johnson, W Chen, M W Wong, C Gonzalez, and J A Pople. Gaussian 03, Revision C.02.
- [159] C T Lee, W T Yang, and R G Parr. Development Of The Colle-Salvetti Correlation-Energy Formula into A Functional Of The Electron-Density. *Phys. Rev. B*, 37:785–789, January 1988.

- [160] Larry A. Curtiss, Paul C. Redfern, Krishnan Raghavachari, and John A. Pople. Assessment of Gaussian-2 and density functional theories for the computation of ionization potentials and electron affinities. *Journal of Chemical Physics*, 109(1):42, 1998.
- [161] LA Curtissa, K Raghavachari, PC Redfern, V Rassolov, and JA Pople. Gaussian-3 (G3) theory for molecules containing first and second-row atoms. *Journal of Chemical Physics*, 109(18):7764, July 1998.
- [162] J. Paldus, J. Čížek, and I. Shavitt. Correlation Problems in Atomic and Molecular Systems. IV. Extended Coupled-Pair Many-Electron Theory and Its Application to the BH₃ Molecule. *Physical Review A*, 5(1):50–67, 1972.
- [163] Anthony P. Scott and Leo Radom. Harmonic Vibrational Frequencies: An Evaluation of HartreeFock, MøllerPlesset, Quadratic Configuration Interaction, Density Functional Theory, and Semiempirical Scale Factors. *Journal of Physical Chemistry*, 100(41):16502–16513, January 1996.
- [164] P Hapiot and C Lagrost. Electrochemical reactivity in room-temperature ionic liquids. *Chemical Reviews*, 108:2238–2264, 2008.
- [165] D. R. MacFarlane, P. Meakin, J. Sun, N. Amini, and M. Forsyth. Pyrrolidinium Imides: A New Family of Molten Salts and Conductive Plastic Crystal Phases. *Journal of Physical Chemistry B*, 103(20):4164–4170, May 1999.
- [166] Hajime Matsumoto. *Electrochemical Windows of Room-Temperature Ionic Liquids*, chapter 4, pages 35–54. John Wiley & Sons, Hoboken, 2005.
- [167] Giovanni B. Appetecchi, Maria Montanino, Andrea Balducci, Simon F. Lux, Martin Winterb, and Stefano Passerini. Lithium insertion in graphite from ternary ionic liquid-lithium salt electrolytes I. Electrochemical characterization of the electrolytes. *Journal of Power Sources*, 192(2):599–605, July 2009.

- [168] P Bonhote, AP Dias, Nicholas Papageorgiou, Kuppaswamy Kalyanasundaram, and Michael Gratzel. Hydrophobic, highly conductive ambient-temperature molten salts. *Inorganic chemistry*, (12):1168–1178, 1996.
- [169] Rico E. Del Sesto, Cynthia Corley, Al Robertson, and John S. Wilkes. Tetraalkylphosphonium-based ionic liquids. *Journal of Organometallic Chemistry*, 690(10):2536–2542, 2005.